THESIS

CREATING OPTICALLY STIMULATED LUMINESCENCE 3D PRINTING FILAMENT AND SYNTHESIZING RADIOSENSITIVE OPTICALLY STIMULATED LUMINESCENCE CRYSTALS

Submitted by

Evan Ross Burson DeVincenzo

Department of Environmental and Radiological Health Sciences

In partial fulfillment of the requirements

For the Degree of Master of Science

Colorado State University

Fort Collins, Colorado

Spring 2025

Master's Committee:

Advisor: Del Leary

Keara Boss
Ralph Sudowe
Kate Vickery

ABSTRACT

CREATING OPTICALLY STIMULATED LUMINESCENCE 3D PRINTING FILAMENT AND SYNTHESIZING RADIOSENSITIVE OPTICALLY STIMULATED LUMINESCENCE CRYSTALS

In radiotherapy, radiation oncologists use Megavoltage (MV) photon beams to deliver dose to target areas of a patient due to the MV's skin-sparing characteristics, but if the target area is near the surface of the patient, material referred to as a bolus is added to the patient's surface to provide dose build up and bring the maximum dose delivered close to the patient surface. Boluses are 3D printed to minimize air gaps between the patient and the bolus to deliver the dose accurately. Optically stimulated dosimeters (OSLD) are passive dosimeters that collect dosimetric information and are read later by using a stimulating laser to stimulate luminescence from the dosimeter, while a photomultiplier tube (PMT) measures the intensity of the luminescing light. We theorized that it was possible to combine 3D printing technology with OSLD crystals to make OSLD 3D printing filament so that an oncologist could 3D print a patient-specific bolus for a patient receiving radiotherapy treatment, and this bolus would function as a patient-specific dosimeter, ensuring precise, accurate, and safe delivery of dose-enhancing the overall quality of radiation therapy treatment.

The first chapter of this study explores how we incorporated OSLD crystals, Al_2O_3:C, which has a robust field of study exploring its radiosensitivity, with NinjaFlex TPU, a filament used to 3D print patient specific boluses, to create an OSLD filament for oncologists to use to 3D print a bolus which would read by a commercially available LANDAUER microSTAR reader, a reader that utilizes Pulsed Optically Stimulated Luminescence (POSL) technology. We did this

by cutting LANDAUER nanoDots, whose primary component is alpha carbon-doped aluminum oxide, into 1 mm or smaller pieces and cutting clear NinjaFlex TPU 3D printing filament into small, less than 1 mm pieces, mixing both at a ratio of 1:90, adding the mixture to a Filabot EX2 extruder, and extruding the mixture at low speed at 180 degrees Celsius. Afterward, the extruded filament was cut and re-extruded 2 more times, then warmed on a hot plate, compressed between 2 glass microscope slides, and cut into 8 mm diameter dots to create Filament Dot (FD) dosimeters. The FDs' dosimetric properties were tested and compared to LANDAUER Dot (LD) dosimeters, whose primary component is Al_2O_3:C crystals, using a Precision small animal irradiator (SAI). We found that the FDs' dosimetric characteristics were mostly similar to those of the LDs. This is the first study of this type, and we conclude that the results warrant further exploration into integrating OSLD material into 3D printing filament to 3D print radiosensitive patient boluses and 3D other radiosensitive models.

LANDAUER had recalled all their nanoDot dosimeters while we were conducting the first chapter of this study, so we decided to explore new ways to synthesize radiosensitive carbon-doped aluminum oxide crystals that the LANDAUER microSTAR could still read. We developed two methodologies: the Arc Furnace methodology, which utilizes an arc furnace to melt aluminum oxide (Al_2O_3) crystals with carbon (C) powder, and the Hot Acid methodology, which involves mixing alpha-phase aluminum oxide crystals with carbon powder in nitric acid and boiling the nitric acid off then firing the remaining powder in a muffle furnace. The Arc Furnace (AF), Hot Acid (HA), and unmodified aluminum oxide samples were exposed to 1940 cGy using the Precision Small Animal Irradiator. When read by the microSTAR, we found that the AF samples had the strongest luminescence compared to the unmodified aluminum oxide, and the HA samples had no significant difference compared to the unmodified aluminum oxide.

Then, to assess if the samples were more sensitive to low energy x-rays, we exposed the samples to an unfiltered beam from the SAI, and we found that the AF samples had a stronger-than-expected increase in luminescence strength when read by the microSTAR, indicating that the AF samples are acutely sensitive to low energy x-rays. We conclude that the Arc Furnace and Hot Acid methodologies created radiosensitive crystals by which the dose can be measured with the LANDAUER microSTAR, and we conclude further research should be conducted to refine these methods.

The first study chapter has shown that we can incorporate OSLD crystals into 3D printing filament and the second chapter explores two methodologies to synthesize the crystals. We conclude that further research should be conducted into the methods to synthesize the crystals and the method to integrate the OSLD into the 3D printing filament. This will lead to new methods to create OSLD filament, which can be 3D printed to make radiosensitive boluses that will improve patient outcomes and 3D printing of other objects that researchers will use in other radiotherapy research.

ACKNOWLEDGEMENTS

I want to express my appreciation and gratitude to those who supported me throughout this project. First and foremost, thank you to my advisor, Dr. Del Leary, for your help, support, and guidance. Next, I would like to recognize my committee, Dr. Ralf Sudowe, Dr. Keara Boss, and Dr. Kate Vickery. Amber Prebble, thank you for your help, particularly for always lending a hand with equipment in the lab. A special thank you to Dr. Michaella Harris for your help in developing and carrying out the Hot Acid Methodology, and to Dr. Jaimie Neilson and Layton Rudolph for your help in developing and carrying out the Arc Furnace Methodology. Lastly, I would like to express my deepest gratitude to Sarah Sublett and Dr. Diane E. Davise for your invaluable assistance with editing and revising my thesis.

TABLE OF CONTENTS

LIST OF TABLES

LIST OF FIGURES

INTRODUCTION

Megavoltage (MV) photon beams are often used in radiation oncology to treat cancers due to their skin-sparing characteristics caused by a dose build-up effect. The beam's maximum absorbed dose is beyond the patient's surface, so MV photon beams treat tumors deep within the body and achieve the desired skin-sparing characteristic. The effectiveness of the photon beam when treating a lesion depends on several factors, some of which are the beam's field size, the beam's energy, and the depth of the lesion (Almond et al., 1999). The location of the MV photon beam's maximum dose can be modified using a bolus to match a shallow lesion location. A bolus is a natural or synthetic material that is added to the patient's surface, acting as patient tissue and bringing the maximum absorbed dose closer to the patient's surface and the lesion location (Vyas et al., 2013).

Treatment planning systems calculate the dose to areas in the treatment field within a patient. However, when using a bolus to treat superficial lesions, air gaps between the patient's surface and the bolus are due to irregular surfaces. These air gaps can cause unintended build-up regions, and the planning systems may not accurately account for them, leading to an underdosing of the target region. The dose absorbed by the patient may be undercalculated by as much as 10.6% when the planning system does not accurately account for the air gaps and unintended build-up regions (Rana & Rogers, 2013). Overdosing patients can lead to patient harm and other undesirable outcomes from radiation treatment.

Additive manufacturing, colloquially known as 3D printing, is a rapidly advancing technology. Key advancements include more precise control of the shape and volume of 3D printed objects from several materials. These advancements can be applied to increase the accuracy of radiation therapy during treatment. As a result, 3D printing prints a patient specific

bolus, which will more closely align with the patient's physical dimensions and enhance treatment goals. Studies have shown that 3D printed boluses reduce air gaps and allow the dose delivered to the patient to be closer to the prescription (Martin et al., 2020).

The first part of this body of work explores the possibility and efficacy of combining material used for 3D printing boluses with crystals having known dosimetric properties, carbon doped aluminum oxide (Al_2O_3:C). The Al_2O_3:C crystal is used frequently in commercially available Optically Stimulated Luminescent dosimeters (OSLDs). Their incorporation into a patient's bolus would allow the shape and volume of the 3D printed bolus to be controlled and create a patient-specific dosimeter. Reducing air gaps and enabling direct dosimetric measurements would ensure precise, accurate, and safe delivery and enhance the overall quality of radiation therapy treatment.

The second part of this body of work explores two novel methods for creating radiosensitive Al_2O_3:C crystals. Since Al_2O_3:C crystals are no longer commercially available, creating new methods to synthesize them is critical if there is to be further exploration into incorporating Al_2O_3:C into 3D printed objects.

LITERATURE REVIEW

3D Printing Methods

Additive manufacturing, more popularly referred to as 3D printing, is a technique that casts thin layers in defined 2D shapes, then is sequentially added to, layer by layer, creating a 3D object. 3D printing has tremendous advantages in areas in which large scale mass manufacturing is weak, in that 3D printing allows a user to rapidly manufacture unique products with complex or bespoke parts. Traditional mass manufacturing requires a substantial amount of initial investment. Mass manufacturing may require designing specialized machines, training personnel, obtaining large amounts of raw materials, and other prohibitive factors. In contrast, 3D printing requires a printer, filament, a design, and an operator to produce physical objects. The 3D printing process is far more nimble. 3D printing will not replace mass manufacturing with its ability to produce many widgets more efficiently. Instead, it will address some of its shortcomings for products that would be too costly, difficult, or time-consuming to produce at scale.

Additive manufacturing (AM), as defined by ASTM Standard F2792, is "a process of joining materials to make objects from 3D model data, usually layer upon layer, as opposed to subtractive manufacturing methodologies." 3D printing is a term often used synonymously with AM, though the machines associated with 3D printing are generally lower in price and capability (F42 Committee, n.d.). ASTM International has categorized the primary AM techniques into seven categories: binder jetting, directed energy deposition, material extrusion, material jetting, powder bed fusion, sheet lamination, and vat photopolymerization.

Binder jetting is "an additive manufacturing process in which a liquid bonding agent is selectively deposited to join powder materials." Its advantages are printed objects free of

supports or substrates, a high level of design freedom, large build volume, high print speed, and relatively low cost. The disadvantages are that parts are fragile and have limited mechanical properties and printed objects may require post-print processing. Materials used to print are polymers, ceramics, composites, metals, and hybrid materials.

Directed energy deposition is "an additive manufacturing process in which focused thermal energy is used to fuse materials by melting as they are being deposited." The method has advantages: it is excellent for repair applications, printed objects are high quality, and the grain structure is highly controlled. The main disadvantage is that it is limited to making or modifying metal objects. The materials used to print are all metals or metal-based hybrids.

Material extrusion is "an additive manufacturing process in which material is selectively dispensed through a nozzle or orifice." The advantages are that the method is widely used, inexpensive, scalable, and can build fully functional objects. The disadvantages of material extrusion printing are vertical anisotropy in printed objects and step-structured surfaces, both of which make fine detail challenging to achieve. Materials used to print are polymers and composites.

Material jetting is "an additive manufacturing process in which droplets of build material are selectively deposited." Advantages include high accuracy of droplet deposition, low waste, and simultaneous use of multiple materials. Disadvantages include support materials are often required and deposited materials generally are limited to photopolymers and thermoset resins. Some additional materials used under specific conditions are ceramics, composites, hybrid, and biological materials.

Powder bed fusion is "an additive manufacturing process in which thermal energy selectively fuses regions of a powder bed." Advantages include it is a relatively inexpensive

method, the powder bed acting as an integrated support structure for printed objects, and the extensive array of materials used. Disadvantages are that this method is relatively slow, final products may lack structural integrity, size limitations, and the level of print detail depends on the size of the powder. Materials used to print are metals, ceramics, polymers, composites, and hybrids.

Sheet lamination is "an additive manufacturing process in which sheets of material are bonded to form an object." Advantages include the method's high speed, low cost, and ease of material handling. Disadvantages include the poor integrity of the final printed object, which depends on the strength of the adhesive used, the limited number of usable materials, and some printed objects that may require additional processing. Materials used are polymers, metals, ceramics, and hybrids.

Vat photopolymerization is "an additive manufacturing process in which liquid photopolymer in a vat is selectively cured by light-activated polymerization." Advantages include that this method makes large parts and has excellent accuracy, surface finish, and details. The disadvantages are that the method is limited to photopolymers, is more expensive, and is slower than the other methods. The materials used are photopolymers. (Tofail et al., 2018)

Material extrusion, also known as Fused Deposition Modeling (FDM), is one of the most widely used AM techniques and is relatively low-cost (Shahrubudin et al., 2019). An additional advantage of FDM printing is that many printing parameters can be modified, which optimizes the final printed object. Print quality, shell, infill, material settings, and speed are some printing parameters. The print quality controls the deposited layer heights and width of the deposited material. The shell controls the wall thickness of the print, excluding the bottom and top layers. Material is deposited in a particular pattern and is called the infill. The chosen infill pattern

affects the speed and quality of the printed object. The material controls the printing temperatures. The speed dictates how long the print may take often at the compromise of the level of printing detail. Being able to control so many parameters of a print make FDM printing an ideal method to test and print with novel materials.

3D Printed Bolus

Radiation oncologists sometimes treat superficial lesions on or adjacent to the patient's surface in radiation therapy. Megavoltage (MV) photon radiotherapy creates a photon beam that penetrates deep into the patient to deliver a dose to the tumor while delivering a relatively small dose to the surface, thus sparing the skin (Almond et al., 1999). Therefore, while using MV photon radiotherapy for superficial treatments, the depth of the lesion in the patient must be artificially increased to increase the dose delivered to the tumor. This is done by an oncologist placing tissue equivalent material on the patient's surface, called a bolus (Vyas et al., 2013). Superflab (Civco, Orange City, IA, USA) makes a synthetic gel-type material with a 0.2 to 4.0 cm thick thickness and a 1.02 g/cm^3 density that is placed over the lesion to be irradiated (*Bolus Material for External Beam Radiation Therapy*, n.d.). **Error! Reference source not found.** is a g eneral illustration showing that by placing the bolus on the skin, the maximum dose deposition, known as the peak Percent Depth Dose (PDD), is aligned with the clinical target volume.

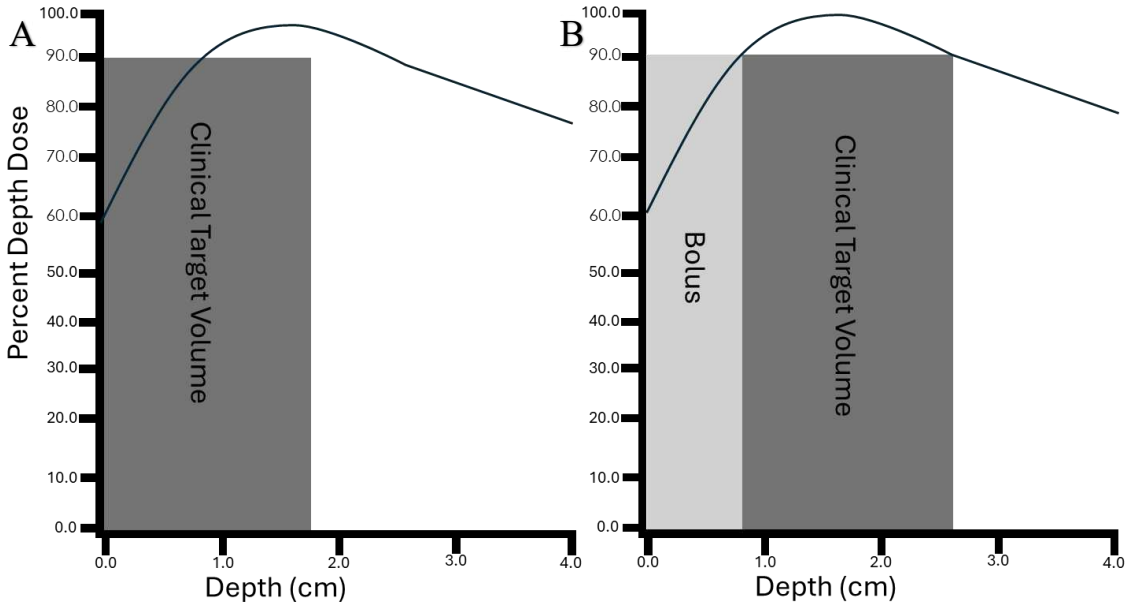

Figure 1: Percent Depth Dose (PDD) distributions are used to treat a superficial lesion. A) The PDD curve without a bolus shows the peak dose located deeper within the tissue and underdosing the clinical target volume. B) The PDD curve with an added bolus shows how the bolus artificially shifts the peak PDD closer to the surface and aligns it with the clinical target volume.

However, there can be uneven surfaces on a patient, and air gaps may form when placing a bolus on the uneven surface. These air gaps may be unaccounted for when planning treatment, creating discrepancies in prescribed and delivered doses (Martin et al., 2020). Suresh Rana and Kevin Rogers (2012) studied how air gaps affected the dose calculation algorithm, Analytical Anisotropic Algorithm (AAA). The authors used a 6 MV photon beam generated by a Varian Clinac IX accelerator equipped with a Millennium 120 multileaf collimator (Varian Medical Systems, Palo Alto, CA, USA to deliver 100 MUs to solid-water phantoms with rectangular Styrofoam blocks 2, 4, and 6 cm wide. The field sizes were 3 cm × 3 cm, 5 cm × 5 cm, and 10 cm × 10 cm. These blocks simulated air gaps and were placed 5 cm below the phantom surface. AAA was used to calculate the dose in solid-water material along the central beam axis. The authors calculated doses at 1, 1.5, 2, 3, and 4 cm below the phantom surface and 1, 2, 3, 4, and 5 cm in the solid-water after the air gap ended. The authors placed an Exradin A1 cylindrical

ionization chamber (Standard Imaging, Middletown, WI) at the same depths as the AAA dose calculations. The ionization chamber took a measurement three times, and the resulting electrometer readings were averaged and normalized to the reading collected at 1.5 cm below the phantom surface, the location where the dose delivered was highest. The authors calculated the percent depth dose (PDD) by normalizing the readings at this location, allowing the same dose normalization point for all depth dose computations and measurements. The authors compared the PDDs measured by the ion chamber to the PDDs calculated by AAA. They found that the PDD measured after the air gap was consistently higher than the PDD calculated by AAA, regardless of field size. The highest discrepancy between calculated PDD and measured PDD occurred when the field was 3 cm × 3 cm, and the air gap was 6 cm, resulting in an underestimation of the delivered dose of 10.6%, 5 cm after the air gap (Rana & Rogers, 2013). This result shows that air gaps can adversely affect the delivery of the prescribed dose to a patient by underdosing a lesion and overdosing healthy tissue.

Mindful of the adverse effects caused by air gaps during MV radiotherapy treatment, a study by Martin et al. (2020) was conducted to determine if custom 3D-printed boluses conformed better to patients compared to standard commercially available boluses. In this study, the patients were 5 dogs and 4 cats. All 3D-printed boluses were created by initially taking a computed tomography (CT) scan of dog and cat patients using a Philips Gemini TF Big Bore 16-slice scanner (Philips Medical Systems, Eindhoven, The Netherlands, B.V.) or an on-board cone beam computerized tomography (CBCT) using a Varian Trilogy (Varian Medical Systems, Palo Alto, California, USA) linear accelerator. The researchers uploaded the CT images to the Varian Eclipse (Varian Medical Systems) treatment planning system version 13.7, and using the AAA algorithm, the algorithm planned a bolus onto the patient's external body. An intensity-

modulated radiation therapy (IMRT) or 3-dimensional conformal radiation therapy (3D-CRT) plan was created with the generated bolus accounted for. The generated bolus was printed by a LulzBot TAZ 6 FDM printer (Aleph Objects, Loveland, Colorado, USA) using a thermoplastic polyurethane (TPU), Ninjaflex 85A (Ninjatek, Manheim, Pennsylvania, USA). TPU is an ideal material as boluses made from TPU have the same dosimetric properties as solid water (Hsu et al., 2008) and are flexible but durable. All boluses were 0.5 cm thick except for one bolus, which was 1 cm thick (Martin et al., 2020). **Error! Reference source not found.** is a photo of a dog w ith one of the customized 3D-printed boluses.

Figure 2: Photograph of a dog with a customized 3D-printed bolus. Reproduced with permission from (Martin et al., 2020).

The researchers compared the 3D-printed bolus to the commercial bolus by placing each on the treatment area of the patient and then taking a CBCT. They evaluated the scans in Eclipse

External Beam Planning by measuring the maximum air gap between the patient and each bolus for each 2-slice on CBCT. For the commercial bolus, the researchers found an average of 25% of the CBCT slices contained an air gap of 5 mm or larger, whereas only 7% of the CBCT slices of the 3D printed bolus contained an air gap of 5 mm or larger. The median air gap size of the commercial bolus was 3.6 mm, and the median air gap size of the 3D printed bolus was 2.3 mm (Martin et al., 2020).

An earlier study conducted by Burleson et al. (2015) showed that a 3D printer could print patient-specific boluses with a dosimeter inside the bolus for external beam therapies. In this study, researchers made a compartment within the printed bolus, placed LANDAUER nanoDot (LANDAUER, Glenwood, IL., USA) inside, and fitted the bolus to a phantom. The LANDAUER nanoDot is an Optically Stimulated Luminescent Dosimeter (OSLD) with plastic disks encased in a light-tight plastic holder. The Al2O3:C crystals are in the plastic disc, and the disc is placed in a reader and measured after exposure to ionizing radiation to determine the dose (Jursinic, 2007).

The researchers irradiated the phantom and bolus with a 9 MeV electron beam, with the nanoDot OSLD inside. The calculated dose to the phantom using the Varian Eclipse planning system was 159.0 cGy, and the average dose reading from the nanoDot was 159.8 cGy (Burleson et al., 2015). The researchers showed that an OSLD could be integrated with a 3D-printed bolus and validate the delivered dose.

3D Printed Radiosensitive Objects

Previous attempts to 3D print various dosimeters have been made. Below is a summary of three approaches researchers have taken to create a 3D-printed dosimeter.

3D Printable Inter Cross-Linking Network (ICN) Gels for Reversible Control with Water Content

Yosuke Watanabe, Shota Inoue, Azusa Saito, Masasu Kawakawami, and Hidemitsu Furukawa (2019) experimented with 3D printable inter cross-linking network (ICN) gels to create patient-specific dosimetric phantoms. ICN gels are tissue-equivalent radio sensitive chemicals that polymerize as a function of the absorbed dose within the gel. Researchers can see the level of polymerization optically, increasing opacity with increasing dose deposition. Therefore, ICN gels are ideal for 3D dosimetry and verification of patient-specific radiation therapy treatment. Researchers poured the gels into a 3D printed negative mold. This technique has challenges as it cannot create voids or cavities due to the extraction process. Here, the researchers investigated directly 3D printing the ICN gel phantoms to create more complex 3D structures (Watanabe et al., 2019).

The ICN gels used in the phantoms were synthesized in a two-step process. First, researchers placed an initial aqueous solution containing the rigid crosslinking polymer and initiator in a reaction mold space between a pair of glass plates, which reacted and formed the ICN gel. Then, they placed the ICN gel in a second solution for 2 days. The second gel had various concentrations of a cross-linking agent, N,N'-methylenebisacrylamide (MBAA). The gel was submerged in the second solution until the MBAA had been fully absorbed and uniformly distributed. Then, the gel was placed in an incubator at 30 ℃ and irradiated with UV LEDs at an intensity of 12.4 mW/cm^2 with a peak wavelength of 375 nm. The higher the concentration of MBAA in the second solution, the more opaque the gels will turn after exposure to UV radiation . After irradiation, researchers quantified the deposited dose by measuring the transmittance of light through the gel. They did that with a UV-2550 Shimazu spectrometer at a light wavelength

of 550 nm. The researchers found that the transmittance decreased exponentially with exposure to UV light (Watanabe et al., 2019).

As a proof of concept, a publicly available 3D model of a right index finger was printed to scale using the ICN gel with the highest concentration of MBAA. The researchers printed ICN gel phantoms with a customized 3D printer with a fluid dispensing print head. The printed finger was submerged in a second gel solution containing MBAA until the phantom was in an equilibrium swollen state. After seven minutes of UV radiation, the phantom optically transformed from transparent to opaque. The researchers could see more detailed patterns of the inhomogeneity of the dose distribution after they cut the phantom into slices. For example, no UV radiation reached the center of the finger phantom, so polymerization did not occur, and the gel remained transparent (Watanabe et al., 2019).

The study's authors successfully 3D printed ICN tissue equivalent gel for phantom creation detailing inhomogeneous dose distribution after UV radiation. However, there are some significant disadvantages to this method as the process is very time intensive-taking multiple days to complete and to make the phantom more sensitive to UV radiation, the researchers had to immerse the phantom in a second solution, and the phantom physically swelled which changed the physical dimensions of the phantom (Watanabe et al., 2019).

Characterization of Novel 3D Printed Plastic Scintillation Dosimeters

Nicholas Lynch, Thalat Monajemi, and James L. Robar (2020) investigated the feasibility of using raw scintillation crystals in FDM 3D printing as a formable dosimeter. The investigation explored how the various printing parameters would alter the printed plastic scintillation dosimeters (PSD) dosimetry. PSDs are any plastic and transparent material that luminesces with a suitable wavelength range as ionizing radiation passes through (Beddar et al.,

1992). The filament used was a non-cladded BCF-10 plastic scintillating fiber from Saint Gobain Crystals with a diameter of 3.0 mm (Lynch et al., 2020).

Optical signal measurements were obtained by placing printed objects in a light-tight box and using an Exemplar Plus spectrophotometer (Exemplar Plus, B&W Tek, Delaware, USA), which recorded all light and luminescence signals during irradiation (Lynch et al., 2020). The researchers performed signal acquisition and processing using the full spectral method where all optical signals are recorded, and then only the light with the wavelength associated with the PSD's luminescence is used to calculate the dose(Monajemi & Ruiz, 2018).

The specific printing parameters investigated were the print variability, layer thickness, anisotropy (non-uniformity), and extrusion temperature. The researchers correlated the dosimetry properties to the printed properties by measuring the stability, dose linearity, dose rate proportionality, energy dependence, and reproducibility of 1 cm^3 cubes (Lynch et al., 2020).

The researchers found a strong relationship between the layer thickness and the amount of collected scintillated light. They hypothesized that the increase in light intensity collected is due to an overall decrease in the number of layers, which decreases light scattering (Lynch et al., 2020).

To investigate the directional sensitivity, four 1 cm^3 cubes were printed at rotation angles of $0°, 45°, 90°,$ and $135°$. Then, each cube was irradiated 6 times at each surface of the cube. The results showed a robust directional dependence across all infill rotation angles, and cubes with infill rotation angles parallel or perpendicular to the shell showed increased light intensity (Lynch et al., 2020).

For a different set of 1 cm^3 cubes, the extrusion temperature was investigated and varied starting at 190 ℃ and raised to 225 ℃ in increments of 5 ℃. The researchers found that the

higher the extrusion temperature, the lower the scintillation intensity, with a maximum difference in signal intensity of 13.0%. The authors hypothesize that the heating of the filament during the printing process degrades the polymer or damages the fluorescent dopants (Lynch et al., 2020). This hypothesis is consistent with a thermal degradation process where molecular deterioration of polymers occurs due to excess heat (Novakovic et al., 2000). It is also possible that the high temperatures expose the scintillating filament to atmospheric oxygen and cause degradation in a photo-oxidation process (Geuskens & David, 1979).

The dosimetric properties of the printed cubes were evaluated by assessing the cube's signal stability, dose linearity, dose rate proportionality, energy dependence of the beam, and reproducibility (Lynch et al., 2020). Following are the methods used to assess the cube's properties.

The researchers assessed the signal stability by subjecting a cube to twenty consecutive 200 MU (2 Gy) doses with a 6 MV photon beam within a period of 1 hour. Over the 20 consecutive measurements, there was minimal error, with the standard error calculated to be 0.05%, showing the scintillation material is stable over many measurements and time (Lynch et al., 2020).

Dose linearity was measured between 40 cGy and 440 cGy in increments of 40 cGy at a dose rate of 200 cGy/min. The greatest diversion from linearity was 0.38%, and the root mean square deviation from linearity in total was 0.23% (Lynch et al., 2020).

Dose rate proportionality assessment required two methods. In the first method, the dose rate was directly varied from the accelerator, ranging from100 cGy min^{-1} to 600 cGy min^{-1} in increments of 100 cGy min^{-1} for a total dose of 200 cGy. The collected data showed that the total signal did not vary more than 0.10% for any pulse rate, and the standard error for the total

signal strength was 0.08% based on the normalized signal strength. In the second method, the dose rate was varied by delivering 200 MUs at a constant dose rate of 600 MU min^{-1} and changing the source-to-surface distance range from 65.25 cm to 145.25 cm in increments of 10 cm to effectively change the delivered dose rate due to the inverse square law of a diverging beam. The greatest deviation from linearity during measurements was 0.74%, and the root mean square from linearity for all measurements was 0.38% (Lynch et al., 2020).

The researchers evaluated the energy dependence by delivering 200 cGy at 100 kVp, 180 kVp, 300 kVp, and 6 MV. They found that relative to the 6MV energy, the scintillation signal dropped to 32% at 100 kVp, 46% at 180 kVp, and 66% at 300 kVp (Lynch et al., 2020).

Short-term, daily reproducibility was evaluated by exposing the printed cubes to 200 MU irradiations with 6 MV photons daily and immediately read over 14 days. The standard error measured was 0.0136, and the scintillation signal did not vary more than 2.1% from the mean, showing that the readings are highly reproducible (Lynch et al., 2020).

Lynch et al. concluded that 3D printing offered new avenues for producing and manufacturing PSDs, and it warrants further investigation into its application in dosimetry, including using 3D-printed PSDs for standalone dosimeters or incorporating PSDs into patient devices.

Fabrication of Radiophotoluminescence Dosimeter with 3D-Printing Technology

Taichi Hashimoto, Fuminobu Sato, Shingo Tamaki, Sachi Kusaka, Hiroyuki Miyamaru, and Isao Murata (2019) developed a material made from polycaprolactone (PCL) resin and radio photoluminescence (RPL) glass powder to 3D print objects with an FDM 3D printer. RPL dosimeters are similar to OSLDs, except RPL uses a glass compound as the luminescent material and requires a different excitation method to read the RPL dosimeter (Y.C. & Hsu, 2011). Researchers exposed the fabricated PCL/RPL dosimetric material, or filament, and 3D printed

objects printed with the filament to various doses of ionizing radiation. Then, researchers shined an ultraviolet (UV) light-emitting diode (LED) on the filament and objects, which caused the printed objects to emit an orange photoluminescence light. The strength of luminescence was proportional to the amount of radiation absorbed (Hashimoto et al., 2019a).

To create the RPL glass, commercially available sodium metaphosphate, aluminum metaphosphate, and silver chloride were placed in a mullite crucible and an electric furnace. The furnace was gradually heated to 1200 ℃ for 10 hours and then left for 5 hours to allow the components to homogenize. Then, it was left to cool to room temperature for over 10 hours, where it was cut with a diamond saw blade to make a powder (Hashimoto et al., 2019a).

The researchers investigated Multiple commercially available filaments to see which would mix with RPL. They determined that a polycaprolactone (PCL) resin (PLUS Corp., Tokyo, Japan) was the most ideal because when the RPL was mixed with PCL and then irradiated, the light output from the luminescence of the RPL after UV stimulation was most intense. A drawback of PCL is its low melting point, 57 ℃, so it is generally not used for 3D printing. However, by setting the extrusion temperature to an appropriately low level during printing, PCL can still be used as a printing filament (Hashimoto et al., 2019a).

The PCL resin was crushed into a powder form and mixed with the RPL powder (7.5% RPL glass powder by weight) and then placed in a filament-manufacturing machine for 3D printers, a Filabot EX2 filament extruder (Filabot, Barre, Vermont, USA). The researchers set the extrusion temperature of the Filabot to 170, and the discharge port had a diameter of 1.75 mm. The PCL resin and RPL powder mixture was extruded through the Filabot to make a PCL/RPL filament with a diameter of 1.75 mm and a density of 1.20 g/cm^3 (Hashimoto et al., 2019a).

In 2014, Sato et al. developed a system to stimulate the RPL and then measure its luminescence. The system contains a light-tight box with a stage, a stimulating UV-LED with a wavelength of 365 nm, a UV-transmitting optical filter, a red-transmitting optical filter, a photodiode, and a microammeter. The readout system worked by stimulating the RPL with light from the UV-LED. The photodiode detected the light from the luminescence and generated a current, which was then measured by the microammeter. The spectrum of luminescing light had two peaks, 430 and 635 nm. When the RPL filament was not irradiated with ionizing radiation and read with the previously described technique, the luminescing light only had one peak of 430 nm. Therefore, the researchers determined that the peak at 635 nm depended on the absorbed dose, and the more light measured during luminescence with the wavelength of 635 nm, the higher the dose the RPL filament absorbed (Sato et al., 2014).

Samples were printed from the PCL/RPL filament and irradiated with a 90 kV microfocus X-ray tube (L9421-02, Hamamstsu Photonics K.K., Shizuoka, Japan) with a current of 89 μA (Hashimoto et al., 2019a). Dose measurements of the samples showed a linear relationship between the delivered dose and the intensity of the recorded light from the RPL luminescence ranging from 30 mGy to 10 Gy (Hashimoto et al., 2019a).

Proof-of-concept experiments were carried out by printing two different objects: a ring and a human ear. The researchers cut the printed ear open and examined the dose distribution within the ear. The measured dose profile of the cut-open ear was compared to a computational simulation and found that the computational simulation produced a similar dose profile to the dose profile of the printed ear (Hashimoto et al., 2019a).

Hashimoto et al. were able to make a remarkably effective 3D printable dosimeter in that the dosimeter was able to be printed as complex shapes and have a dose profile of those shapes

generated; the luminescence intensity during the reading of the dosimeter was proportional to the absorbed dose, was read multiple times, and it had a wide range of doses the dosimeter is sensitive to. There are various disadvantages to these 3D printed dosimeters. The first is to read the dose from the dosimeter a custom reader had to be designed and made. The second is that the PCL/RPL filament is not tissue equivalent with an effective atomic number of 7.1, meaning corrections would need to be made when the material is used to make water equivalent phantoms (the effective atomic number of water is 7.4) (Hashimoto et al., 2019a).

Thermoluminescence

A precursor to optically stimulated luminescence is thermoluminescence (TL), where recorded light proportional to dose is emitted by heating a solid to a temperature below incandescence. Excited electrons are liberated during ionizing radiation and become trapped within crystal imperfections. With sufficient energy in the form of heat, the trapped electrons escape the traps, and the electrons recombine to release light. The released photons' energy can be discreet and has a corresponding wavelength. This wavelength is called a thermoluminescence peak. A photomultiplier tube measures the intensity of light and the greater the intensity of light measured by the photomultiplier tube, the higher the dose absorbed by the TL material (Daniels et al., 1953).

G. P. Summers (1984) studied Al_2O_3 for its thermoluminescence properties. Al_2O_3 is grown in reducing environments, causing anion vacancy defects (F-type centers) to form and making it sensitive to ionizing radiation. As a result of the F-centers, there are two primary observed thermoluminescence peaks in Al_2O_3 around 320nm (photon energy of 3.8eV) and 410nm (photon energy of 3.0eV). The F-centers are defects within the crystal structure and lack an oxygen ion. The emission of a photon at the 320nm wavelength is due to the anion vacancy defect, or F^+ center, trapping one electron. The anion-deficient vacancy only captures one

electron, so the vacancy still has a net positive charge with respect to the rest of the crystal lattice. When the F^+ center traps an additional electron, the vacancy becomes an F center again as it is back to neutral with respect to the crystal lattice. In the Al_2O_3 lattice a slightly disoriented close-packed O^{2-} ion sublattice is present. In his sublattice Al^{3+} ions occupy two octahedral interstices (Summers (INVITED), 1984).

By irradiating Al_2O_3 with x-rays or γ-rays, thermoluminescence is induced later. The ionizing radiation does not damage the physical structure of Al_2O_3, so the only effect the radiation can produce is changing the charge state of impurities or defects within the crystal. Specifically, the changes are the capture or loss of electrons or electron holes. F or F^+-centers capture electrons while the crystal is heated, and photons are released. These photons have wavelengths of 320 nm and 410 nm. When the F^+-center captures an electron, a 410 nm photon emission specifically occurs (Summers (INVITED), 1984).

M. S. Akselrod, V. S. Kortov, D. J. Kravetsky, and V. I. Gotlib (1990) found and developed a material that was highly efficient and had a large TL signal when the material absorbed a small dose. This material was a single crystal of Al_2O_3:C grown by the Verneuil method (Akselrod et al., 1993). The Vernuil method is a process developed by Augusta Verneuil where finely ground Al_2O_3 flows down a narrow tube with a small opening. At the opening, a flame of at least 2030 ℃ is applied, which melts the powder into molten drops. These drops drip onto a rod, form a solid mass, and are left to cool to make a single crystal (Barvinschi et al., 1999). The researchers found that oxygen vacancies are essential in creating the exoemissive and luminescent properties of SiO_3 (Kortov, 1985). The key to the high sensitivity of Al_2O_3:C was the large number of oxygen vacancy centers formed during the crystal growth. The process of forming Al_2O_3:C involves crystallization, forming solid crystals from solution, under strongly

reducing conditions. Two-valent ions of carbon replace three-valent Al cations within the oxide lattice during crystallization, which leads to hole-trapping centers. The researchers observed that during optical absorption tests of Al_2O_3:C crystals, they strongly absorbed 205 nm photons conditioned by transitions in F-centers and 230 nm and 255 nm photons due F^+ centers. The centers are formed as charge compensators to heterovalent impurity C^{2+} ions, so the absorption intensity increases with the amount of carbon introduced into the crystal. F-centers are the main contributor to the luminescence of Al_2O_3:C, which has a measured emission spectrum with a maximum of 420 nm. This peak is well within the spectral sensitivity of low-noise photomultiplier tubes, an essential aspect for effective luminescence measurements (Akselrod et al., 1990).

Further exploration of Al_2O_3:C was conducted and initially single crystals of Al_2O_3:C in the shape of discs with 5 mm diameters and 1 mm thick were created by cutting them from a single crystal rod. The crystal rods were grown from a melt at 2050 ℃ and were grown by the Verneuil method. The raw material which was melted was Al_2O_3 with impurities, the most important impurity being carbon in a concentration of 100-5000 ppm. At the final stage of production, the crystals were annealed in air at 950 ℃ for 30 minutes to remove stresses that may have occurred during the growing, cutting, and grinding (Akselrod et al., 1993). Also, this final anneal empties all traps within the crystal (Akselrod & Gorelova, 1993).

Researchers found that the Al_2O_3:C single crystals had a high sensitivity to ionizing photons and could be stored in the dark and measured up to two years later without appreciable fading. To address skin dosimetry problems the Al_2O_3:C single crystals were ground to a powder of various grain sizes using a ball-tube mill. Researchers tested the TL sensitivity and response of Al_2O_3:C. Various grain sizes were measured and the grain size of 125-200 μm had the highest

TL output, meaning the ideal size of Al_2O_3:C in powder form is 125-200 µm for dosimetry purposes (Akselrod et al., 1993). However, Al_2O_3:C was sensitive to visible light, resulting in light-induced fading. Researchers found that exposing Al_2O_3:C to visible light after irradiation caused fading, the loss of TL signal, and any dosimetric information. The light-induced fading showed that exposure to light caused the dosimetric traps within the crystal to empty (Moscovitch et al., 1993).

Researchers discovered that Al_2O_3:C is highly light-sensitive which leads to a substantial loss of TL signal. The shorter the wavelength, the greater the TL signal loss when the Al_2O_3:C was exposed to the light for the same period. Also, the TL signal loss was more acute in samples exposed to a higher dose. The TL signal loss caused by exposure to light showed that light was optically stimulating electrons from the traps responsible for the TL signal used in dosimetry measurements (Walker et al., 1996).

Another phenomenon within a material like Al_2O_3:C while measuring its TL signal, is phototransferred thermoluminescence (PTTL). PTTL occurs when the material is irradiated, heated to remove all charges from the shallow traps, and left to cool. The material was left to cool and then stimulated with light with a short enough wavelength to provide enough energy to excite an electron from a deep trap and liberate the electron. Most newly liberated electrons are re-trapped in the now-vacant shallow traps. Researchers reheated the material and measured the TL signal, and the TL signal is due to the release of electrons from the shallow traps (Alexander & McKeever, 1998).

Optically Stimulated Luminescence Theoretical Description

When a semiconducting or insulating material absorbs energy from ionizing radiation, excitation occurs within the material, which frees electrons and electron holes. The energy from the incident particle is absorbed, and charges are excited primarily through the Compton effect or

photoelectric effect (Akselrod et al., 2006). The Compton effect is when a photon collides with an electron, the photon is inelastically scattered, and the electron absorbs some of the photon's energy. When the photon is scattered, its wavelength shifts to a longer wavelength by the laws of conservation of energy and momentum (Compton, 1923). The photoelectric effect is when an atom absorbs a photon, and the absorbed energy is sufficient to eject an electron from its orbital, usually from an inner shell (Einstein, 1905). When the energy absorbed by the electron is high enough, the electron leaves its orbit and is unbound. In semiconducting or insulating materials, electron holes are made as well. These freed electrons and electron holes travel within the material until defects within the material trap them. Another way to describe the OSLD material is to refer to the material as a system. In this system, when there are no electrons or electron holes trapped, the system is in thermodynamic equilibrium, but defects in the system trap electrons or electron holes. The electrons and electron holes remain trapped until they are stimulated out of their traps by some external energy source where they may recombine with each other. This process can also be thought of as returning the system from a metastable state to thermodynamic equilibrium. In OSLDs, the external energy source is light, which can be UV, visible, or infrared (Akselrod et al., 2006).

The light intensity emitted from luminescence is caused by the rate at which the electrons and electron holes recombine. This rate is dictated by the number of electrons and electron holes trapped. The intensity of the luminescence is measured as a function of time that produces a luminescence over a time curve. The integral of this curve is related to trapped electrons and electron holes, which are proportional to the dose absorbed during irradiation (Akselrod et al., 2006).

Figure 3 depicts the various pathways an electron/electron-hole pair may follow within an OSLD crystal after exposure to ionizing radiation. Figure 3 also depicts the pathways previously trapped electrons/electron holes may follow after being liberated from their traps with energy absorbed from incoming light. Pathway 1 is the absorption of ionizing radiation and creating the electron/electron-hole pair. Pathway 2 represents how the electron may travel along the conduction band before it falls into a trap. Pathway 3 represents how the electron-hole may travel along the valence band before falling into a trap. Pathway 4 is an electron traveling from the conduction band, and a Shallow Electron Trap (SET) captures it. Pathway 5 is the release of the electron from the SET and occurs without stimulating light at room temperature. The release of electrons from SETs is transient and has a half-life of 48 seconds. Pathway 6 is an electron hole falling from the valence band and a Deep Hole Trap (DHT) capturing it. Pathway 7 is the release of the electron hole from the DHT, which occurs at 550 ℃. Pathway 8 is an electron falling from the conduction band, and a Deep Electron Trap (DET) captures it. Pathway 9 is the release of the electron from the DET, occurring at 900 ℃.. Pathway 10 is an electron falling from the conduction band, and an Intermediate Electron Trap (IET) captures it. Pathway 11 is the liberation of the electron from the IET after the IET absorbs heat or light. The light can come from a source outside the crystal, like a laser, or from within. Light is released during thermoluminescence or optical luminescence and can stimulate an electron or electron hole to escape from one of the traps. Pathway 12 is the capture of an electron-hole by an F center, creating an F^+ center. Pathway 13 is the electron liberated from the IET, traveling along the conduction band and falling to the F^+ center, where the electron/electron-hole recombines and emits light (Jursinic, 2010).

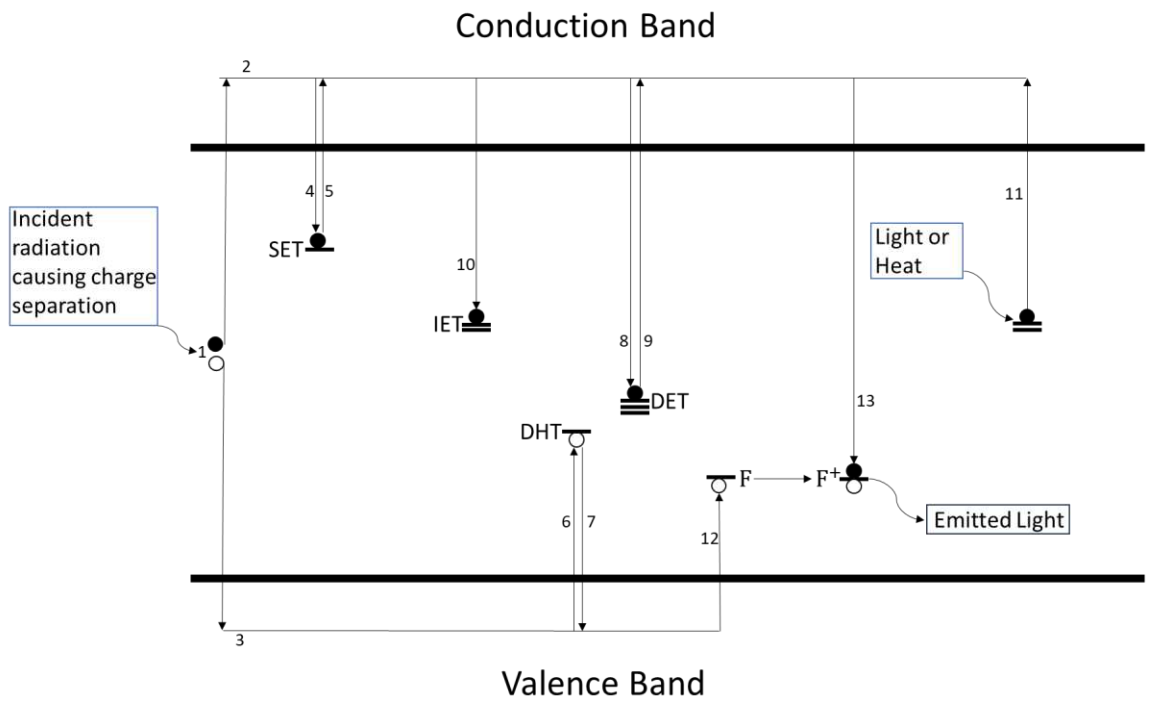

Figure 3: Diagram of the various pathways electrons and electron holes may follow within the crystalline structure, as well as the various traps the electrons/electron holes may be captured in. The black dots represent electrons, and the white dots represent electron holes.

Photomultiplier Tubes

The instrument used to measure the strength of the luminescing light from the stimulated TLDs and OSLDs is a photomultiplier tube (PMT). PMTs were the first devices able to detect single-photon signals and are devices that researchers use due to their reliability and accuracy when measuring low levels of light in fields ranging from medical imaging to physics experiments. A typical PMT, illustrated in **Error! Reference source not found.** and described b y Serve Polyakv of the National Institute of Standards and Technology (2013), contains a photocathode, several dynodes, and an anode in a sealed glass tube with a high vacuum inside. The PMT works by a photon entering the tube through a window in the PMT. The incoming photon excites electrons from the photocathode, and some of the excited electrons are emitted into the vacuum and become photoelectrons. The first dynode, which is a secondary-electron emission surface, focuses the photoelectrons and from the first dynode, the photoelectrons are

multiplied by the secondary-electron emission effect and are emitted to the next dynode. The process of photoelectrons being emitted from one dynode to the next dynode and increasing the number of photoelectrons after each interaction with the dynodes occurs several times until there are no more dynodes, resulting in a high-gain amplification of the initial signal. The anode collects the secondary electrons from the last dynode, generating a current spike or pulse. Finally, detection electronics outside the PMT measure this current spike (Polyakov, 2013).

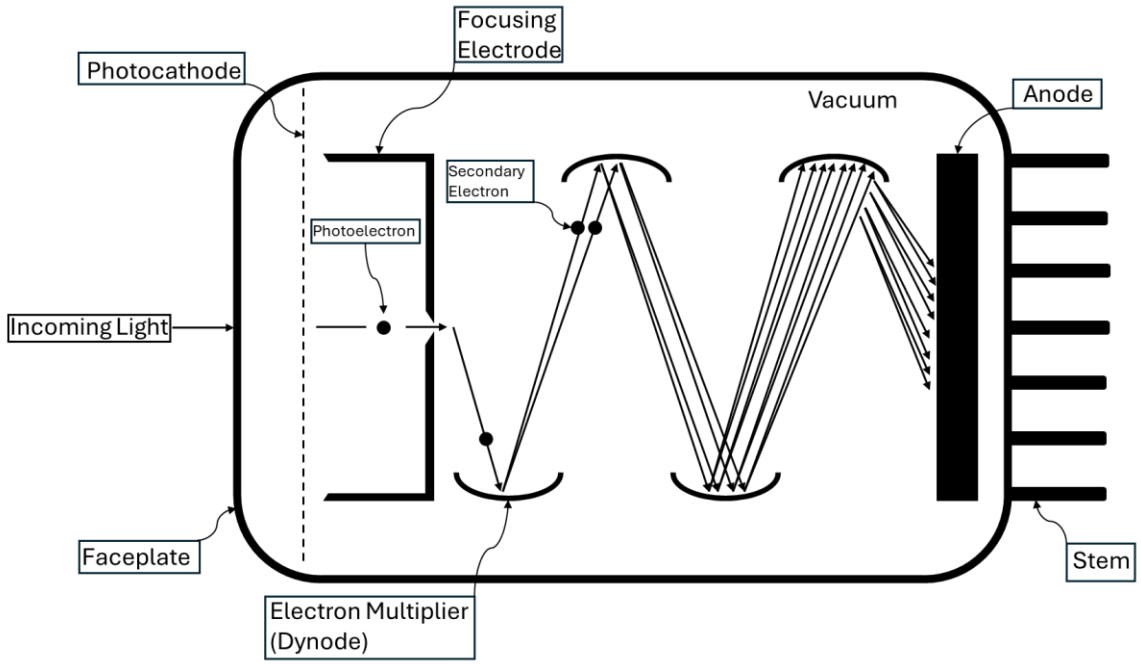

Figure 4: A diagram of a typical PMT whereby incoming light enters through the faceplate and interacts with the photocathode to generate a photoelectron; the photoelectron is then focused and propelled to the electron multiplier (dynode). Next, secondary electrons are generated and propelled to subsequent dynodes until the anode collects the secondary electrons, a current is generated in the anode, and outside electronics measure the current.

The electron transit time of a PMT is the time it takes the photoelectrons in the tube to travel from the photocathode to the anode. This time varies because the photoelectrons and secondary-electron beams take various paths within the tube, so the average electron transit time and the variation of the average transit time are considered. All these factors are affected by the material used to make the dynode and the configurations of the dynodes. There are tradeoffs

between configurations and materials that may minimize electron transit time, maximize collection efficiency, or spatial response uniformity. Depending on the application, the most suitable dynode materials and configurations are chosen (Polyakov, 2013).

There are important drawbacks to consider when using PMTs. PMTs are sensitive to single photons by having the incoming photon generate a photoelectron, amplified by the dynodes until the anode collects the amplified signal, where the resulting current spike, or pulse, is measured. However, this current spike is not resolved instantaneously, and photons may enter the PMT close enough together such that the resulting pulses are close enough together that they are indistinguishable from each other and, as a result, are measured as a single large pulse. Another drawback is that the pulse height from single photons can vary, which makes it difficult to determine whether a single or multiple photons caused a large pulse (Polyakov, 2013).

The process of two pulses occurring so close together that they become indistinguishable from each other is called pulse overlap. One of the factors that contributes to pulse overlap is called dead time. No new input pulses can be detected during dead time, the period after an initial detection. The length of time varies depending on the PMT and its design, where a typical dead time is 10 ns but can be as short as 1 ns. In practice, external corrections limit dead time. Reduced dead time can be achieved through improved pulse counting electronics, or missed counts can be countered by applying correction factors while measuring weak light sources (Polyakov, 2013).

To address the drawbacks of the various pulse heights in PMTs, distributions of the pulse heights are measured. First, the distribution is measured with an input of a known optical signal and then measured again with no optical signal. The discriminator threshold is set based on the pulse height distribution measured with the known optical signal, and the threshold will be low

enough that pulses caused by photons pass through the discriminator and are counted. The pulse height distribution measured with no optical signal characterizes dark current. Dark current are pulses generated from thermal electron-emissions (Polyakov, 2013). Thermal electron-emissions occur when heat generated on the photocathode or the dynodes is transferred to electrons so that they have enough energy to escape their orbitals and become unbound (Huffman, 2003). Thermal electrons originating from most dynodes undergo fewer amplification stages, so their generated pulses have a lower amplitude and are mostly filtered out by the discriminator. However, thermal electrons from the photocathode or the first few dynodes may be amplified enough to make their resulting pulses indistinguishable from pulses caused by photons. The likelihood of dark current generating a pulse and recorded as a count caused by a photon depends on the discriminator level. Increasing the discriminator level reduces the number of dark counts but may also reject counts caused by photons, so the PMT's efficiency varies depending on the discriminator threshold. Considering these tradeoffs, the discriminator level depends on the application and objectives, ensuring single-photon detection is maximized without compromising the PMT's performance (Polyakov, 2013).

In addition, after pulsing may occur, which can lead to false detections. Two main ways after pulsing may occur in PMTs: elastic scattering of electrons on the first dynode and ionization of residual gas in the tube. Elastic scattering of electrons on the first dynode is generally not a problem because the after pulse is measured 1 ns after the initial pulse, so the after pulse is not recorded due to dead time. Ionization of residual gas results in positive ions being present in the tube, which is pulled to the photocathode, knocking out electrons, with the knocked-out electrons being pulled to the dynodes and amplified, eventually leading to a counted

pulse. To address counts caused by ionization, the probability of an after pulse occurring is estimated, and a statistical correction may be applied (Polyakov, 2013).

LANDAUER nanoDots

Paul A. Jursinic (2007) characterized LANDAUER nanoDots. The nanoDots have been previously discussed and are OSLDs in which crystals of Al_2O_3:C are contained in a plastic disk, and the disks are encased in a light-tight plastic holder. When exposed to ionizing radiation, the Al_2O_3:C crystals store the energy and are read by putting them in a LANDAUER microSTAR reader. In the reader, the plastic disc is moved from the light-tight plastic holder, and the reader stimulates the crystals by illuminating the disc with a laser having a peak wavelength of 540 nm. The Al_2O_3:C crystals release the stored energy as luminescence with a peak wavelength of 420 nm. A useful property of the nanoDots is that they can be read repeatedly with only a 0.05% decrease in signal, and the OSLD does not have to be completely discharged to obtain accurate signals. The original strength can be calculated if the total number of reading cycles is known. Additionally, the OSLDs slowly decay over time, about 2% of their signal after 2 days, then stabilizing after that. This allows the reading of the OSLD and storage of it for future readings and acts as a permanent record of measured dose (Jursinic, 2007).

The luminescence response of the OSLDs was linear, with absorbed doses being exposed to doses 1-300 cGy. At about 300 cGy, a slight supra-linearity trend was observed. When the nanoDots were exposed to 100 cGy of radiation from a ^{192}Ir source (which decays to excited states of ^{192}Pt and ^{192}Os that emit gamma rays with an average energy of 370 keV (Nath et al., 1995)), 6 and 15 MV x-rays, and 6, 9, 12, 16, and 20 MeV electrons, it was found that the luminescence strength was the same across all energies. Thus, there is no dependence on the radiation energy (Jursinic, 2007).

It was found that nanoDots can be reused if they are zeroed (optically annealed). This is easily achieved by exposing them to visible light. The annealing can be accomplished by leaving the disc containing the Al_2O_3:C crystal exposed to bright room light for many hours or a 1-minute exposure to a tungsten-halogen lamp (Jursinic, 2007).

Pulsed Optically Stimulated Luminescence

The conventional technique for reading OSLDs is to turn on the stimulating light and read the luminescence at the same time, a technique known as continuous-wave stimulation (CW-OSL) (Bulur, 2000). In 1996, McKeever et al. addressed a major drawback posed by the CW-OSL technique- the difficulty separating the light from the stimulation and emission during the measurement. This is particularly difficult during low dose measurements where the number of photons from emission needs to be measured with a background intensity $10^{15} - 10^{20}$ larger caused by the stimulating light. Various filters may be employed, but even the most sophisticated light filtration system cannot completely remove the background signal from the stimulating light beams, and as a result, the background signal can be a serious detriment to the accuracy of the measurements (Akselrod & McKeever, 1999).

To address the problem of high background signal, the CW-OSL technique is modified by only measuring the amount of light coming from the material after turning off the stimulating light source, e.g., PTTL/COSL and DOSL, but these techniques have major limitations as they do not measure any luminescence emitted during the optical stimulation stage. As much as 70-90% of liberated electrons recombine and emit light during stimulation (prompt luminescence) (Akselrod & McKeever, 1999).

Pulsed Optically Stimulated Luminescence (POSL) addresses the drawbacks of the techniques by preferentially measuring the prompt luminescence after stimulating light pulses. There is still a short delay, so the photomultiplier tube (PMT) may relax. The stimulating laser

light continuously stimulates the trapped electrons by turning the laser light on and off in fast pulses a pre-determined number of times. The laser light is turned off for less than the lifetime of the prompt luminescence, and the PMT measures the emitted light from the OSL material while the laser light is off. The signal measured by the OSL is integrated, and the final measurement results from the integrated signals. Two essential characteristics of the laser light and PMT must be met for the POSL method to be viable. For the laser light, the time the laser is on must be substantially shorter than the lifetime of the prompt OSL emission for the measured OSL material. The time between pulses must be 10-20 times longer than the relaxation time of the PMT- while 5-10 times shorter than the prompt luminescence lifetime. This allows the laser pulses to induce significant luminescence and build up the total number of excited states while not losing luminescence, and consequently signal, during stimulation. The amount of light collected and lost during the pulse and delay for the PMT relaxation period is relatively high and results in high luminescence measurement efficiency (Akselrod & McKeever, 1999).

Figure 5 is a diagram for measuring the POSL signal. T_1 is the period of the laser's full-width half maximum (the width of the laser pulse), T_2 is the dead time where the PMT is blocked and not measuring any light, and T_3 is when the gate is open and allows the PMT to measure any luminescing light (acquisition). The POSL must be with equipment and materials such that the luminescence lifetime τ is longer than the measuring time, dead time, and laser pulse period such that $T_1 < T_2 < T_3 < \tau$ (Akselrod & McKeever, 1999).

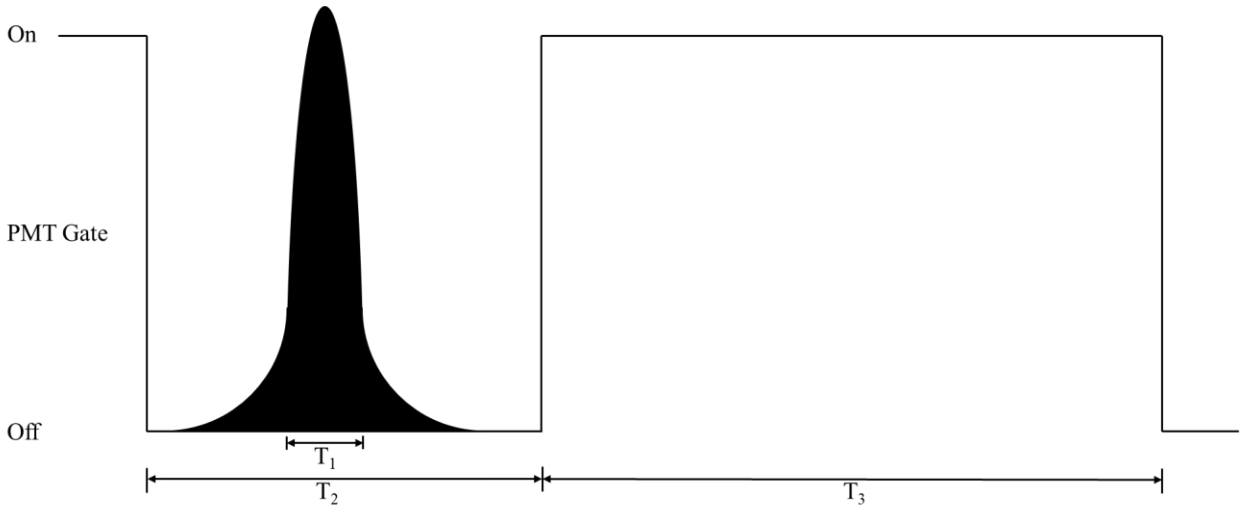

Figure 5: Diagram of the POSL measuring method. T_1 is the period of the laser pulse, 300 ns, T_2 is the period in which the PMT is turned off and not measuring any signal, 15 μs, and T_3 is the period which the PMT is turned on and measuring light

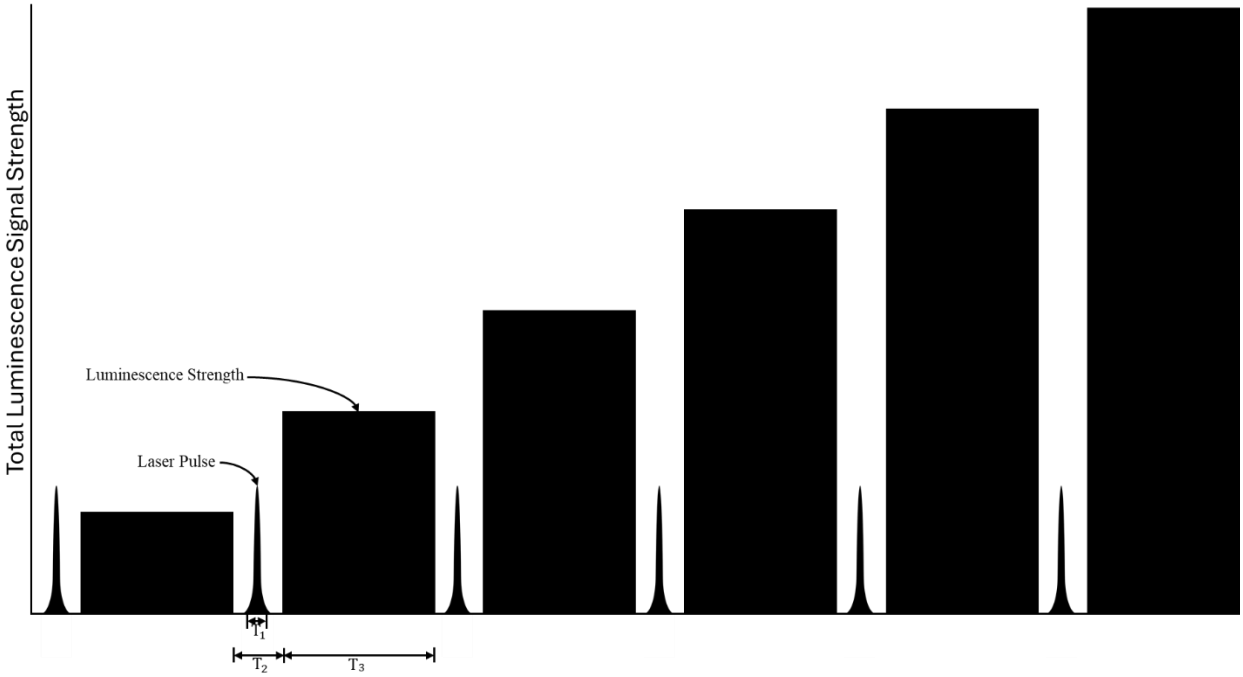

Figure 6: Diagram showing how frequent stimulation from laser pulses continuously excites electrons out of traps and increases luminescence.

For Al_2O_3: C the characteristic time periods are the luminescence lifetime of Al_2O_3:C, $\tau = 35 - 36\text{ms}$, the laser pulse period, $T_1 = 300$ ns, the period the PMT is turned off, $T_2 = 15$ μs, and the period the PMT is turned on, $T_3 = 235$ μs, while using a Nd:YAG laser in its

second harmonic mode. The available power, full width half max time, and repetition frequency dictates the stimulating laser light. The light from the stimulating laser must be within the range in which the OSL material will absorb the incoming light and liberate the electrons from the traps. In the case of Al_2O_3:C, a laser emitting light with a wavelength of 532 nm will liberate trapped electrons and cause the material to luminesce. At the chosen frequency of 4kHz, the deadtime for a 1 second stimulation period is 60 ms ($60\ \text{ms} = 4000 \times 15\ \mu\text{s}$) so the total acquisition time is 940 ms ($940\ \text{ms} = 1000\ \text{ms} - 60\ \text{ms}$). This means that the data acquired is 94% of the stimulation period, and since $\tau \gg T_3$ the luminescence intensity can be approximated to be constant. Therefore, the measurement efficiency is approximated to be about 94% (Akselrod & McKeever, 1999).

Since the luminescence lifetime of stimulated $Al_2O_3:C$ is substantially longer than the time the PMT is not gated and acquiring signal, T_3, and the frequency of the laser pulses is high, the $Al_2O_3:C$ is being stimulated again before it had stopped luminescing from the stimulation caused by the previous laser pulse. As a result, when the laser is pulsed more the luminescence of the $Al_2O_3:C$ increases until an equilibrium is reached where the trapping centers in the $Al_2O_3:C$ are being excited at the same rate, those same centers are decaying. Later, as more of the trapping centers are emptied, the luminescence strength decreases, and consequently, the signal recorded by the PMT decreases as well. This is why a decrease in luminescence signal is found during relatively long stimulation times or over the course of many measurements. Trapping centers are also stimulated and emptied at higher rates as the strength of the pulsed laser increases. Therefore, the POSL signal depends on the strength of the pulsed laser, the period the laser is turned on, and the frequency of the pulses (Akselrod & McKeever, 1999).

For $Al_2O_3:C$ the lifetime, τ, of luminescence after stimulation is approximately 35 ms (Summers (INVITED), 1984) so signals were to be collected in series, which would mean the $Al_2O_3:C$ would be stimulated and allowed to decay entirely before it was stimulated again, the time between pulses would have to be $3\tau \approx 100$ ms. This would correspond to a laser frequency of about 10 Hz. If the laser were pulsed 4000 times the measurement period would be 400 seconds. But when the pulse frequency is increased to 4000 Hz, the signals from the stimulated $Al_2O_3:C$ are effectively collected in parallel, and the measurement time is reduced to just 1 s to collect the same amount of signal. In addition to significantly shorter collection time, the pulse width is 300 ns, so a very small amount of signal is lost when the PMT is turned off and not collecting signal while the laser is turned on (Akselrod & McKeever, 1999).

Reducing the laser pulse width and increasing the laser power can increase the luminescence strength emitted after the pulse and reduce signal loss (McKeever et al., 1996). It was found that several detrimental processes can occur when peak power densities are too high. One such process is two-photon absorption, where luminescent material absorbs two photons (Göppert-Mayer, 1931) from the stimulating laser and luminesces (Akselrod & McKeever, 1999). The luminescence recorded from this process is unrelated to the absorbed radiation dose. If the laser power density is too high, laser-induced heating can occur where the local temperature increases, which leads to a loss of OSL signal by either or both thermal quenching (Akselrod et al., 1999) or thermal emptying of trapped electrons (Akselrod & McKeever, 1999). Another reason to restrict the laser power is that even when the PMT is turned off, the photocathode material can still be damaged if the intensity of any absorbed light is too high and lead to photomultiplier tube 'blinding' (Akselrod & McKeever, 1999).

microSTAR

By leveraging the principles of OSLDs and pulsed optically stimulated luminescence, LANDAUER developed the microSTAR to read customized OSLDs. The microSTAR is a portable dosimetry system specifically designed to measure optically stimulated luminescence signal from OSLDs that use Al_2O_3:C. The customized OSLDs are Al_2O_3:C crystals ground to a fine powder, then mixed with a polyester binder and coated onto a roll of polystyrene film. The Al_2O_3:C layer is approximately 0.2 mm thick and is sandwiched between 0.03 and 0.1 mm thick polyester foil. To stimulate the luminescence of the Al_2O_3:C, Light Emitting Diodes (LED) emit light at a wavelength of 532 nm. The PMT within the microSTAR is calibrated to be most sensitive to light wavelengths 410 – 420 nm, which corresponds to the principal emission peak of Al_2O_3:C during luminescence (Perks et al., 2008). When reading dose from OSLDs, studies found the number of counts with respect to dose measured by the microSTAR had a linear response up to 600 cGy (Schembri & Heijmen, 2007; Viamonte et al., 2008) and a slight non-linear response above 600 cGy, which can be fitted with a quadratic equation (Jursinic, 2007). The microSTAR is a valuable tool for radiotherapy because the customized OSLDs can be repeatedly read, allowing them to be archived with patient records as permanent documents. Unlike TLDs, OSLDs can be read within minutes of exposure and do not lose all dosimetric information after reading. Compared to electronic detectors like Diodes and MOSFETs, OSLDs require no cabling and are relatively inexpensive. Additionally, the microSTAR system does not require a medical physicist to operate and can be used in mammography, diagnostic and CT fields, making it suitable for both patient dosimetry and quality control of x-ray beams.

Conclusion

Megavoltage photon beams are often used in radiation oncology to treat cancers due to its ability to deliver dose deep into tissues while sparing the skin. A radiation oncologist adds a

bolus to the patient's surface to modulate the beam and deliver the maximum dose to the target region to treat superficially located tumors or lesions. However, conventional treatment planning software does not account for air gaps between the bolus and the patient's skin, which leads to underdosing of the tumor and overdosing of healthy tissue.

Advancements in 3D printing technology solve the challenges caused by air gaps between the bolus and the patient. 3D printing creates patient-specific boluses that conform closely to the patient's surface and minimize air gaps. FDM printing emerged as the ideal method for research because many printing parameters can be modified and controlled, and FDM printing allows for the testing and printing of novel materials.

Researchers have conducted studies using 3D-printed objects with radiosensitive filaments to test the feasibility of 3D printing in future research. The researchers integrated OSLDs with filament and print radiosensitive objects, showing that combining the two technologies offers new avenues of research in radiation therapy.

Researchers were exploring TLD materials and discovered some could make OSLDs, which provide improved dosimetry and reliability over TLDs. We discussed the physical theory explaining how Al_2O_3:C, PMTs, and the microSTAR system work and how the Al_2O_3:C OSLDs provide enhanced dosimetry and stability.

Our literature review shows how 3D printing has led to advancements in radiation oncology and the origins and benefits of OSLDs for dosimetry. Combining 3D printing applications for radiation oncology with OSLD filament may lead to innovations and address the limitations of conventional bolus materials and dosimetry challenges, potentially improving treatment accuracy and patient outcomes.

CHAPTER 1

INTEGRATING Al_2O_3:C INTO 3D PRINTABLE MATERIAL

INTRODUCTION

The advent of 3D printing is rapidly growing in the medical and veterinary radiation oncology field due to its ability to rapidly create custom models for a wide variety of research applications. There is a plethora of 3D printing methods, all with their associated advantages and disadvantages, but the fused deposition modeling (FDM) 3D printing method is of particular interest in the research field. FDM 3D printing is highly versatile because any of the inputs of the printing process, e.g., temperature, flow, speed, are controllable, and a wide range of filaments are made of various materials that suit different applications.

As discussed in the literature review, researchers applied FDM 3D printers to create patient specific devices such as boluses and incorporated an optically stimulated dosimeter (OSLD) and were able to directly measure the dose delivered to the patient (Burleson et al., 2015). Also discussed were other applications where researchers used FDM 3D printers to create radiosensitive models, such as a human ear, showing it is possible to print anatomically accurate, radiosensitive models with potential for radiation oncology applications (Hashimoto et al., 2019b). Similarly, another study was conducted where a radiosensitive cube was printed which accurately and reliably measured dose during irradiation by a 6 MV x-ray beam (Lynch et al., 2020). These advancements show the interest in using FDM 3D printing for radiation oncology applications and in developing 3D printed models to address and research challenges in radiation therapy.

Despite the advancement of printed boluses and radiosensitive models, there are some drawbacks. The 3D printed boluses that contained OSLD within them contained air gaps, which caused inaccurate dose distribution, and the OSLD can only provide point measurements. The major drawback of the 3D printed models is that they rely on radioluminescence for dose measurements. Radioluminescence measurements require specialized equipment to read and interpret the luminescent signal to calculate the absorbed dose. Additionally, the measurements must occur simultaneously with irradiation, which makes them less practical for many clinical applications.

To address the limitations, a novel radiosensitive filament was developed by incorporating Al_2O_3:C crystals, a well-characterized material used to make commercially available OSLDs, with thermoplastic polyurethane (TPU), a material used to 3D print boluses. This novel OSLD filament will allow for the creation and printing of 3D printed OSLD boluses and other models, which can be read with a commercially available reader, the LANDAUER microSTAR. The stability of Al_2O_3:C crystals within the printed object allows for post-irradiation measurements, increasing its applications in radiation oncology. Combining Al_2O_3:C crystals with TPU for FDM 3D printing offers significant advancement in radiation dosimetry.

This work demonstrates the feasibility of integrating active Al_2O_3:C crystal into commercially available 3D printable filament. This is the first investigation of this type. Incorporating OSLD into 3D filament allows the creation of an OSLD in any desired shape. In radiation oncology or radiology, it is essential to minimize air gaps (Martin et al., 2020). Often, tiny dosimeters such as film, TLD, or OSLD are used to get close to point dose measurements. However, these tiny dosimeters do not measure the distribution of the radiation field itself (Ezzell et al., 2003). The ability to measure 3D dose has been a challenge in polymer gels due to

unintended mixing and dose reading challenges (Watanabe et al., 2019). It is believed that incorporating active dosimetry crystal into 3D filament may offer a helpful alternative to these clinical challenges.

METHODOLOGY

Construction of Optically Stimulated Luminescence Filament

Three-dimensional optically stimulated luminescence dosimeter (OSLD) filament was created in this work by combining standard NinjaFlex 85A Filament (Fenner Precision Polymers, Lititz, Pennsylvania, USA), a material used to 3D print boluses (Martin et al., 2020), with commercial Al_2O_3:C. The active Al_2O_3:C crystal was removed from commercially available LANDAUER nanoDots (LANDAUER, Glenwood, Illinois, USA) and mixed with NinjaFlex filament in a Filabot EX2 extruder (Filabot, Barre, Vermont, USA). The Filabot is simple in design, where heat is controlled and applied to the ingredients in the hopper. The contents are mixed via a rate-controlled worm screw and extruded through a selected bore size through the extrusion nozzle to make a new filament (Figure 7).

Uniformity of the active OSLD crystal distribution within the printable filament is a key issue and challenge. In our work, handheld scissors were used to cut 3 mm diameter NinjaFlex TPU into pellets about 1 mm long or smaller. The bulk concentration of the OSLD crystal (including the polystyrene substrate) to pelletized printable filament was approximately 1:90. The OSLD crystal was obtained by removing the polystyrene dot from LANDAUER nanodot holders, and the polystyrene dots were cut into small pieces to allow for optimal mixing distribution of Al_2O_3:C within the 3D printing filament. These contents were premixed as much as possible, placed into the Filabot EX2 extruder set to 180 ℃, and left to preheat for 40 minutes. After preheating, the new filament was created with the extrusion screw set to 1/6 of the max extrusion speed. After all the material in the hopper had been extruded and left to cool, the new extruded filament was pelletized again into 1 mm segments. The pellets were collected and placed in the hopper again and re-extruded.

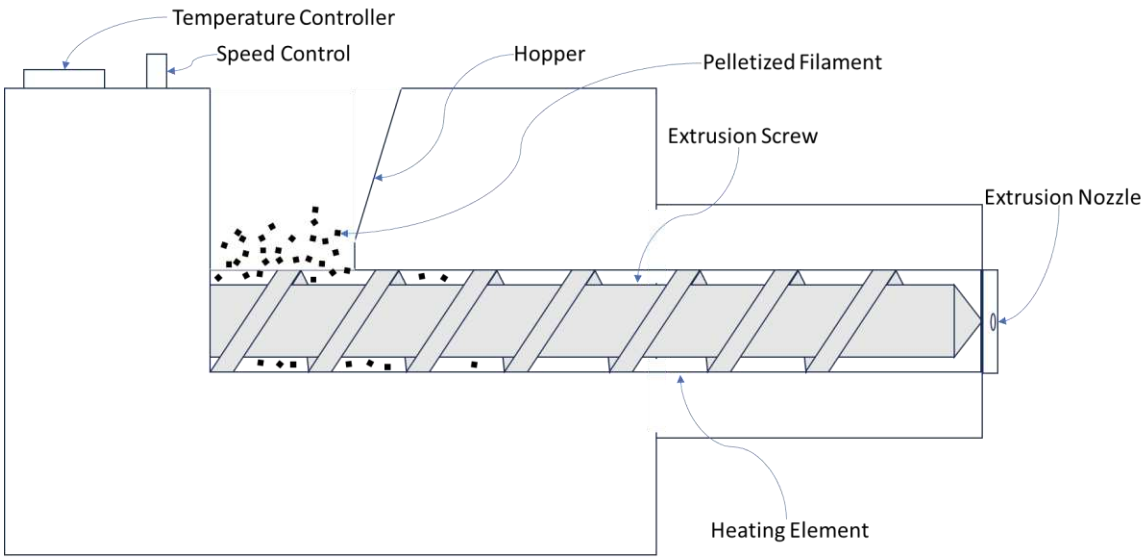

Figure 7: Diagram of the Filabot EX2 extruder.

The OSLD printed filament was formed into a thin 8 mm diameter disk, similar in dimension to the LANDAUER nanoDots. The LANDAUER dot (LD) dosimeters and the filament dot (FD) dosimeters were irradiated identically using a Precision Small Animal Radiation Therapy irradiator (Precision X-Ray Irradiation, Madison, Connecticut, USA). The radiation was delivered to the dosimeters, which were placed on SuperFlab (to provide backscatter) at isocenter with a 40 mm × 40 mm square collimator, set to 225 kVp, with a current of 13 mA, and a 0.3 mm copper filter.

The Precision Small Animal Radiation Therapy irradiator was used to deliver the dose using kV photons rather than MV photons because the LDs dose response is independent of photon energies (Belhaj et al., 2023), and the Precision Small Animal Radiation Therapy irradiator was more readily available. The delivered dose is controlled by units of time where, under the stated conditions, the minimum incremental dose is 6.45 cGy for 1s.

Evaluation of Optically Stimulated Luminescence Filament

A LANDAUER microSTAR reader was used to read the recorded dose on the LD and FD dosimeters. The dots are placed in a LANDAUER InLight holder so that they may be measured. The InLight holder is a light-tight plastic rectangle with a plastic slide with four 7 mm diameter holes. The slide can move in and out of the light-tight rectangle. The plastic slide of the InLight holder extends out and positions 1 of the 4 dots between the stimulating laser and the PMT. The holes in the slide allow light from the stimulating laser to hit the dosimeters, allowing the luminescence light to travel out the other side to the PMT. The LDs were pressed onto the slide and securely fastened because the holes in the slide had small protrusions that held onto the LDs. The FD dosimeters were kept in position by lightly coating the edges of the slide's holes with Elmers Liquid School Glue (Elmer's Products, Inc., Westerville, OH, USA). The glue unlikely affected any measurements by blocking light from the stimulating laser or luminescing light because the slide places the dot behind a 5 mm diameter aperture. The glue was put on the edge of the 7 mm hole so no glue would ever be in the path of the stimulating laser or luminescence light. The glue prevented any FDs from falling off the slide during measurement. The fading characteristics over successive readings, the dots' uniformity (or consistency), how closely measurements follow generated fits, and the upper dose limit the dots could measure dose before saturation were all evaluated.

Linearity of LANDAUER Dot and Filament Dot Dosimeters

Initially, to determine if the FDs could function as dosimeters and had dosimetric properties similar to the LDs, four doses, 51.6, 103.2, 148.38, and 199.95 cGy, were delivered to four individual LDs and FDs and read 10 successive times. The doses were chosen because previous studies have shown that the LDs have a linear response in their number of counts

respective to dose when exposed to a dose of up to 300 cGy (Jursinic, 2007). It was unknown at the time if the TPU would affect the properties of the Al2O3:C, such as changing the range of the linear dose-response of the Al_2O_3:C, so choosing higher or lower doses may have introduced uncertainties. The average of the 10 readings was taken and plotted with a linear fit to determine if the FDs had a similar linear response to the dose as the LDs.

Signal Fading

Four doses, 51.6, 103.2, 148.38, and 199.95 cGy, were delivered to four individual LDs and FDs, then read at least 100 successive times and plotted with an exponential decay fit. Previous studies of Al_2O_3:C had found repeated readings cause the signal to decrease by 0.05% per reading using an exponential decay model (Jursinic, 2007). This type of decay suggests a multiplicative process rather than a subtractive one- each measurement is a fraction of the previous one which is characteristic of exponential decay. Therefore, another exponential decay model was generated to evaluate the signal fading of the LDs and FDs.

Uniformity of LANDAUER Dot and Filament Dot Dosimeters

The uniformity of the Al_2O_3:C crystal distribution was determined by exposing 16 LDs and FDs to a range of doses from 303.15 cGy up to 1651.2 cGy. The specific doses were 303.15, 399.9, 503.1, 59985, 703.05, 799.8, 999.75, 1102.95, 1206.15, 1296.15, 1399.65, 1548, 1599.6, and 1651.2 cGy. The averages of 10 measurements per dot were plotted, a quadratic fit was generated, and an R^2 value of the fit was calculated. Previous studies characterizing Al_2O_3:C found a quadratic fit to be most appropriate while measuring doses at or greater than 300 cGy (Jursinic, 2007). In addition, each dot was normalized to counts/dose to compare the respective distributions between a sample batch of LDs vs FDs and associated characteristic means and standard deviations.

Assessment of Data Fits for LANDAUER Dot and Filament Dot Dosimeters Exposed to Low Doses

Previous studies have found that the signal response of Al_2O_3:C OSLDs increased linearly with respect to exposed doses up to 300 cGy (Jursinic, 2007; Schembri & Heijmen, 2007; Viamonte et al., 2008). To assess whether the signal response of the LDs and FDs was linear, four LDs and FDs were repeatedly given an incremental dose up to a total dose of 51.6 cGy by placing the dots in a 40 × 40 mm, 225 kV, and 13 mA x-ray beam in the small animal irradiator for 1 second. The specific dose steps were: 0, 6.45, 12.9, 19.35, 25.8, 32.25, 38.7, 45.15, and 51.6 cGy. After each exposure, every dot was read a minimum of five times. The readings for each dosimeter at each dose were averaged and plotted. Both linear and quadratic fits were generated and an R^2 value for each fit was calculated and used to determine the goodness of fit.

Dose Range and Saturation of LANDAUER Dot and Filament Dot Dosimeters

Saturation is when all the dosimetric traps within the Al_2O_3:C crystals are filled, and no more dosimetry information can be collected. To determine the dose for which saturation occurs 4 LDs and FDs were repeatedly exposed to an incremental dose up to a total dose of 1651.2 cGy. The total doses were: 0, 51.6, 96.75, 199.95, 303.15, 399.9, 503.1, 599.85, 703.05, 799.8, 999.75, 1102.95, 1206.15, 1296.15, 1399.65, 1548, 1599.6, and 1651.2 cGy. The final dose of 1651.2 cGy was chosen because LANDAUER claims the LDs saturate when exposed to doses greater than 1500 cGy (*nanoDot™ - Dosimetry Badges | LANDAUER*, n.d.). The dose increment was reduced from 100 cGy to 50 cGy after 1500 cGy was exceeded to more precisely determine if the saturation occurred at exactly 1500 cGy or some other total dose. After each exposure, every dot was read a minimum of five times. The readings of each dosimeter at each dose were

averaged and plotted. A quadratic fit was generated and an R^2 value was calculated and used to determine the goodness of fit.

Statistical Analysis

Standard Deviation of a Single Measurement

When analyzing the data of a single measurement, it is necessary to calculate the standard deviation, σ, as it is a useful index of the degree of scatter within the data. To calculate the standard deviation some assumptions must be made. All measurements were made with the microSTAR, which measured luminescing light, and when measuring light with a PMT, the number of detected photons is determined by Poisson distribution (de Haas & Dorenbos, 2011). Further, the number of counts was the only measurement of the luminescing light for a single measurement so we must assume that the mean of the measurement distribution is equal to the single measurement, or $\bar{x} = x$. We can conclude that when the model is Poissonian $\sigma = \sqrt{\bar{x}}$, and $\bar{x} = x$ because x is our only measurement which $\bar{x}$ can be based. Therefore, the standard deviation being equal to x is the best estimate of deviation for a single measurement, $\sigma = \sqrt{x}$ (Knoll, 2010).

$$\text{Standard Deviation} = \sqrt{\text{Counts}}$$

All plots showing the number of counts for a single measurement include error bars representing the standard deviation, which is equal to the square root of the number of counts.

Standard Deviation of Averages

When calculating the averages we have a total number of counts measured by the microSTAR after reading the dosimeters N number of times. The counts from each measurement are designated as x_1, x_2, …, x_N, and the sum of the counts from all measurements is equal to Σ.

$$\Sigma = x_1 + x_2 + \ldots + x_N$$

When the error of the independent measurements, σ_{xN}, is applied to the sum the expected error of the sum, σ_Σ, is

$$\sigma_\Sigma^2 = \sigma_{x1}^2 + \sigma_{x2}^2 + \cdots + \sigma_{xN}^2$$

And since $\sigma_{xN} = \sqrt{x_N}$ for each count σ_Σ^2 is

$$\sigma_\Sigma^2 = x_1 + x_2 + \ldots + x_N$$

So

$$\sigma_\Sigma = \sqrt{\Sigma}$$

This shows the standard deviation for the sum of all counts is as if the sum had been measured from a single measurement.

The mean value of all the measurements is simply the sum divided by the number of measurements.

$$\bar{x} = \frac{\Sigma}{N}$$

This is an error-associated quantity divided by a constant, so the expected standard error of the mean is

$$\sigma_{\bar{x}} = \frac{\sigma_\Sigma}{N} = \frac{\sqrt{\Sigma}}{N} = \frac{\sqrt{N\bar{x}}}{N}$$

$$\sigma_{\bar{x}} = \sqrt{\frac{\bar{x}}{N}}$$

(Knoll, 2010).

When we apply this to the context of this experiment the standard deviation of the averages is

$$\text{Standard Deviaion of Averages} = \sqrt{\frac{\text{Average Counts of Measurements}}{\text{Number of Measurement}}}$$

Linear, Exponential, and Quadratic Goodness of Fit

A coefficient of determination, R^2, is calculated to analyze all figures. An R^2 value is often calculated to evaluate the goodness of fit for the generated fits of many models, and the calculated R^2 value was used to evaluate the generated fits. The R^2 value ranges from 0 to 1, and the closer to 1 the R^2 value, the greater the goodness of fit and the more closely the fit follows the data (Colin Cameron & Windmeijer, 1997). R^2 values indicate how predictable LD or FD dosimeters will respond to a known dose or how predictable the signal of the LD or FD dosimeters will fade over a known number of measurements.

F-Test Using R^2 Values

To determine if the differences in the generated linear and quadratic fits for the low dose measurements of the LD and FD dots are statistically significant or not, the F statistic, F, is calculated and compared to the F critical value. The F statistic provides a quantitative measure to determine if the differences in R^2 values between the generated fits are significant. The formula to calculate the F statistic is as follows:

$$F = \frac{(R^2_{Quadratic} - R^2_{Linear}) \Big/ (k_{Quadratic} - k_{Linear})}{(1 - R^2_{Quadratic}) \Big/ (n - k_{Quadratic} - 1)}$$

Where $R^2_{Quadratic}$ and R^2_{Linear} are the R^2 values of the quadratic and linear fits, $k_{Quadratic}$ and k_{Linear} are the number of predictors in each fit equation, and n is the number of measurements in the data set. The F statistic is calculated and if it is larger than the critical value then the difference between the linear and quadratic fits is significant. The critical value is determined by setting a significance level, α, to 0.05 and using an F Distribution table for α = 0.05, determining the degrees of freedom, and selecting the critical value from the table. There are two degrees of freedom in the F Distribution Table and the degrees of freedom in the

columns are equal to $k_{Quadratic} - k_{Linear}$ and the degrees of freedom in the rows are equal to $n - k_{Quadratic} - 1$. When $\alpha = 0.05$ and the F statistic is larger than the critical value there is a 95% chance the difference in quadratic, and linear fits is statistically significant (Sureiman & Mangera, 2020).

Signal Fading

The fading characteristics of the LD and FD dosimeters were evaluated by calculating their respective average percent signal loss per measurement. The average percent signal loss per measurement for a dosimeter was calculated by taking the number of counts from the initial measurement and subtracting the counts from the following measurement to find the signal loss in a number of counts.

$$\text{Signal Loss (counts)} = \text{Initial Reading (counts)} - \text{Next Reading (counts)}$$

The signal loss was converted to a percentage of the initial measurement by dividing the signal loss counts by the initial measurement counts and multiplying by 100.

$$\text{Signal Loss (percentage)} = \frac{\text{Signal Loss (counts)}}{\text{Initial Reading (counts)}} \times 100$$

The signal loss percentage for each measurement was calculated for all measurements and then averaged to calculate the average percent signal loss.

$$\text{Average Signal Loss for All Readings (percetage)} = \frac{\text{Signal Loss Reading Number 1 (percentage)} + \cdots + \text{Signal Loss Reading Number N (percentage)}}{\text{N}}$$

Uniformity of LANDAUER Dot and Filament Dot Dosimeters

The average counts of LD and FD dosimeters exposed to 303.15 – 1651.2 cGy were plotted with respect to the exposed dose and a quadratic fit was generated. The R^2 value was also

calculated to evaluate the goodness of fit of the generated quadratic fit. The generated quadratic fit was used to calculate the predicted counts of a dosimeter for a given dose.

$$\text{Predicted (counts)} = \text{K}_1 \times \text{dose(cGy)}^2 + \text{K}_2 \times \text{dose (cGy)} + \text{K}_3$$

Where K_1 and K_2 and K_3 are the various constants of the quadratic fit.

The difference in counts between predicted counts was calculated by taking the absolute value of the predicted counts minus the average counts.

$$\text{Difference (counts)} = |\text{Predicted (counts)} - \text{Average (counts)}|$$

The percentage difference between the predicted counts and the average of the measured counts was calculated by dividing the difference in counts by the predicted counts and multiplying by 100.

$$\text{Percent Difference} = \frac{\text{Difference (counts)}}{\text{Predicted (counts)}} \times 100$$

Saturation

Saturation is when all the dosimetric traps within the Al_2O_3:C crystals are filled, and no more dosimetry information can be collected with the Al_2O_3:C crystal. When the dosimeters have not reached saturation, they can still measure increasing doses. In the unsaturated state, the dosimeters' count increases for each additional cGy of dose. This can be represented as the slope between points on a plot. When the dosimeters have reached saturation or approach saturation, the number of counts per cGy of dose decreases, and the slope between the points on the plot decreases and approaches zero.

$$\text{Slope Between Doses } (\frac{\text{counts}}{\text{cGy}}) = \frac{\text{Higher Dose (counts)} - \text{Lower Dose (counts)}}{\text{Higher Dose (cGy)} - \text{Lower Dose (cGy)}}$$

RESULTS

Linearity of LANDAUER Dot and Filament Dot Dosimeters Exposed to 51.6 – 199.95 cGy

The 4 LDs were exposed to 51.6, 103.2, 148.35, and 199.95 cGy, and read 10 times and averaged (Figure 8). A linear fit of the averages was generated and an R^2 value was calculated. The R^2 value of the generated linear fit was 0.99.

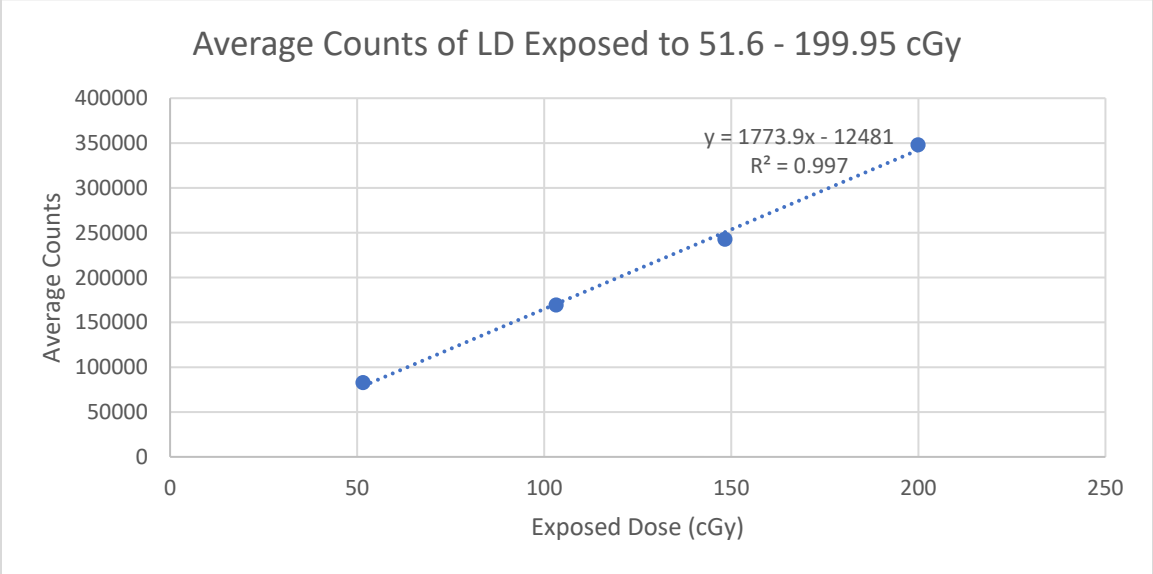

Figure 8: Average counts of 10 readings of 4 LDs after being exposed to a dose of 51.6, 103.2, 148.35, and 199.95 cGy exposed with a 40 × 40 mm, 225 kV, 13 mA x-ray beam from the small animal irradiator.

The 4 FDs were exposed to 51.6, 103.2, 148.35, and 199.95 cGy, read 10 times, and averaged (Figure 9). A linear fit was generated, and an R^2 value of the linear fit was calculated. The R^2 value of the linear fit was 0.98.

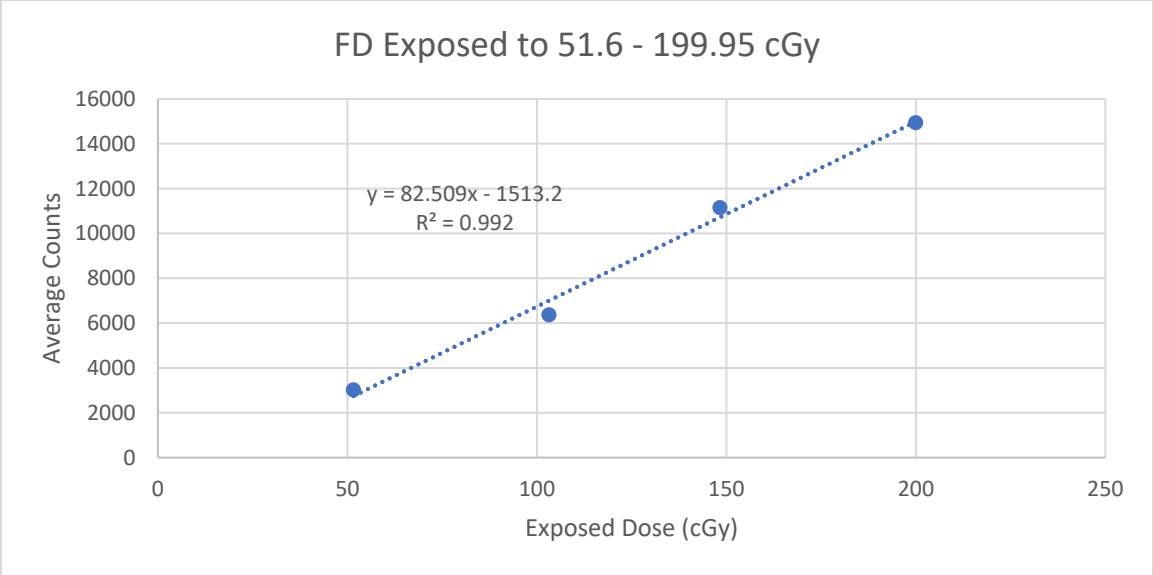

Figure 9: Average counts of 10 readings of 4 FDs after being exposed to a dose of 51.6, 103.2, 148.35, and 199.95 cGy exposed with a 40 × 40 mm, 225 kV, 13 mA x-ray beam from the small animal irradiator.

Fading Characteristics of LANDAUER Dot and Filament Dot Dosimeters

The fading characteristics of the LDs were assessed by reading the same dot with the microSTAR reader 100 times for two individual LDs exposed to 51.6 and 103.2 cGy and 99 times for two individual LDs exposed to 148.35 and 199.95 cGy (Figure 10). An exponential decay of the readings was generated for each LD, and an R^2 value was calculated. The R^2 values of the generated exponential decays are shown in Table 1.

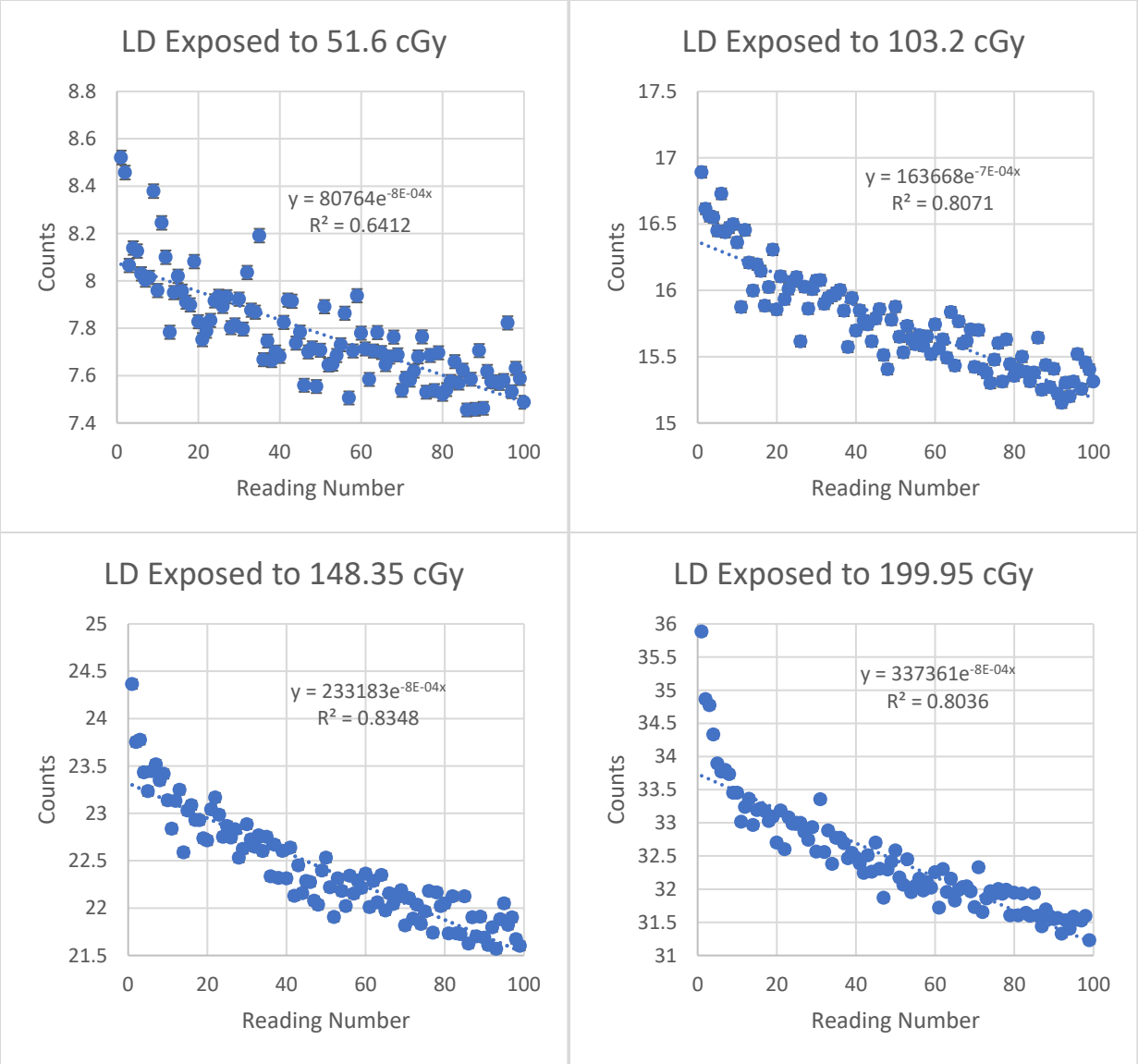

Figure 10: The number of counts measured by the LANDAUER microSTAR when reading each of the four LD dosimeters, each exposed to 51.6, 103.2, 148.35, and 199.95 cGy using a 40 × 40 mm, 225 kV, 13 mA x-ray beam from a small animal irradiator. The y-axis is scaled so that one count equals ten thousand counts.

Table 1: The calculated R^2 value of the exponential decay fit of 4 LDs exposed to 51.6,103.2, 148.35, and 199.95 cGy and read 99 or 100 times.

LD Number	Exposed Dose (cGy)	Calculated R^2 Value
1	51.6	0.64
2	103.2	0.81
3	148.35	0.83
4	199.95	0.80

Average Percent Signal Loss of LDs

The average percent signal loss per measurement for a dosimeter was calculated by taking the number of counts from the initial measurement and subtracting the counts from the next measurement to find the signal loss in number of counts:

$$\text{Signal Loss (counts)} = \text{Initial Measurement (counts)} - \text{Next Measurement (counts)}$$

$$= 85209 - 84573$$

$$= 636$$

The signal loss was converted to a percentage of the initial measurement by dividing the signal loss counts by the initial measurement counts and multiplying by 100:

$$\text{Signal Loss (percentage)} = \frac{\text{Signal Loss (counts)}}{\text{Initial Measurement (counts)}} \times 100$$

$$= \frac{636}{85209} \times 100$$

$$= 0.75\%$$

The signal loss percentage for each measurement was calculated for all measurements and then averaged to calculate the average percent signal loss. These results are summarized in Table 2.

Table 2: Average percent signal loss for 4 LDs exposed to 51.6, 103.2, 148.35, and 199.95 cGy measured 99 or 100 times.

Dose (cGy)	Average Percent Signal Loss (%)
51.6	0.11
103.2	0.09
148.35	0.12
199.95	0.14

The fading characteristics for the FDs were assessed by reading the same dot with the microSTAR reader 100 times for the 4 individual FDs exposed to 51.6, 103.2, 148.35, and 199.95 cGy (Figure 11). An exponential decay of the readings was generated for each LD, and an R^2 value for that decay was calculated. The R^2 values of the generated exponential decays were 0.9335, 0.9685, 0.983, and 0.9917 for the LD exposed to 51.6. 103.2, 148.35, and 199.95 cGy, respectively. The R^2 values of the generated exponential decays are shown in Table 3.

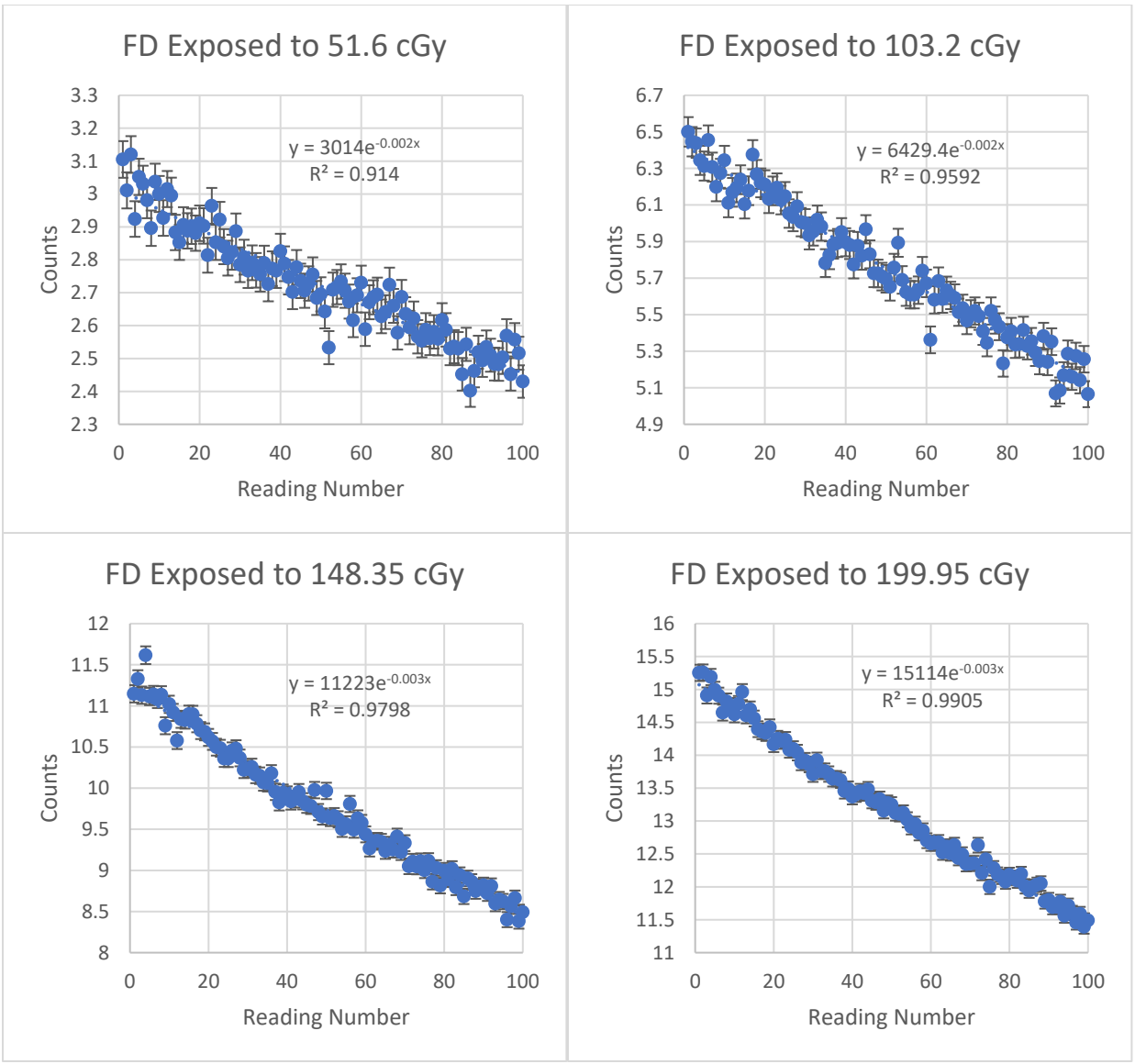

Figure 11: The number of counts measured by the LANDAUER microSTAR when reading each of the four FD dosimeters, each exposed to 51.6, 103.2, 148.35, and 199.95 cGy using a 40 × 40 mm, 225 kV, 13 mA x-ray beam from a small animal irradiator. The y-axis is scaled so that one count equals one thousand counts.

Table 3: The calculated R^2 value of the exponential decay fit of 4 FDs exposed to 51.6,103.2, 148.35, and 199.95 cGy and read 99 or 100 times.

FD Number	Exposed Dose (cGy)	Calculated R^2 Value
1	51.6	0.91
2	103.2	0.96
3	148.35	0.98
4	199.95	0.99

Average Percent Signal Loss of FDs

The average percent signal loss for all measurements for the FD dosimeters was performed the same as for the LD dosimeters, and the results are shown in Table 4.

Table 4: Average percent signal loss for 4 FDs exposed to 51.6, 103.2, 148.35, and 199.95 cGy measured 100 times.

Dose (cGy)	Average Percent Signal Loss (%)
51.6	0.22
103.2	0.24
148.35	0.26
199.95	0.28

The average percent signal loss for the 4 LDs and FDs exposed to 51.6, 103.2, 148.35, and 199.95 cGy was averaged for all dosimeters. The resulting average percent signal loss per reading for the LD and FD dosimeters is shown in Table 5.

Table 5: Average percent signal loss per reading of 4 LDs and 4 FDs exposed to 51.6, 103.2, 148.35, and 199.95 cGy and read 99 or 100 times.

Dosimeter	**Average Percent Signal Loss Per Reading (%)**
LD Dosimeter	0.11
FD Dosimeter	0.25

The relative difference in signal loss between the LDs and FDs was found by subtracting the average percent signal loss per reading of the FD dosimeter by the LD dosimeter and then dividing that difference by the average percent signal loss of the LD dosimeter. The result was multiplied by 100 to give a percent difference in the average loss per signal reading between the LD and FD dosimeters:

$$\text{Percent Difference} = \frac{\text{Average Percent Signal Loss FD Dosimeter} - \text{Average Percent Signal Loss LD Dosimeter}}{\text{Average Percent Signal Loss LD Dosimeter}} \times 100$$

$$= \frac{0.25 - 0.11}{0.11} \times 100$$

$$= 127.27\%$$

Uniformity of LANDAUER Dot and Filament Dot Dosimeters

Sixteen LDs were exposed to 303.15, 399.9, 503.1, 599.85, 703.05, 799.8, 903, 999.75, 1102.95, 1206.15, 1296.45, 1399.65, 1496.4, 1548, 1599.6, and 1651.2 cGy and then read 10

times using the LANDAUER microSTAR reader. The 10 readings were averaged and plotted with respect to the exposed dose (Figure 12). A quadratic fit was generated, and an R^2 value of the linear fit was calculated to be 0.99.

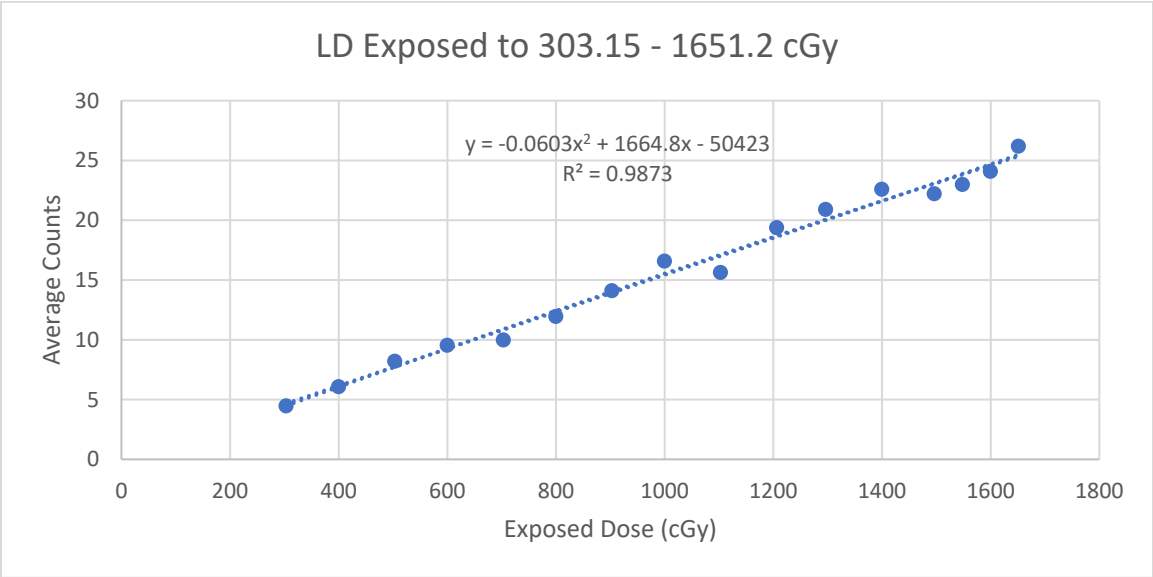

Figure 12: The average counts of 16 LD which were exposed to a 303.15, 399.9, 503.1, 599.85, 703.05, 799.8, 903, 999.75, 1102.95, 1206.15, 1296.45, 1399.65, 1496.4, 1548, 1599.6, and 1651.2 cGy by placing the dots in a 40 × 40 mm, 225 kV, and 13 mA x-ray beam in the small animal irradiator for various periods and then read with the microSTAR reader 10 times and then averaged. The y-axis is scaled so that one count is equal to 100,000 counts.

Sixteen FDs were exposed to the same doses as the previous 16 LDs and then read 10 times each. All the counts were averaged and plotted with respect to the exposed dose (Figure 13). A quadratic fit of the plot was generated, and an R^2 value of the fit was calculated to be 0.79.

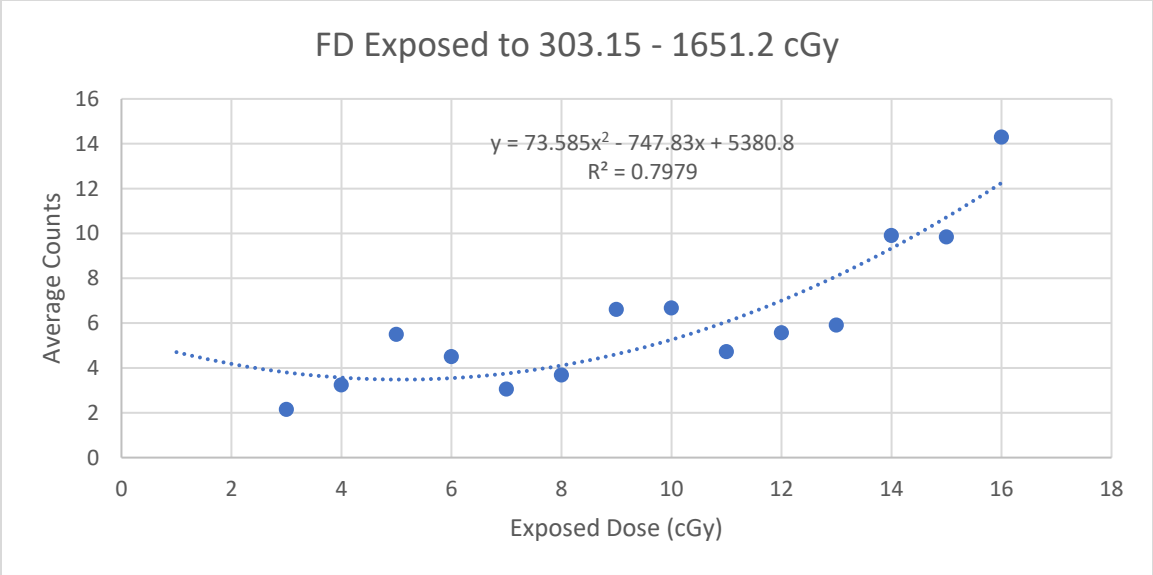

Figure 13: The average counts of 16 FDs which were exposed to 303.15, 399.9, 503.1, 599.85, 703.05, 799.8, 903, 999.75, 1102.95, 1206.15, 1296.45, 1399.65, 1496.4, 1548, 1599.6, and 1651.2 cGy by placing the dots in a 40 × 40 mm, 225 kV, and 13 mA x-ray beam in the small animal irradiator for various periods and then read with the microSTAR reader 10 times each. The y-axis is scaled so one count is equal to 1000 counts.

The generated linear fit equations in **Error! Reference source not found.** and **Error! Reference source not found.** were used to calculate the predicted counts for a given dose.

$$\text{Predicted (counts)} = K_1 \times \text{dose(cGy)}^2 + K_2 \times \text{dose (cGy)} + K_3$$

$$= -0.0603 \times (303.15\ \text{cGy})^2 + 1664.8 \times (303.15\ \text{cGy}) + (-50423)$$

$$= 448719.55\ \text{counts}$$

The average counts from the measurements were subtracted from the expected counts, and the absolute value was taken to find the difference in expected counts and average counts:

$$\text{Difference (counts)} = |\text{Expected Counts} - \text{Average Counts}|$$

$$= |448719.55\ \text{counts} - 446175.9\ \text{counts}|$$

$$= 2543.65\ \text{counts}$$

The difference is divided by the expected counts and multiplied by 100 to calculate the percent difference:

$$\text{Percent Difference} = \frac{\text{Difference (counts)}}{\text{Predicted (counts)}} \times 100$$

$$= \frac{2543.65 \text{ counts}}{448719.55 \text{ counts}} \times 100$$

$$= 0.57\%$$

The predicted counts calculated from the quadratic fit, average counts, difference in counts, and percent difference for the LDs are summarized in Table 6. The predicted counts calculated from the quadratic fit, average counts of the measurements, difference in counts, and percentage difference for the FDs are summarized in Table 7.

Table 6: The predicted counts calculated from the quadratic fit, average counts, difference in counts, and percent difference for 16 LDs exposed to 303.15, 399.9, 503.1, 599.85, 703.05, 799.8, 903, 999.75, 1102.95, 1206.15, 1296.45, 1399.65, 1496.4, 1548, and 1651.2 cGy.

Dose (cGy)	Predicted (counts)	Average (counts)	Difference (counts)	Percent Difference (%)
303.15	448719.55	446175.9	2543.65	0.57
399.9	605687.34	606692.9	1005.56	0.17
503.1	771875.37	819414.2	47538.83	6.16
599.85	926510.13	953552.1	27041.97	2.92
703.05	1090209.60	997651.8	92557.80	8.49
799.8	1242511.33	1194664.8	47846.53	3.85
903	1403722.24	1409337.1	5614.86	0.40
999.75	1553690.95	1656748.5	103057.55	6.63
1102.95	1712413.29	1561545.7	150867.59	8.81
1206.15	1869851.21	1936807	66955.79	3.58
1296.45	2006555.77	2089480.7	82924.93	4.13
1399.65	2161585.41	2257769.4	96183.99	4.45
1496.4	2305759.18	2220212.3	85546.88	3.71
1548	2382190.27	2298085	84105.27	3.53
1599.6	2458300.25	2407487.1	50813.15	2.07
1651.2	2534089.14	2617827.4	83738.26	3.30

Table 7: The predicted counts calculated from the quadratic fit, average counts, difference in counts, and percent difference for 16 FDs exposed to 303.15, 399.9, 503.1, 599.85, 703.05, 799.8, 903, 999.75, 1102.95, 1206.15, 1296.45, 1399.65, 1496.4, 1548, and 1651.2 cGy.

Dose (cGy)	Predicted (counts)	Average (counts)	Difference (counts)	Percent Difference (%)
303.15	3240.51	2143.4	1097.10	33.86
399.9	3345.59	3234.6	111.0	3.32
503.1	3536.10	5488.6	1952.50	55.22
599.85	3788.21	4502.4	714.19	18.85
703.05	4135.55	3048.4	1087.15	26.29
799.8	4534.68	3675.6	859.08	18.94
903	5038.84	6605.7	1566.86	31.10
999.75	5585.00	6666.3	1081.30	19.36
1102.95	6245.98	4721.4	1524.58	24.41
1206.15	6987.90	5560.3	1427.60	20.43
1296.45	7703.48	5906.1	1797.38	23.33
1399.65	8597.17	9902.9	1305.73	15.19
1496.4	9508.52	9836.5	327.98	3.45
1548	10023.66	14293.1	4269.44	42.59
1599.6	10559.03	9706	853.03	8.08
1651.2	11114.64	9143	1971.64	17.74

Assessment of Data Fits for LANDAUER Dot and Filament Dot Dosimeters Exposed to Low Doses

Four LDs were exposed to dose increments of 6.45 cGy by placing the LDs in a 40 × 40 mm, 225 kV, and 13 mA x-ray beam in the small animal irradiator for 1 second and reading each a minimum of 5 times after each exposure. The total doses the LDs were exposed to were 0, 6.45, 12.9, 19.35, 25.8, 32.25, 38.7, 45.15, and 51.6 cGy. The 5 measurements for each total dose were averaged for all 4 LDs and each LD and then plotted. Linear fits were generated, and the R^2 values were calculated for the averages of all 4 LDs (Figure 14) and the averages for individual LDs (Figure 15). Then quadratic fits were generated, and the R^2 values were calculated for the averages of all 4 LDs (Figure 16) and the averages for individual LDs (Figure 17). The results are summarized in Table 8.

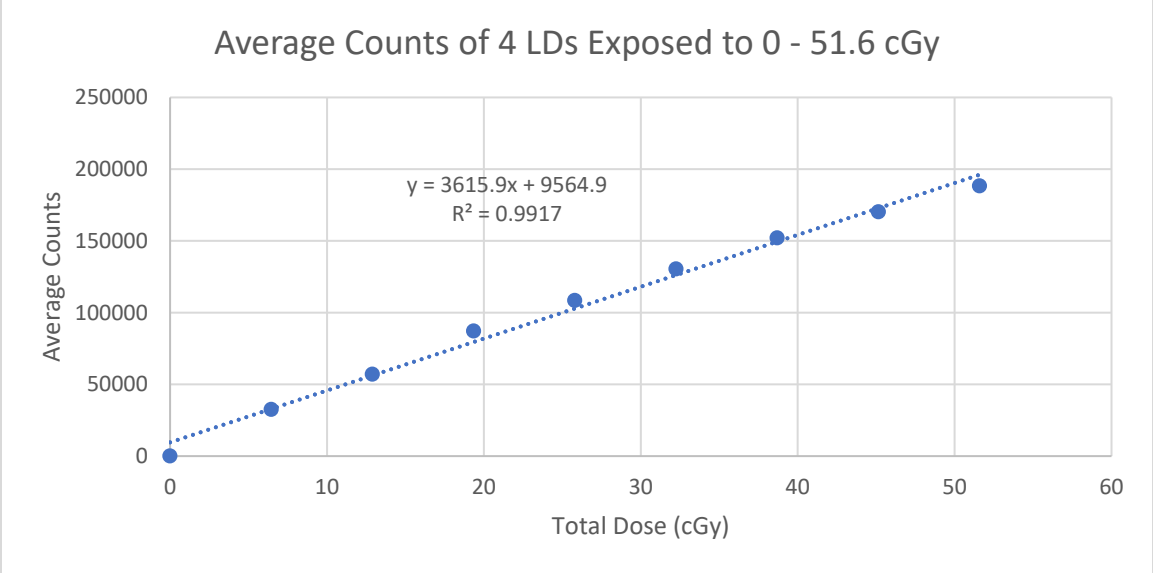

Figure 14: The average counts of all 4 LDs which were incrementally exposed to doses of 6.45 cGy for total doses of 0, 6.45, 12.9, 19.35, 25.8, 32.25, 38.7, 45.15, and 51.6 cGy by placing the dots in a 40 × 40 mm, 225 kV, and 13 mA x-ray beam in the small animal irradiator for 1 second and then read with the microSTAR reader 5 times each with a generated linear fit and calculated R^2 value.

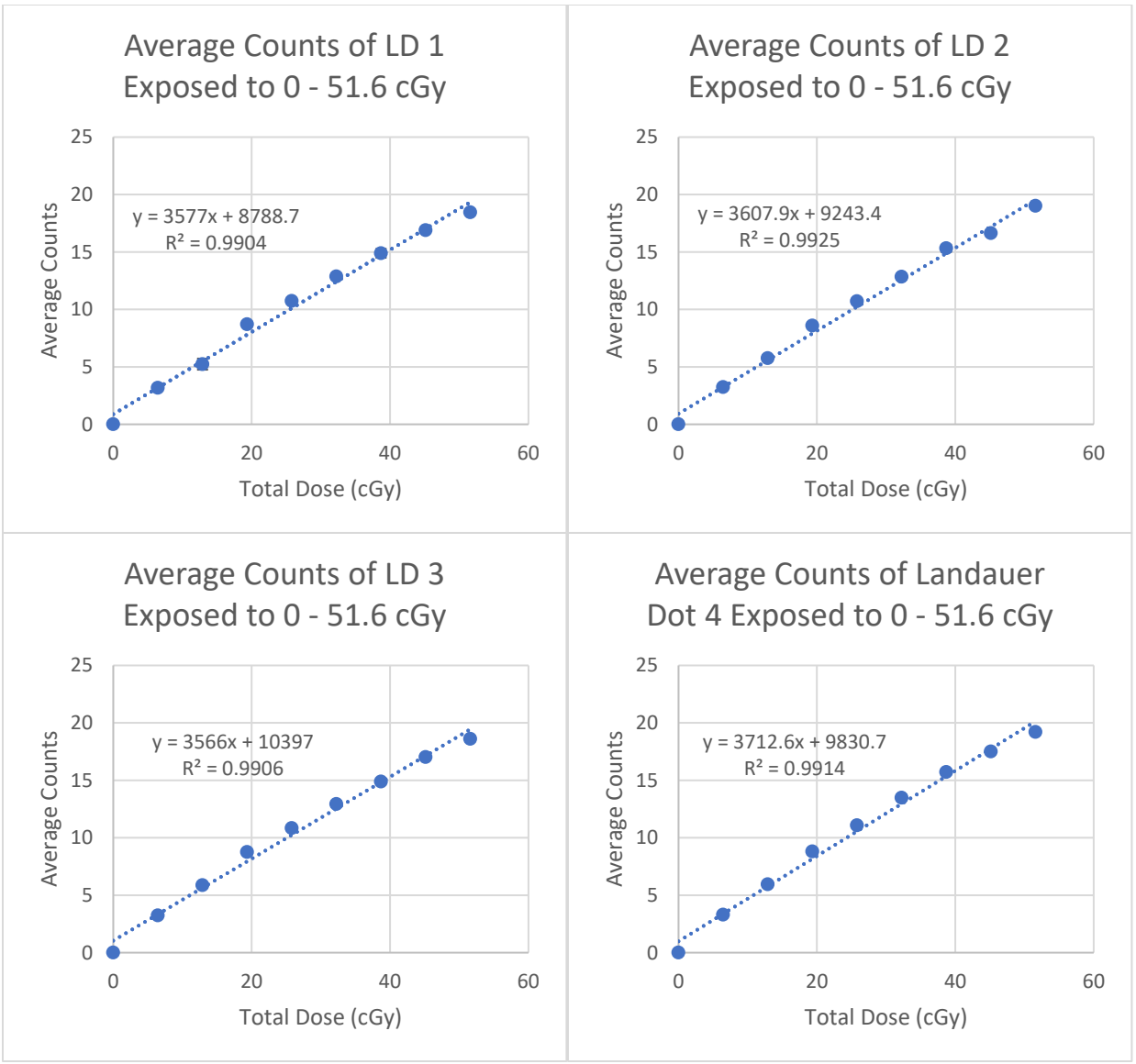

Figure 15: The average counts of LD 1, 2, 3, and 4 which were incrementally exposed to doses of 6.45 cGy for total doses of 0, 6.45, 12.9, 19.35, 25.8, 32.25, 38.7, 45.15, and 51.6 cGy by placing the dots in a 40 × 40 mm, 225 kV, and 13 mA x-ray beam in the small animal irradiator for 1 second and then read with the microSTAR reader 5 times each with a generated linear fit and calculated R^2 value. The y-axis is scaled so one count is equal to 1000 counts.

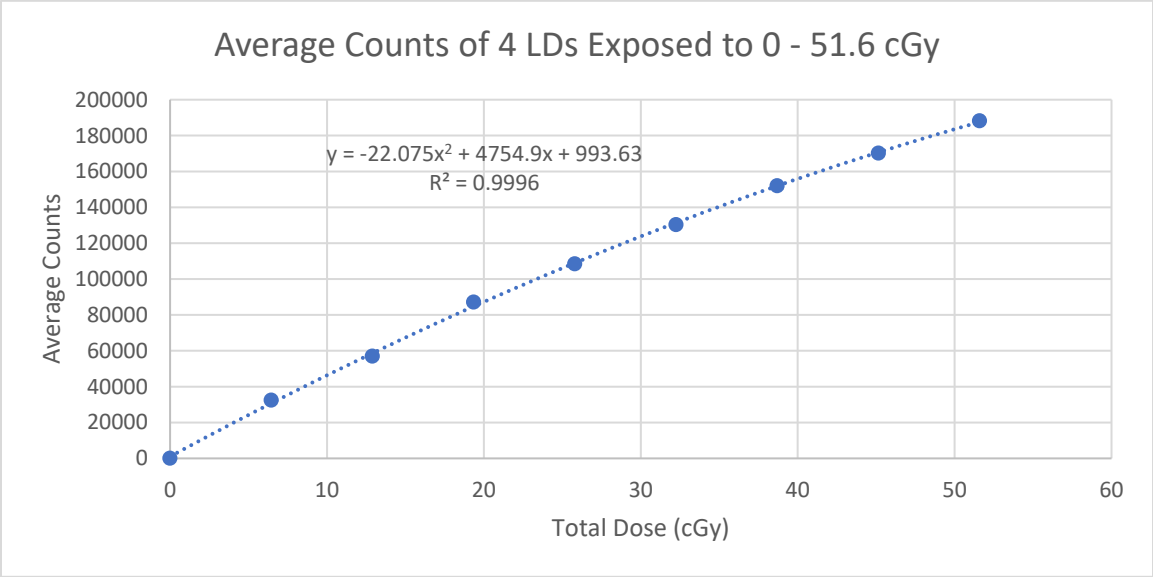

Figure 16: The average counts of all 4 LDs which were incrementally exposed to doses of 6.45 cGy for total doses of 0, 6.45, 12.9, 19.35, 25.8, 32.25, 38.7, 45.15, and 51.6 cGy by placing the dots in a 40 × 40 mm, 225 kV, and 13 mA x-ray beam in the small animal irradiator for 1 second and then read with the microSTAR reader 5 times each with a generated quadratic fit and the associated R^2 calculated value.

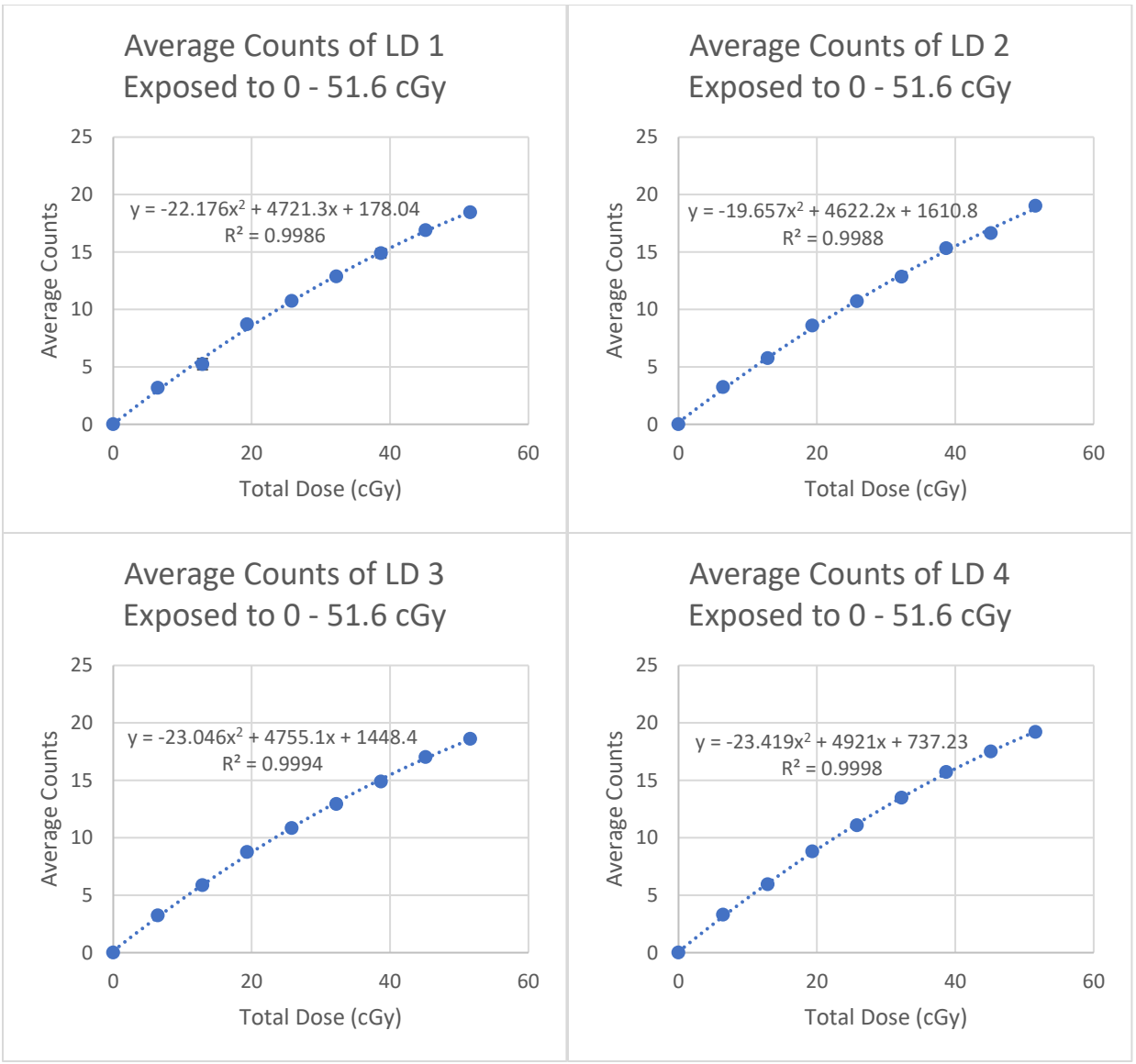

Figure 17: The average counts of LD 1, 2, 3, and 4 which were incrementally exposed to doses of 6.45 cGy for total doses of 0, 6.45, 12.9, 19.35, 25.8, 32.25, 38.7, 45.15, and 51.6 cGy by placing the dots in a 40 × 40 mm, 225 kV, and 13 mA x-ray beam in the small animal irradiator for 1 second and then read with the microSTAR reader 5 times each with a generated quadratic fit and calculated R^2 value. The y-axis is scaled so one count is equal to 1000 counts.

Table 8: Calculated R^2 values of the generated linear and quadratic fits of all 4 LDs and each LD.

LD Number	Calculated R^2 Value of the Linear Fit	Calculated R^2 Value of the Quadratic Fit
Average of All LDs	0.9917	0.9996
1	0.9904	0.9986
2	0.9925	0.9988
3	0.9906	0.9994
4	0.9914	0.9998

The F Statistic was calculated using the calculated R^2 value of the linear and quadratic fit to determine if the difference in fits is statistically significant. Below is an example calculation performed comparing the calculated R^2 value of the generated linear and quadratic fit for the Average of All LDs:

$$F = \frac{(R^2_{Quadratic} - R^2_{Linear}) \Big/ (k_{Quadratic} - k_{Linear})}{(1 - R^2_{Quadratic}) \Big/ (n - k_{Quadratic} - 1)}$$

$$F = \frac{(0.9996 - 0.9917) \Big/ (2 - 1)}{(1 - 0.9996) \Big/ (9 - 2 - 1)}$$

$$F = 37.5$$

The significance level, α, is set to 0.05 and the degrees of freedom are 1 and 6. Using an F distribution table with α = 0.05 and the degrees of freedom being 1 for the column and 6 for the row, the critical value is 5.99 (*1.3.6.7.3. Upper Critical Values of the F Distribution*, n.d.).

The F statistic was calculated for all 4 LDs and the results are summarized in Table #.

Table 9: Calculated F statistic comparing R^2 values of the generated linear and quadratic fits for 4 LDs which were incrementally exposed to doses of 6.45 cGy for total doses of 0, 6.45, 12.9, 19.35, 25.8, 32.25, 38.7, 45.15, and 51.6 cGy.

LD Number	Calculated R^2 Value of the Linear Fit	Calculated R^2 Value of the Quadratic Fit	Calculated F Statistic	Critical Value	Significant
Average of All LDs	0.9917	0.9996	37.5	5.99	Yes
1	0.9904	0.9986	35.14	5.99	Yes
2	0.9925	0.9988	31.5	5.99	Yes
3	0.9906	0.9994	88	5.99	Yes
4	0.9914	0.9998	252	5.99	Yes

Four FDs were exposed to various doses as the LDs. The FDs were exposed to dose increments of 6.45 cGy and read a minimum of 5 times after each exposure. The total doses the FDs were exposed to were 0, 6.45, 12.9, 19.35, 25.8, 32.25, 38.7, 45.15, and 51.6 cGy. The 5 measurements for each total dose were averaged for all 4 LDs and each LD and then plotted. Linear fits were generated, and the R^2 values were calculated for the averages of all 4 FDs (Figure 18) and the averages for individual FDs (Figure 19). Then quadratic fits were generated and the R^2 values were calculated for the averages of all 4 FDs (Figure 20) and the averages for individual FDs (Figure 21). The results are summarized in Table 10.

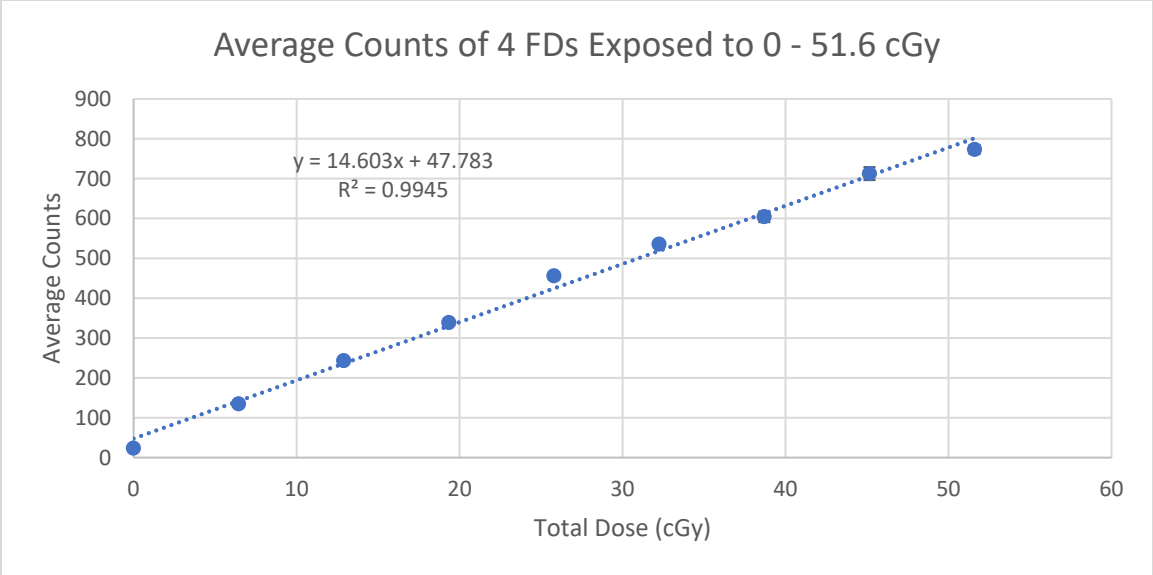

Figure 18: The average counts of all 4 FDs which were incrementally exposed to doses of 6.45 cGy for total doses of 0, 6.45, 12.9, 19.35, 25.8, 32.25, 38.7, 45.15, and 51.6 cGy by placing the dots in a 40 × 40 mm, 225 kV, and 13 mA x-ray beam in the small animal irradiator for 1 second and then read with the microSTAR reader 5 times each with a generated linear fit and calculated R^2 value.

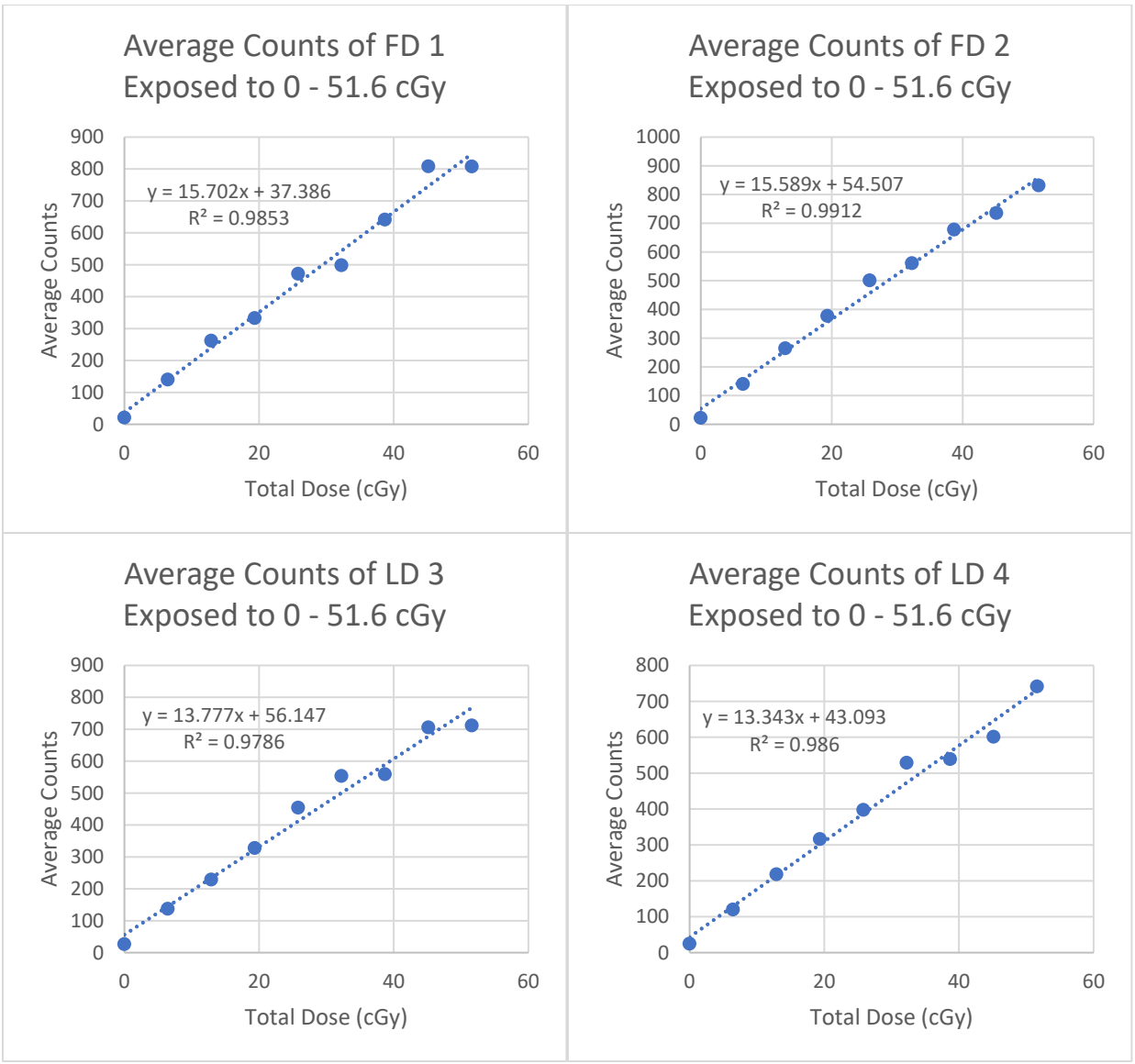

Figure 19: The average counts of FD 1, 2, 3, and 4 which were incrementally exposed to doses of 6.45 cGy for total doses of 0, 6.45, 12.9, 19.35, 25.8, 32.25, 38.7, 45.15, and 51.6 cGy by placing the dots in a 40 × 40 mm, 225 kV, and 13 mA x-ray beam in the small animal irradiator for 1 second and then read with the microSTAR reader 5 times each with a generated linear fit and calculated R^2 value.

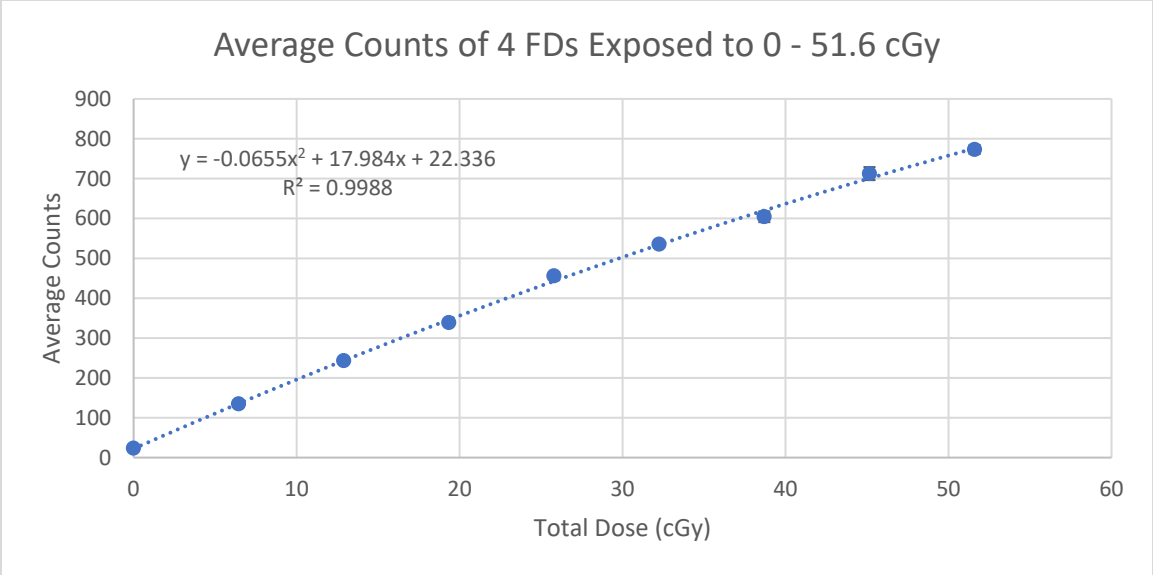

Figure 20: The average counts of all 4 FDs, which were incrementally exposed to doses of 6.45 cGy for total doses of 0, 6.45, 12.9, 19.35, 25.8, 32.25, 38.7, 45.15, and 51.6 cGy by placing the dots in a 40 × 40 mm, 225 kV, and 13 mA x-ray beam in the small animal irradiator for 1 second and then read with the microSTAR reader 5 times each with a generated quadratic fit and calculated R^2 value.

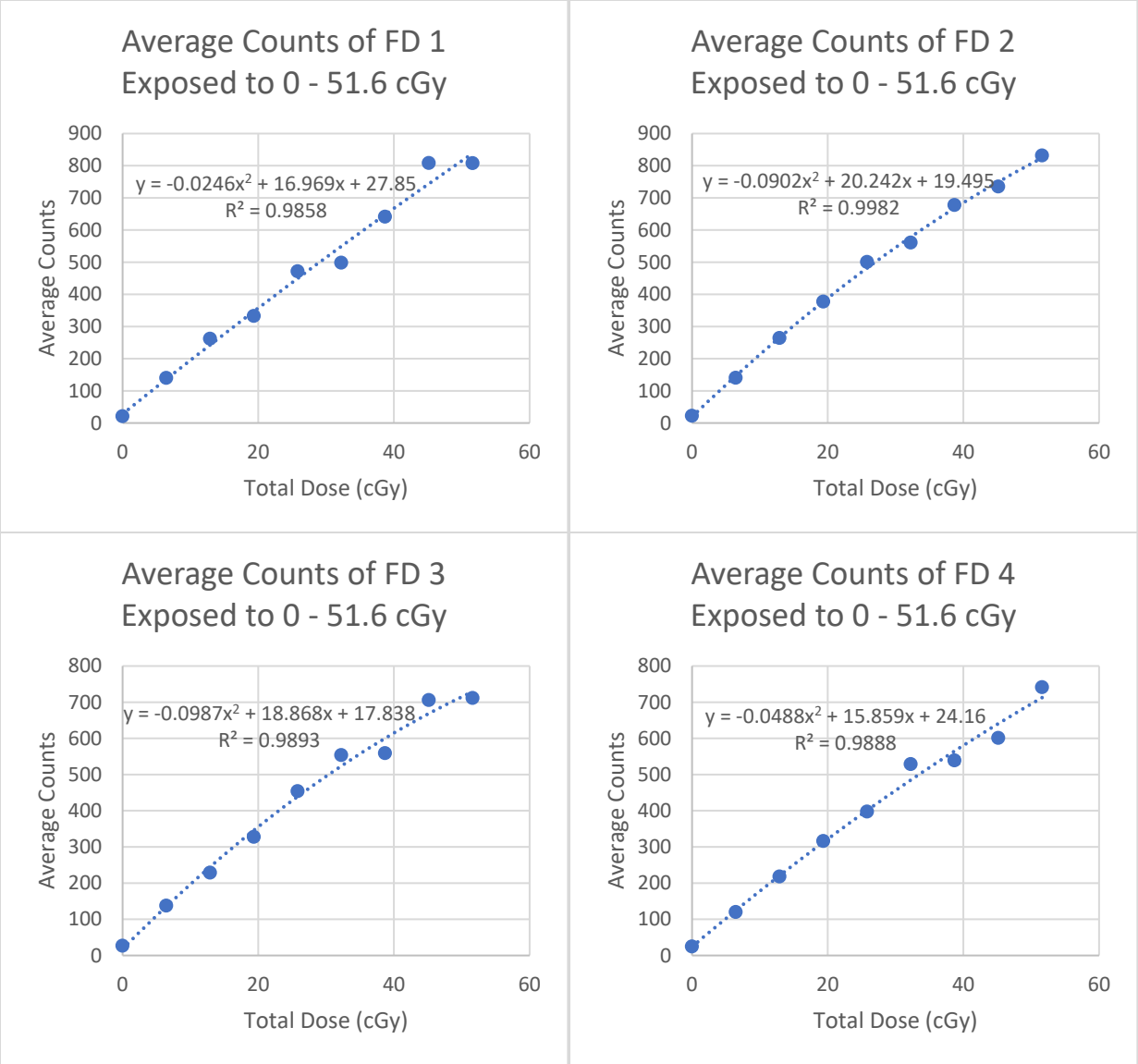

Figure 21: The average counts of FD 1, 2, 3, and 4, which were incrementally exposed to doses of 6.45 cGy for total doses of 0, 6.45, 12.9, 19.35, 25.8, 32.25, 38.7, 45.15, and 51.6 cGy by placing the dots in a 40 × 40 mm, 225 kV, and 13 mA x-ray beam in the small animal irradiator for 1 second and then read with the microSTAR reader 5 times each with a generated quadratic fit and calculated R^2 value.

Table 10: Calculated R^2 values of the generated linear and quadratic fits of all 4 FDs and each FD.

FD Number	Calculated R^2 Value of the Linear Fit	Calculated R^2 Value of the Quadratic Fit
Average of All FDs	0.9945	0.9988
1	0.9853	0.9858
2	0.9912	0.9982
3	0.9786	0.9893
4	0.986	0.9888

The F Statistic was calculated using the calculated R^2 value of the linear and quadratic fit to determine if the difference in fits is statistically significant. Below is an example calculation performed comparing the calculated R^2 value of the generated linear and quadratic fit for the Average of All FDs:

$$F = \frac{(R^2_{Quadratic} - R^2_{Linear}) \Big/ (k_{Quadratic} - k_{Linear})}{(1 - R^2_{Quadratic}) \Big/ (n - k_{Quadratic} - 1)}$$

$$F = \frac{(0.9988 - 0.9945) \Big/ (2 - 1)}{(1 - 0.9988) \Big/ (9 - 2 - 1)}$$

$$F = 21.5$$

The significance level, α, is set to 0.05 and the degrees of freedom are 1 and 6. Using an F distribution table with α = 0.05 and the degrees of freedom being 1 for the column and 6 for the row, the critical value is 5.99 (*1.3.6.7.3. Upper Critical Values of the F Distribution*, n.d.).

The F statistic was calculated for all 4 LDs and the results are summarized in Table 11.

Table 11: Calculated F statistic comparing R^2 values of the generated linear and quadratic fits for 4 FDs which were incrementally exposed to doses of 6.45 cGy for total doses of 0, 6.45, 12.9, 19.35, 25.8, 32.25, 38.7, 45.15, and 51.6 cGy.

FD Number	Calculated R^2 Value of the Linear Fit	Calculated R^2 Value of the Quadratic Fit	Calculated F Statistic	Critical Value	Significant
Average of All FDs	0.9945	0.9988	21.5	5.99	Yes
1	0.9853	0.9858	0.21	5.99	No
2	0.9912	0.9982	23.33	5.99	Yes
3	0.9786	0.9893	6	5.99	Yes
4	0.986	0.9888	1.5	5.99	No

Dose Range and Saturation of LANDAUER Dot and Filament Dot Dosimeters

Four LDs were exposed to various dose increments by placing the LDs in a 40 × 40 mm, 225 kV, and 13 mA x-ray beam in the small animal irradiator and reading each a minimum of 5 times after each exposure. The total doses the LDs were exposed to were 0, 51.6, 96.75, 199.95, 303.15, 399.9, 503.1, 599.85, 703.05, 799.8, 999.75, 999.75, 1102.95, 1206.15, 1296.15, 1399.65, 1548, 1599.6, and 1651.2 cGy. The 5 measurements for each total dose were averaged for all 4 LDs and each LD and then plotted. Quadratic fits were generated, and the R^2 values were calculated for the averages of all 4 LDs (Figure 22) and the averages for the individual LDs (Figure 23). The results are summarized in Table 12.

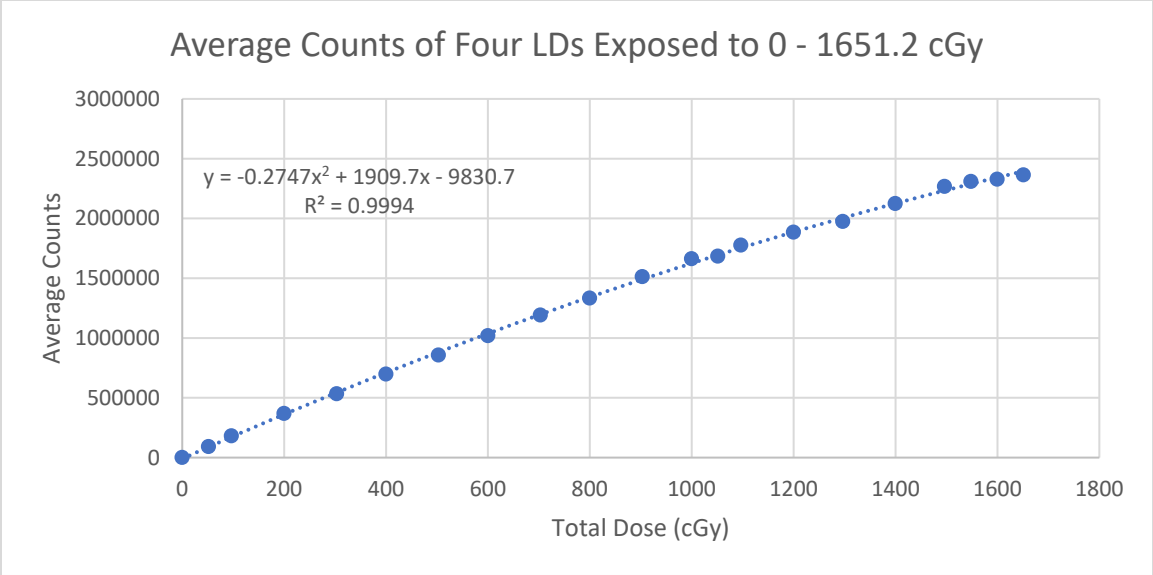

Figure 22: The average number of counts of 4 LDs exposed to 0, 51.6, 96.75, 199.95, 303.15, 399.9, 503.1, 599.85, 703.05, 799.8, 999.75, 1102.95, 1206.15, 1296.15, 1399.65, 1548, 1599.6, and 1651.2 cGy by putting the dots in a 40 × 40 mm, 225 kV, and 13 mA beam in the small animal irradiator for various periods. Each dot was measured a minimum of 5 times after each exposure.

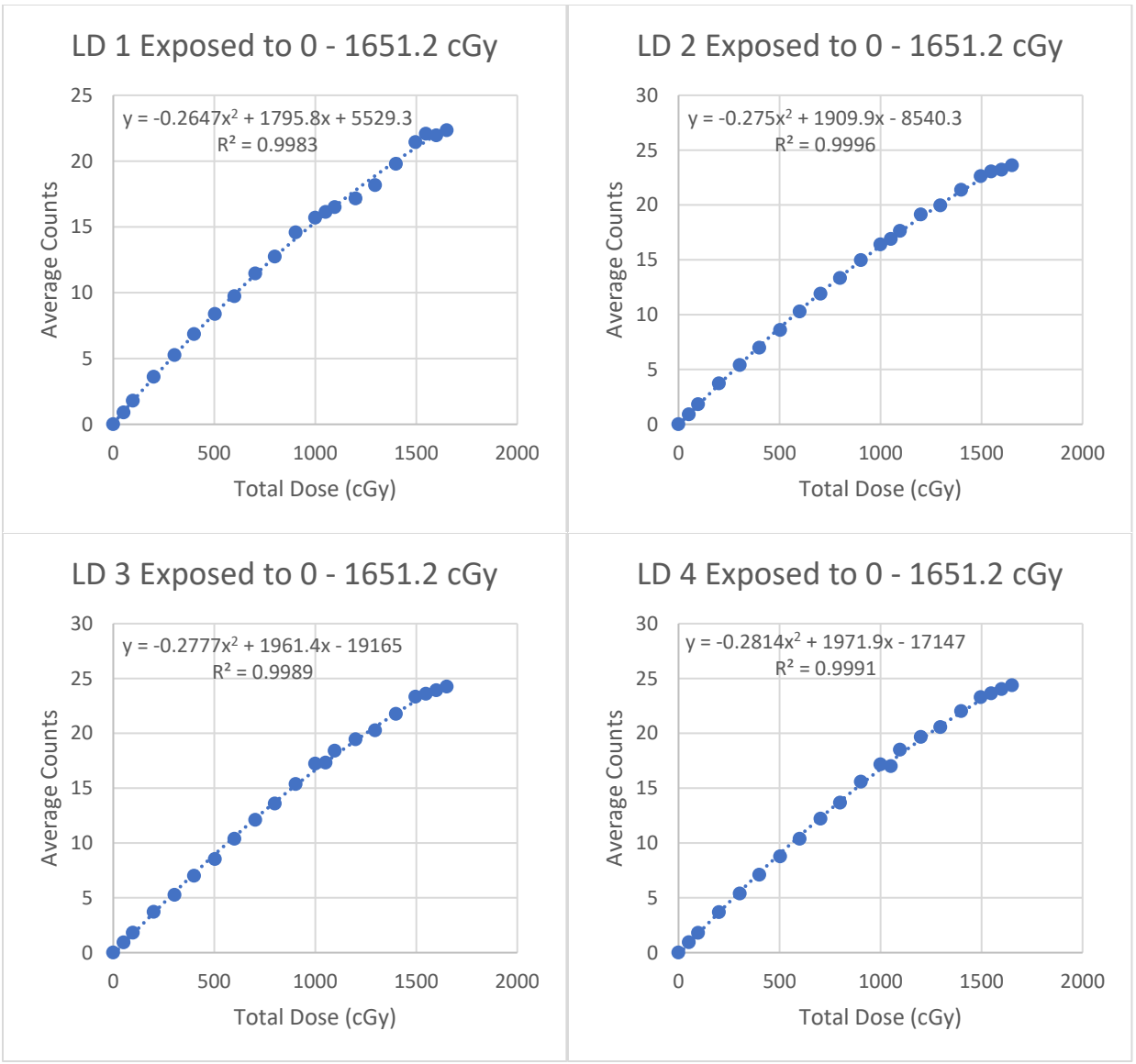

Figure 23: The average number of counts LD 1, 2, 3, and 4 exposed to 0, 51.6, 96.75, 199.95, 303.15, 399.9, 503.1, 59985, 703.05, 799.8, 999.75, 1102.95, 1206.15, 1296.15, 1399.65, 1548, 1599.6, and 1651.2 cGy by putting the dots in a 40 × 40 mm, 225 kV, and 13 mA beam in the small animal irradiator for various periods. Each dot was measured a minimum of 5 times after each exposure. The y-axis is scaled so one count equals one hundred thousand counts.

Table 12: Calculated R^2 values of the generated quadratic fits of all 4 LDs and each LD.

LD Number	Calculated R^2 Value of Generated Quadratic Fit
Average of All LDs	0.9994
1	0.9983
2	0.9996
3	0.9989
4	0.9991

Saturation Statistics

The increase in counts per additional cGy of dose was calculated by taking the counts at the new dose and subtracting the counts from the previous dose, and then dividing by the number of additional cGy the dosimeter was exposed to. This gives the slope between doses:

$$\text{Slope Between Doses} = \frac{\text{Difference In Counts}}{\text{Difference in Dose}}$$

$$= \frac{\text{Counts at } 96.75 \text{ cGy} - \text{Counts at } 51.6 \text{ cGy}}{96.75 \text{ cGy} - 51.6 \text{ cGy}}$$

$$= \frac{180958 \text{ counts} - 91774.3 \text{ counts}}{96.75 \text{ cGy} - 51.6 \text{ cGy}}$$

$$= 1975.28 \text{ counts/cGy}$$

This calculation was performed for all 4 LD dosimeters, and the averages of the 4 LD dosimeters and is shown in Table 13.

Table 13: The slope between doses (counts/cGy) for the average of all 4 LDs and each individual LD for every dose interval.

Total Dose Interval (cGy)	**Slope Between Doses of the Dosimeter (counts/cGy)**				
	Averages of LD 1-4	LD 1	LD 2	LD 3	LD 4
0 – 51.6	1777.70	1736.40	1752.07	1790.97	1831.36
51.6 – 96.75	1975.28	1979.71	2043.10	1975.09	1903.20
96.75 – 199.95	1813.49	1755.91	1841.68	1832.89	1823.49
199.95 – 303.15	1596.40	1608.70	1616.99	1507.59	1652.31
303.15 – 399.9	1711.80	1647.05	1638.36	1802.42	1759.19
399.9 – 503.1	1538.29	1480.25	1572.12	1473.13	1627.66
503.1 – 599.85	1676.65	1394.01	1736.15	1917.14	1659.31
599.85 – 703.05	1668.07	1668.93	1566.16	1661.6	1775.58
703.05 – 799.8	1464.42	1325.54	1486.64	1540.67	1504.86
799.8 – 903	1737.29	1784.52	1580.33	1727.67	1856.63
903 – 999.75	1544.69	1149.08	1480.42	1922.88	1626.37

999.75 – 1051.35	426.71	855.44	967.18	180.10	-295.90
1051.35 – 1096.5	2039.76	823.02	1622.19	2399.80	3314.030
1096.5 – 1199.7	1055.32	635.66	1443.96	1011.88	1129.76
1199.7 – 1296.45	918.28	1051.35	862.26	839.00	920.51
1296.45 – 1399.65	1452.17	1557.71	1381.21	1458.84	1410.93
1399.65 – 1496.4	1480.95	1705.12	1279.28	1618.94	1320.46
1496.4 – 1548	816.20	1251.00	833.58	502.00	678.22
1548 – 1599.6	361.21	-254.63	321.80	638.25	739.43
1599.6 – 1651.2	711.5736	758.1589	765.1085	639.6124	683.4147

Four FDs were exposed to various dose increments in the exact same manner as the 4 preceding LDs. The FDs were placed in a 40 × 40 mm, 225 kV, and 13 mA x-ray beam in the small animal irradiator, reading each a minimum of 5 times after each exposure. The total doses the FDs were exposed to were 0, 51.6, 96.75, 199.95, 303.15, 399.9, 503.1, 599.85, 703.05,

799.8, 999.75, 999.75, 1102.95, 1206.15, 1296.15, 1399.65, 1548, 1599.6, and 1651.2 cGy. The 5 measurements for each total dose were averaged for all 4 FDs and each individual FD and then plotted. Quadratic fits were generated and the R^2 values were calculated for the averages of all 4 FDs (Figure 24) and for the averages for the individual FDs (Figure 25). The results are summarized in Table 14.

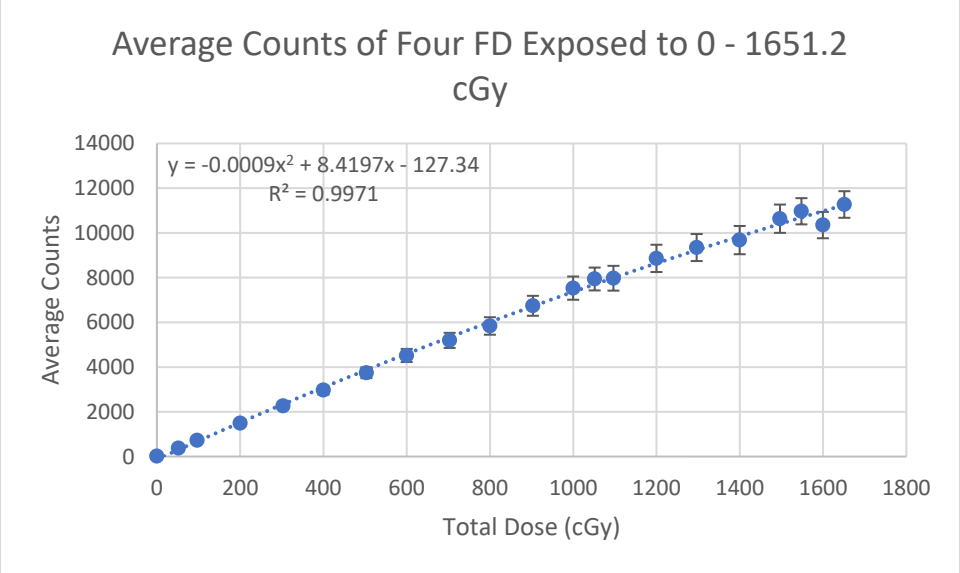

Figure 24: The average number of counts of 4 FDs exposed to 0, 51.6, 96.75, 199.95, 303.15, 399.9, 503.1, 59985, 703.05, 799.8, 999.75, 1102.95, 1206.15, 1296.15, 1399.65, 1548, 1599.6, and 1651.2 cGy by putting the dots in a 40 × 40 mm, 225 kV, and 13 mA beam in the small animal irradiator for various periods.

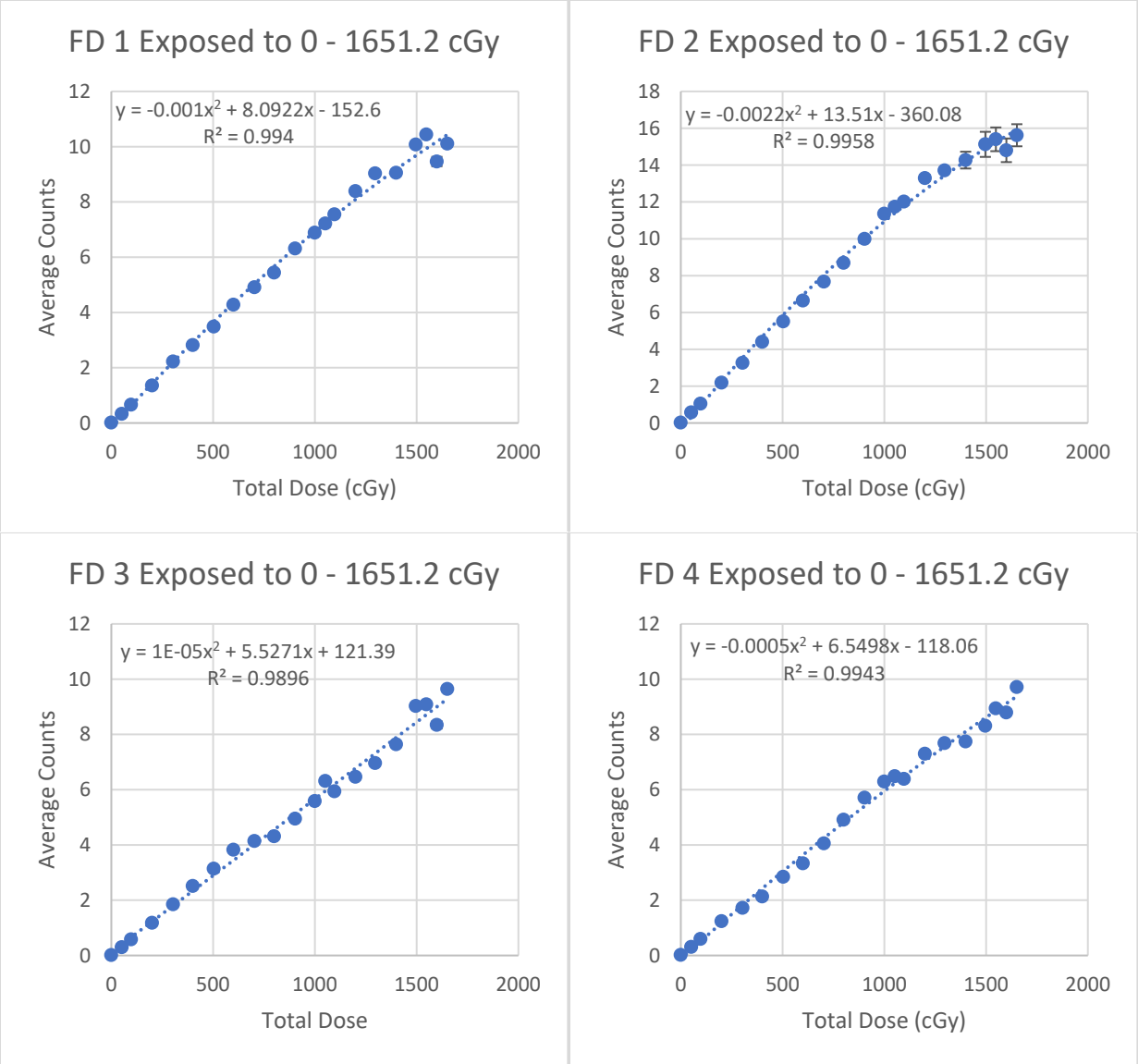

Figure 25: The average number of counts FD 1, 2, 3, and 4 exposed to 0, 51.6, 96.75, 199.95, 303.15, 399.9, 503.1, 59985, 703.05, 799.8, 999.75, 1102.95, 1206.15, 1296.15, 1399.65, 1548, 1599.6, and 1651.2 cGy by putting the dots in a 40 × 40 mm, 225 kV, and 13 mA beam in the small animal irradiator for various periods. Each dot was measured a minimum of 5 times after each exposure. The y-axis is scaled so one count is equal to one thousand counts.

Table 14: Calculated R^2 values of the generated quadratic fits of all 4 FDs and each FD.

FD Number	Calculated R^2 Value of Generated Quadratic Fit
Average of All FDs	0.9994
1	0.9983
2	0.9996
3	0.9989
4	0.9991

The same calculation to find the slope between doses at each additional exposure performed for the LD dosimeters was done for the FD dosimeters. The results are shown in Table 15.

Table 15: The slope between doses (counts/cGy) for the average of all 4 FDs and each FD for every dose interval.

Total Dose Interval (cGy)	**Slope Between Doses of the Dosimeter (counts/cGy)**				
	Averages of FD 1-4	FD 1	FD 2	FD 3	FD 4
0 – 51.6	6.97	6.07	10.72	5.51	5.58
51.6 – 96.75	7.69	7.42	10.63	6.22	6.49
96.75 – 199.95	7.45	6.71	11.05	5.83	6.20
199.95 – 303.15	7.47	8.40	10.36	6.45	4.66
303.15 – 399.9	7.29	6.18	11.84	6.85	4.31
399.9 – 503.1	7.54	6.48	10.75	6.07	6.87
503.1 – 599.85	7.99	8.14	11.70	7.08	5.03
599.85 – 703.05	6.54	6.17	9.90	3.09	6.99
703.05 – 799.8	6.66	5.46	10.57	1.78	8.85
799.8 – 903	8.74	8.46	12.61	6.16	7.74
903 – 999.75	8.17	5.91	14.12	6.61	6.05

999.75 – 1051.35	7.91	6.48	7.36	14.05	3.76
1051.35 – 1096.5	0.74	7.32	6.13	-8.30	-2.20
1096.5 – 1199.7	8.62	8.13	12.42	5.10	8.82
1199.7 – 1296.45	5.00	6.65	4.26	5.12	3.98
1296.45 – 1399.65	3.22	0.23	5.46	6.58	0.59
1399.65 – 1496.4	9.88	10.54	8.84	14.34	5.82
1496.4 – 1548	6.45	7.08	5.30	1.17	12.26
1548 – 1599.6	-11.96	-18.98	-11.56	-14.43	-2.88
1599.6 – 1651.2	17.84	12.48	15.82	25.20	17.85

DISCUSSION

The results of this project generally follow our initial hypothesis because the functional components of both LD and FD dosimeters were Al_2O_3:C crystals created by LANDAUER. The signal in the FD dosimeters likely was not as strong as the signal in the LD dosimeters because the concentration of the crystal was not as high and additional plastic from the 3D filament caused absorption of both the stimulating laser and the emitted light. Otherwise, the dosimeters were functionally the same.

Linearity of LANDAUER Dot and Filament Dot Dosimeters Exposed to 51.6 – 199.95 cGy

The first experiment exposed 4 LD and 4 FD dosimeters to 51.6, 103.2, 148.35, and 199.95 cGy. Each dosimeter was read 10 times, and the average of the 10 readings was calculated and plotted with respect to dose (Figure 8 and Figure 9). A linear fit was generated to determine if the counts for the LD and FD dosimeters also increased linearly with dose and an R^2 value of the linear fit was calculated. The R^2 value was calculated to determine how closely the linear fit matches the data. The closer the R^2 value is to 1.00, the more closely the fit is aligned with the data, meaning the counts linearly increase with dose.

The R^2 was 0.99 for both the LD and FD dosimeters and shows the counts/cGy increases linearly. The counts of the FD dosimeters were not as high as the LD despite being exposed to the same dose, likely because the concentration of the crystal was not as high, and the TPU caused absorption of both the stimulating laser and the emitted light. The results make sense because the functional components of both LD and FD dosimeters were both Al_2O_3:C crystals created by LANDAUER. The difference is how the crystals are held, but the crystal's physical properties are likely unaltered.

Fading Characteristics of LANDAUER Dot and Filament Dot Dosimeters Exposed to 51.6 – 199.95 cGy

Previous studies have shown there is little loss in signal (0.05% per reading) (Perks et al., 2008) for OSLDs exposed to a dose of 0.1 cGy or greater. One hundred measurements of the LD and FD dosimeters were taken and then plotted in Figure 10 and Figure 11 for the LDs and FDs, respectively. An exponential decay fit of the plots was generated with corresponding R^2 values for each fit. Figure 10 shows the R^2 values of the generated exponential decay for the LD dosimeters ranged from 0.64 to 0.83. Figure 11 shows the R^2 values of the generated exponential decay for the FD dosimeters ranged from 0.91 to 0.99. The R^2 values being closer to unity for the FD dosimeters than the LD dosimeters show that the FD dosimeters exhibit more precise and predictable fading over many measurements. It is unclear why the FD dosimeters exhibit more precise and predictable fading and further investigation is needed.

Signal Fading

The average signal loss per measurement as a percentage of the preceding measurement for the LD dosimeters was 0.11% and 0.25% for the FD dosimeters. The FD dosimeters, on average, had 127.27% more signal loss per reading than the LD dosimeters. The Al_2O_3:C crystals were the active component of both the LD and FD dosimeters, and the Al_2O_3:C crystals lost more signal as a percentage of the preceding measurement in the FD dosimeters than the LD dosimeters. The R^2 values for the exponential fits of the LDs are all lower than the FDs' R^2 fits (as summarized in Table 1 and Table 3), showing that the FDs all had more predictable signal fading than the LDs. Even though the FDs had a larger signal loss per measurement, the signal fading was more consistent and predictable, which is preferred for clinical and research applications because it allows users of the FDs to calculate the original dose to the dosimeter

more accurately with application correction factors. Inconsistent signal fading makes calculating and applying correction factors to determine the original dose far less accurate. It is unclear as to why the FDs exhibit more predictable signal fading than the LDs, as signal fading between the dosimeters would have been thought to be the same since the radiosensitive Al_2O_3:C is fundamentally the same in both dosimeters, but it is a favorable characteristic to have.

Uniformity of LANDAUER Dot and Filament Dot Dosimeters

To compare uniformity, sixteen printed FDs and sixteen LANDAUER LDs were selected, and each dot was exposed to a specific dose ranging from 303.15 – 1651.2 cGy and plotted (Figure 12 and Figure 13). A quadratic fit was generated in the plots, and it was evident that the LDs more closely followed the linear fit than the FD dosimeters. This was reflected in the R^2 values of 0.9873 and 0.7288 for the LDs and FDs, respectively. Looking at Figure 13, the FD dosimeter was rather imprecise as some FD dosimeters yielded lower counts despite being exposed to higher doses, and the number of counts increased in a seemingly random manner. The randomness of the data for the FD dosimeters is evident from the fact that the generated quadratic fit curves upward in a positive direction. This implies the fit suggests an increase in counts/cGy, contrary to all other findings in this study and previous studies. This inconsistency could be due to the Al_2O_3:C crystals not being uniformly distributed throughout the filament used to make the FD dosimeters.

The lack of uniformity in the FD dosimeters compared to the LD dosimeters is further highlighted by comparing the percent differences between the predicted counts (calculated with the generated quadratic fits) and the average of the measured counts, as summarized in Table 7. The percentage difference for the LD dosimeters ranged from 0.57 – 8.49%, while the percentage difference for the FD dosimeters ranged from 3.45 – 55.22%. This substantial

difference indicates that the FD dosimeters cannot be reliably used to measure doses consistently between each other. Further work is needed to address this lack of uniformity between FD dosimeters. This could be tested by repeating the experiment and modifying the creation and extrusion process of the filament used to make the FD dosimeter. Rather than cutting and re-extruding the filament 2 times, the filament could be cut and re-extruded many more times, e.g., 10 times, to determine if this process results in a more uniform dose response between the subsequent FD dosimeters. If there are still inconsistent dose responses between FD dosimeters, there may be other sources of error, such as the microStar.

Assessment of Data Fits for LANDAUER Dot and Filament Dot Dosimeters Exposed to Low Doses

Previous studies have found that a linear fit was appropriate for OSLDs exposed to doses up to 300 cGy, and a quadratic fit was more appropriate for doses beyond 300 cGy (Perks et al., 2008). However, our findings indicate that a quadratic fit is more appropriate for the LD and FD dosimeters even at doses lower than 300 cGy. This suggests that the supra-linear response observed by Jursinic (2007) may begin before 300 cGy. This is supported by the higher R^2 values of the quadratic fits compared to the R^2 values of the linear fits, which have been shown to be significant by the F statistic being greater than the critical value when $\alpha = 0.05$ for most of the dosimeters. The exception is the F statistic is lower than the critical value for FD 1 and 4, indicating that the linear fit is more appropriate than the quadratic for these two dosimeters.

The R^2 value for the plot of the average counts of the four LD dosimeters was 0.9917 for the linear fit (Figure 14) and 0.9996 for the quadratic fit (Figure 16). The R^2 values of the plots for each LD were 0.9904, 0.9925, 0.9906, and 0.9914 for the linear fit (Figure 15) and 0.9986, 0.9988, 0.9994, and 0.9998 for the quadratic fit (Figure 17). Similarly, the R^2 value for the plot

of the average counts of the four FD dosimeters was 0.9945 for the linear fit (Figure 18) and 0.9988 for the quadratic fit (Figure 20). The R^2 values of the plots for each FD were 0.9853, 0.9912, 0.9786, and 0.986 for the linear fit (Figure 19) and 0.9858, 0.9982, 0.9893, and 0.9888 for the quadratic fit (Figure 21). The R^2 value of the quadratic fit is higher for every quadratic fit compared to the R^2 value of the linear fit, and the calculated F statistic is higher than the critical value, which shows that even at low doses, a quadratic fit more closely aligns with the data. Additionally, visual inspection of the plots shows the data points tend to round off with increasing dose rather than increase linearly, further indicating that the quadratic fit aligns more closely.

The notable exception is the linear fit is more appropriate for FD 1 and 4 as the calculated F statistic is smaller than the critical value showing the higher R^2 value of the quadratic fit is not significant.

As mentioned above, a quadratic fit is more appropriate than a linear fit for all the individual LDs and the average of the individual LDs, half of the FDs, and the average of the individual FDs, which is contrary to previous studies' findings. A potential explanation for this may be the difference in methodology. Previous studies did not incrementally increase the dose of the dosimeters and did not account for the potential fading effects caused by repeated readings. This fading may have affected our findings, leading to the observed preference for a quadratic fit at low doses. However, the quadratic fit for FD 1 and 4 was not more significant than the linear fit and it is unclear as to what caused the difference in behavior between the FDs at low doses. More FDs should be made and exposed to low doses to determine if this difference in behavior is observed across many FDs when exposed to low doses. Since the quadratic fit followed the measured data more closely than the linear fit for the average counts of LDs and

FDs, even at low doses, a quadratic fit will be used to fit the data of the LDs and FDs in this study.

Dose Range of LANDAUER Dot and Filament Dot Dosimeters

To address the uniformity issues previously encountered and determine the dose at which saturation occurs for the LD and FD dosimeters, 4 LDs and 4 FDs were selected and incrementally exposed to doses. The 4 dosimeters were irradiated simultaneously and then read. The counts were averaged to obtain counts/cGy. The average counts/cGy of all 4 LDs and FDs were plotted (Figure 22 and Figure 24) as well as the average counts/cGy of the individual LDs and FDs (Figure 23 and Figure 25).

If saturation of the dosimeters has occurred, the increase in counts/cGy when reading the dosimeters should substantially decrease. For the LD dosimeters, saturation initially appeared to have occurred at the 999.75 – 1051.35 cGy dose interval, where the slope between doses for the averages of LD 1-4 was 426.71 counts/cGy. For comparison, the slope between doses of 903 – 999.75 cGy was 1544.69 counts/cGy, showing a large drop in counts/cGy for the 999 – 1051.35 cGy dose interval. Further, the slope between doses of individual dosimeters is 180.105 and -295.895 counts/cGy for LD 3 and 4, respectively. The slope between doses at the same dose interval for LD 1 and 2 was 855.442 and 967.182 counts/cGy. However, the slope between doses of the next total dose interval, 1051.35 – 1096.5 cGy, for the averages of the 4 LDs was 2039.76 counts/cGy, the highest slope between doses. The slope between doses for the averages of the 4 LDs goes from a minimum of 426.708 counts/cGy to a high of 2039.76 counts/cGy in the next total dose interval. This indicates there is a high degree of variability in the dose response between dosimeters. This is evidenced by the fact that within the same dose range, 1051.35 – 1096.5 cGy, LD 1 had a slope of 823.02 counts/cGy whereas LD 4 had a slope of 3,314.03

counts/cGy. LD 4's slope is over 4 times as great as LD 1. Additionally, in the dose range of 999.75 – 1051.35 cGy, LD1 had a slope of 855.44 counts/cGy, while LD 4 had a slope of -295.9 counts/cGy. This indicates there is an unknown cause of variability between the dosimeters rather than saturation. If saturation had occurred, the slope between doses would not have increased to a new maximum in the next total dose interval, and the slope between doses of all 4 dosimeters would have been low.

The lowest slope between doses for the averages of LD 1-4 was 361.21counts/cGy, which occurs in the 1548 – 1599.6 cGy total dose interval, but the slope between doses of the next dose interval, 1599.6 – 1651.2 cGy, was 711.574 counts/cGy. If saturation were occurring, the counts/cGy should continue to decrease after the 1548 – 1599.6 cGy dose interval but increased instead. It is unclear at this time why this is occurring as the manufacturer had said saturation occurs at 1500 cGy, but these results indicate that saturation may occur at a dose higher than 1500 cGy.

For the averages of FD 1-4, the first time the slope between doses drops significantly is during the total dose interval 1051.35 – 1096.5 cGy, where the slope between doses was 0.74 counts/cGy. However, saturation has probably not occurred. Similarly to the LD dosimeters, the slope between doses of the FD dosimeters in the next total dose interval, 1096.5 – 1199.7 cGy, recovered to 8.62 counts/cGy. Further, when analyzing the slope between doses of individual dosimeters for the dose interval of 1051.35 – 1096.5 cGy, the slope of FD 1 and 2 was 7.32 and 6.13 counts/cGy, while the slope for FD 3 and 4 was -8.30 and -2.20 counts/cGy. This disparity indicates variability between dosimeters rather than saturation across all 4.

The lowest slope between doses for the averages of FD 1-4 occurs in the 1548 – 1599.6 cGy for the dose interval where the slope is -11.96 counts/cGy. The slope between doses for all 4

dosimeters was -18.98, -11.56, -14.43, and -2.85 counts/cGy for FD 1, 2, 3, and 4, respectively. The negative slope would indicate that the FD dosimeters reach saturation in the 1548 – 1599.6 cGy total dose interval, but the slope between doses of the next dose interval, 1599.6 – 1651.2 cGy, was 17.84 counts/cGy. This behavior of increasing slope after a minimum slope, similar to that of the LDs, appears to contradict the manufacturer's claim of saturation occurring at 1500 cGy, and the reason for this is unclear.

Advantages of FD Dosimeter

Models made with the same filament used to make the FD dosimeter would be highly customizable and able to be modified for a wide range of circumstances and be able to create unique and complex shapes. The printed models can be tissue equivalent, meaning they absorb and distribute dose similarly to patient tissue, as x-ray scatter behaves differently in non-tissue equivalent models. A bolus can be made from FD filament to directly measure dose, allowing the beam field to be directly measured in areas where planning software may miscalculate dose due to air gaps.

While measuring signal fading over many measurements, the FD dosimeter followed the generated exponential fit more closely than the LD dosimeter. This is demonstrated by the R^2 values of the generated exponential fit for the 4 FD dosimeters being 0.914, 0.9592, 0.9798, and 0.9905 (Figure 11), compared to 0.6412, 0.8071, 0.8348, and 0.8036 for the 4 LD dosimeters (Figure 10), with the FD dosimeters having values closer to 1, indicating a higher goodness of fit. This is an unexpected result, given that the FD dosimeters have fewer total counts during measurement, making them more susceptible to variance. Typically, this would result in a larger negative impact on the goodness of fit compared to measurements with a higher number of counts. The higher goodness of fit of the FD dosimeters suggests that the FD dosimeter may be

more adept at calculating the original dose after numerous readings and demonstrates higher stability.

Previous studies of Al_2O_3:C have shown that the crystals are stable over time and do not undergo annealing when kept in a dark environment, so the crystals in the filament should be stable as well. Models and OSLDs made from the filament with Al_2O_3:C crystals incorporated would be able to be read a long time after exposure and still provide accurate readings if they are stored in a dark environment. Testing crystals' stability in the filament over time is required to determine if the crystals in the filament remain stable and must be studied in future research.

The NinjaFlex TPU was tissue equivalent, and the relative amount of Al_2O_3:C crystals incorporated into the filament was low enough that the atomic value of the filament remained tissue equivalent so any objects made from the filament would also be tissue equivalent. If the concentration of the crystals were increased in the printed filament, the sensitivity would increase but the filament or printed objects would no longer be tissue equivalent. Ideally, the concentration would be increased but not enough to substantially increase the effective atomic number of the filament. It could also be possible to increase the concentration of Al_2O_3:C such that the effective atomic number may be increased enough to match other materials like bone and be used to create bone-equivalent phantoms.

Disadvantages of FD Dosimeters

The number of counts recorded by the microSTAR when reading the filament is many orders of magnitude lower than the number of counts recorded when reading the commercially available dots. In this study, we used a low concentration of OSLD crystal. This resulted in a comparatively lower sensitivity to dose. Future work should explore higher concentrations of

active crystal. However, as mentioned earlier, maintaining the same effective atomic number as water may be challenging.

Future Work

Currently, access to Al_2O_3:C crystal is limited and somewhat expensive due to LANDAUER recalling all nanoDots (Vishwanathan, 2023). We do not know of any other producers of radiosensitive Al_2O_3:C crystal. Alternate cost-effective forms are required to fully see this dosimetric alternative come to fruition.

The ability to fully utilize the 3D dosimetry aspect currently requires the printed model to be cut and prepared into the required size for the OSLD for the reader. After exposure, the OSLD still needed to be physically modified to fit the dimensions of the holder so the OSLD could be read by the microSTAR. This was found to be relatively time and labor-intensive, and it was possible for the dosimeter to fall from the loader and be lost inside the reader.

The likely lack of uniformity was a major drawback in the FDs. Figure 13 shows some FDs having higher counts despite being exposed to less dose and this prohibits the FDs from being used as reliable dosimeters. Until this inconsistent counts/cGy response between multiple FDs is addressed the FDs cannot be used as dosimeters. The inconsistent counts/cGy between individual FDs are likely due to the inhomogeneous distribution of Al_2O_3:C crystals within the filament. The current degree of inhomogeneity may introduce variability that is beyond a clinically useful level and shows the method used to create the OSLD filament and FDs requires further refinement.

Another important next step in this work is developing a way to produce more cost-effective radiosensitive Al_2O_3:C crystals which would be incorporated into the filament during extrusion. This would allow for experimentation to determine the ideal concentration of Al_2O_3:C

in the filament that would allow for successful printing and ideal sensitivity for dosimetry applications. Using dismantled LANDAUER nanoDot dosimeters as the source for Al_2O_3:C crystals appeared to add additional jamming in the printer nozzle. We believe this may be due to the plastic adhered to the Al_2O_3:C crystals which would jam in the printer nozzle. Regardless, a new way to obtain or produce radiosensitive crystals is needed. Once radiosensitive crystals are produced, more work is needed to determine the most effective way to extrude filament, more optimized ratios of Al_2O_3:C crystals to TPU, and further characterizations of the filament.

CHAPTER 2

ALTERNATIVE METHODS OF CREATING Al_2O_3:C

INTRODUCTION

The earlier experiments and methods developed in the previous chapter used commercially available Al_2O_3:C manufactured by LANDAUER, and while the crystal is effective for radiation measurements, it quickly becomes prohibitively expensive to purchase it for experiments. Additionally, on August 17, 2023, LANDAUER issued a voluntary recall of all nanoDots due to reports of some nanoDots' accuracy being outside of the specified range (Vishwanathan, 2023). However, the LANDAUER microStar reader used in the previous chapter is designed to measure Al_2O_3:C and would unlikely be unable to be used with other radiosensitive crystals. Therefore, to continue the development of radiosensitive filament for 3D printing, a novel method of creating Al_2O_3:C would need to be developed. In the original studies conducted by Akselrod, the radiosensitive $Al_2O_3:C$ was created by incorporating carbon into Al_2O_3 using the Verneuil method (Akselrod et al., 1993). In this method, the Al_2O_3 is brought to

a high enough temperature to melt Al_2O_3. The Al_2O_3 is cooled to create the Al_2O_3:C crystal. The Al_2O_3:C crystal has a carbon impurity of 100-5000 ppm. The solid crystal is then ground down to a powder and sieved so crystals of the ideal size, 100-125 μm, can be selected and made into the OSLD (Akselrod et al., 1993). The key aspect of the Verneuil method is that a known concentration of carbon, 100-5000 ppm, is incorporated into the Al_2O_3 crystal lattice by melting of Al_2O_3, but a furnace with the ability to generate the required heat of 2050 ℃ to melt the Al_2O_3 was unavailable. To create radiosensitive Al_2O_3:C capable of being read by the LANDAUER microStar reader, new methods of incorporating carbon into Al_2O_3 without a furnace capable of reaching 2050 ℃ would need to be developed.

Arc Furnace

While a more traditional furnace capable of reaching 2050 ℃ was not available another device which could heat of Al_2O_3 to its melting point was - an arc furnace. An arc furnace heats a material by exposing the material to an electric arc. The electric arc is generated by building an extremely high voltage in an electrode using a generator and then discharging the voltage through the material, which is held in a copper crucible, and the current through the material generates heat. Arcs can be continuously applied to the material to increase its temperature. While it is difficult to precisely control the temperature the material is heated to in the arc furnace, and the arc causes rapid heating and cooling, it is still possible to reach temperatures higher than most laboratory furnaces can reach and makes it possible to heat the Al_2O_3 to its melting point in the presence of carbon. By melting Al_2O_3 in the presence of carbon, we theorized that some carbon atoms will be incorporated into the Al_2O_3 structure and make radiosensitive Al_2O_3:C.

Hot Acid Synthesis

In a study conducted by Michaella Swinhart, Asher DeLarme, and Anthony L. Diaz, the authors designed an experiment to more systematically and comprehensively study YBO_3: RE, Ca^{2+}(RE = Eu^{3+} or Tb^{3+}). To synthesize the $Y_{1-x-y}BO_3$: RE_x, Ca_y, various amounts of Y_2O_3, H_3BO_3, $CaCO_3$, and rare earth oxide Eu_2O_3 were dissolved in 2 M hot nitric acid with stirring. The materials were dissolved entirely, and the resulting sample was evaporated to dryness. The remaining powder was ground and fired open to air in alumina crucibles for 2 hours at 240℃ and then covered and fired in air for 18 hours at 1100 ℃. After analysis it was found Ca^{2+} was incorporated into the lattice creating YBO_3:Eu,Ca (Swinhart et al., 2022).

The methodology from the study was of particular interest as the authors were able to dope a structure with Ca^{2+} and form oxygen vacancies, and the OSLD of this study is Al_2O_3 doped with carbon. It was theorized that the hot acid synthesis methodology could be adapted to dope Al_2O_3 with carbon. By doping Al_2O_3 with carbon it is theorized that some carbon atoms will be incorporated into the Al_2O_3 structure and make radiosensitive Al_2O_3:C.

Low Energy X-Ray Exposure

During routine operation of the Small Animal Irradiator an x-ray filter is placed between the window and the collimator. The x-ray filter is a thin metal sheet that attenuates low-energy x-rays from the beam. If the low-energy x-rays were not filtered out, they would be absorbed by superficial structures, not the target area. Instead, the low energy x-rays would increase scatter and surface dose (Brosi et al., 2011).

It is known that Al_2O_3:C is acutely sensitive to low-energy x-rays (Lee & Jai Lee, 2001). This acute sensitivity to low-energy x-rays can be utilized to determine whether carbon had been incorporated into the Al_2O_3 lattice structure to create Al_2O_3:C using the AF or HA methods. If

carbon has been incorporated into the crystal lattice of the AF or HA powders the number of counts would likely increase at a rate greater than the increase in dose, reflecting the Al_2O_3:C's acute sensitivity to low energy x-rays and support that carbon had successfully been incorporated into the Al_2O_3 lattice structure.

Removing the 0.3 mm Cu treatment x-ray filter allows for low energy x-rays to not be filtered; the resulting dose to iso center increases as the x-ray intensity increases. Therefore, any powders exposed to the unfiltered beam will be exposed to an increased dose but if the luminescent signal strength increases at a rate greater than the increase in dose it is likely that carbon was incorporated into the Al_2O_3 and create Al_2O_3:C.

METHODOLOGY

Arc Furnace Methodology

The arc furnace is an Arc Melt Furnace ABJ-338 (Materials Research Furnace Inc., Allenstown, New Hampshire, USA) and was used to melt Al_2O_3 powder with carbon powder to incorporate the carbon into the of Al_2O_3 crystal structure and create radiosensitive Al_2O_3: C. In a large mortar and pestle 2.0015 g of Al_2O_3 powder, with a crystal size of ~90-100 μm (~150 mesh), and 0.0005 g of carbon powder were mixed for 10 minutes. After mixing, the powder was pressed into a 1/2-inch diameter pellet using a Bench Top Laboratory Pellet Press Model 4350 L (Carver Inc., Wabash, Indiana, USA) to ensure mixing and allow the powder to be heated more uniformly while in the arc furnace. The pellet was then heated with multiple arcs from the arc furnace and surpassed the melting point of alumina as the pellet changed from a solid to a molten liquid. The furnace was turned off, the molten liquid was left to cool, and a solid black pellet remained after cooling. The black pellet was then ground down to a powder using a mortar and pestle.

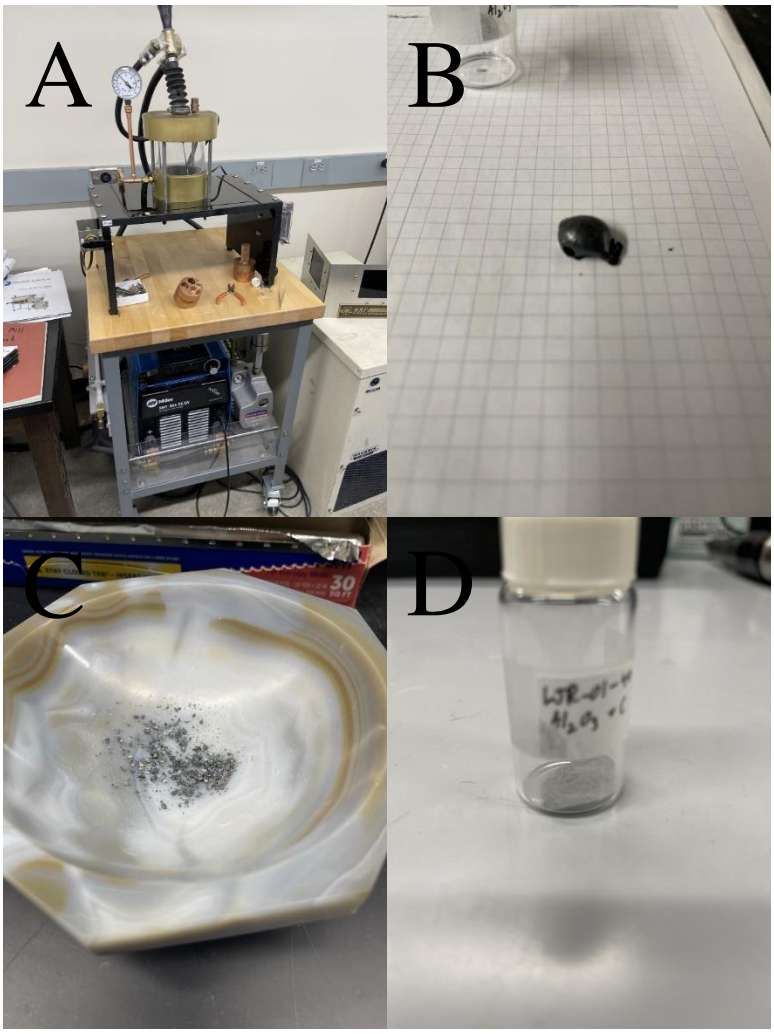

Figure 26: A) Photo of the arc furnace. B) The black pellet remaining from the cooled molten carbon and Al_2O_3. C) The black pellet is ground to a powder using a mortar and pestle. D) Final form of the powderized Al_2O_3 and carbon.

Hot Acid Synthesis Methodology

To test if it was possible to incorporate carbon into $Al_2O_3:C$ using the Hot Acid Synthesis methodology and create radiosensitive $Al_2O_3:C$, the original methodology was adopted and applied. For the first test, 5.00350 g of Al_2O_3 powder with a crystal size of ~90-100 µm (~150 mesh) and 22.50 mg of carbon powder were added to 8 M nitric acid. The reason for those quantities of carbon powder and Al_2O_3 was that the ratio of carbon to Al_2O_3 is just under 5000 ppm, within the ratio of carbon to Al_2O_3 (Akselrod et al., 1993). The solution was stirred with a stir bar, and heat was added with a hot plate until all the liquid was boiled off. The remaining

crystal was scraped off the beaker, and black carbon was visible. Once all the liquid had been boiled off, the powder was scraped from the beaker and put in an alumina crucible to be fired in the muffle furnace for 2 hours at 350 ℃. Once the crucible had cooled, a powder sample was removed and crushed into an even finer powder. The powder was fired in the muffle furnace again for 2 hours at 350 ℃. Once the crucible had cooled, the remaining powder was removed from the crucible and crushed to a fine white powder.

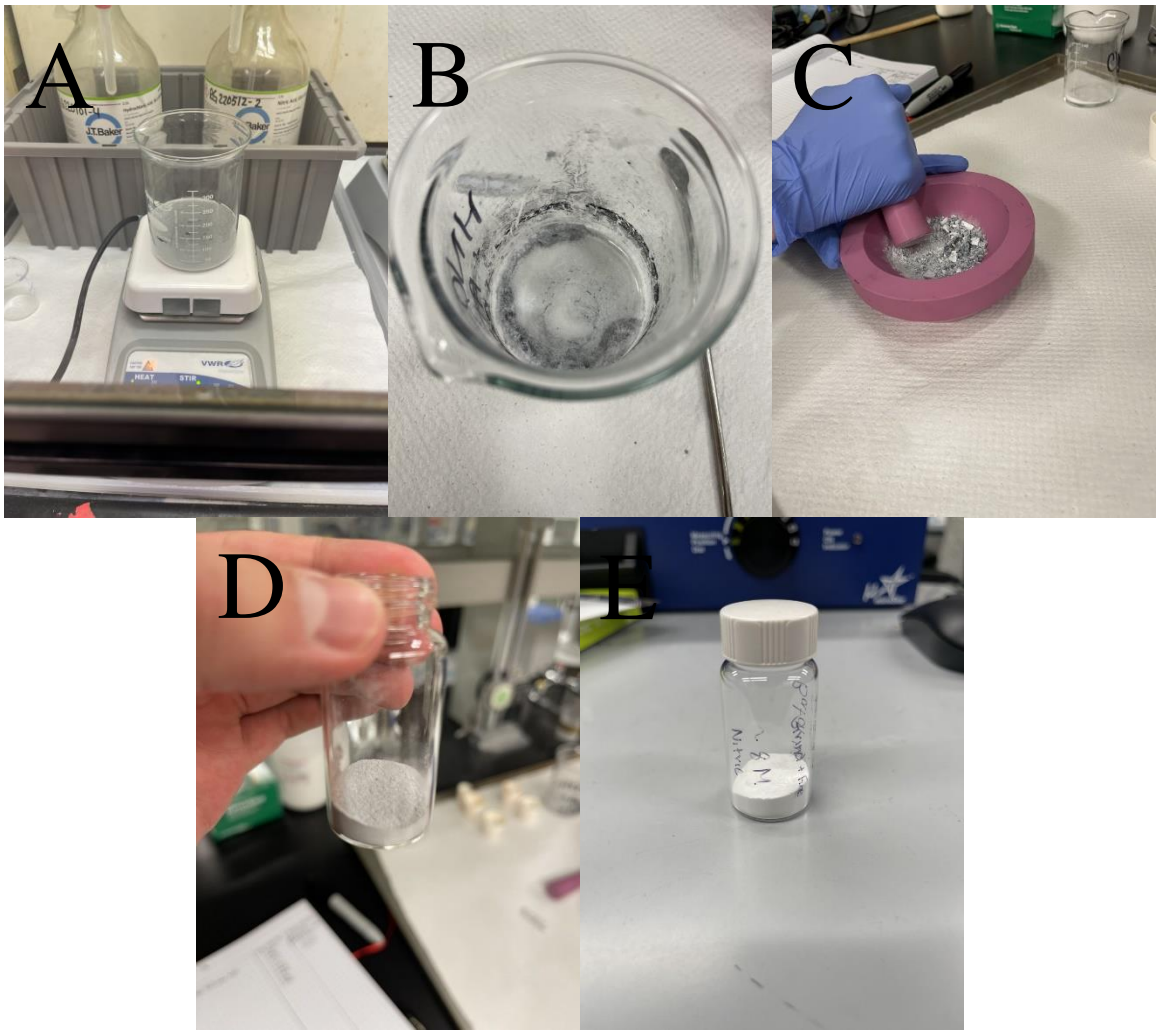

Figure 27: A) Al_2O_3 and carbon in 8 M nitric acid are stirred while the nitric acid is boiled off using a hot plate. B) Beaker with Al_2O_3 and carbon on the bottom and sides after 8 M nitric acid and water had been boiled off. C) Powder with Al_2O_3 and carbon being ground to a powder after being removed from the beaker. D) Powder after being fired in an alumina crucible in a muffle furnace for 2 hours at 350 ℃*. E) Powder after being fired for an additional 2 hours at 350* ℃ *in the muffle furnace.*

Radiation Sensitivity Testing of All Three Powders Using X-Ray Beam

The 3 powders: the original unaltered Al_2O_3 powder, the Al_2O_3 powder and carbon powder from the arc furnace (AF), and the Al_2O_3 and hot acid (HA) powder, were then prepped to be measured. The powders were spread thinly over the adhesive side of the Scotch Self-Seal Laminating Pouch (3M, St. Paul, Minnesota, USA), and a hole punch was used to punch 24, 7 mm diameter dots with a thin coating of powder, 8 dots of each powder. The dots were then weighed. Three dots with no powder were punched from the Scotch Self-Seal Laminating pouch and weighed to determine the weight of a dot without any crystal adhered. The dots with the powder adhered had the mass of the dots without powder subtracted to determine the mass of the adhered powder. The powdered dots were initially measured by the microSTAR 10 times to collect pre-irradiated measurements, which were averaged.

The Precision Small Animal Radiation Therapy irradiator was used to deliver radiation to the dots, which were placed on SuperFlab (to provide backscatter) at isocenter with a 40 mm × 40 mm square collimator, set to 225 kVp, with a current of 13 mA, and a 0.3 mm Cu filter. The delivered dose is controlled by units of time where, under the stated conditions, the delivered dose was 1940 cGy when the beam was turned on for 5 minutes. This high dose was chosen to maximize the likelihood of detecting any potential response from the dots.

After exposure, all the dots were measured 10 times, and the average counts of those measurements were calculated. The average counts for each dot pre- and post-irradiation were divided by the mass of the powder to calculate the number of counts/grams of powder. The average counts/gram pre-irradiation were subtracted from the average counts/gram post-irradiation to find the difference in counts/gram. The larger the difference in counts/gram the powder is, the more radiosensitive the crystal is.

All the samples were measured the same way the FDs were in the previous chapter. A LANDAUER microSTAR reader was used to read the recorded dose on the samples. The samples are placed in a LANDAUER InLight holder. The InLight holder is a light-tight plastic rectangle with a plastic slide with four 7 mm diameter holes. The slide can move in and out of the light-tight rectangle. When the InLight holder is loaded into the microSTAR, the plastic slide extends out and positions 1 of the 4 samples between the stimulating laser and the PMT tube. The holes in the slide allow light from the stimulating laser to hit the dosimeters allowing the luminescence light to travel out the other side to the PMT. The samples were kept in position by lightly coating the edges of the slide's holes with Elmers Liquid School Glue (Elmer's Products, Inc., Westerville, OH, USA). The glue unlikely affected any measurements by blocking light from the stimulating laser or the luminescing sample because the slide places the sample behind a 5 mm diameter aperture. The glue was put on the edge of the 7 mm hole so no glue would ever be in the path of the stimulating laser or luminescence light. The glue prevented any samples from falling off the slide during measurement.

Radiation Sensitivity Testing of Unmodified Al_2O_3, AF, and HA Powders Exposed to Unfiltered X-Ray Beam

A key characteristic of dosimetry performed with Al_2O_3:C is that the relative response to 30 keV photons is 2.9 times higher than 1.33 MeV photons, meaning Al_2O_3:C may over-respond to lower energy photons (Lee & Jai Lee, 2001). To potentially enhance any possible signal, the 0.3 mm copper treatment filter was removed to expose the powders to low-energy x-rays that the filter would normally remove. This was done. Four AF, HA, and unmodified powder dots were then irradiated to expose the powders to low-energy x-rays.

After exposure, all the dots were measured 10 times, and the average counts of those measurements were calculated. The average counts for each dot pre- and post-irradiation were divided by the mass of the powder to calculate the number of counts/grams of powder. The average counts/gram pre-irradiation were subtracted from the average counts/gram post-irradiation to find the net difference in counts/gram.

With the Cu filter removed the dose to the samples was increased. The increase in dose is examined and calculated in Appendix A. With the increase in dose and the previously observed extra sensitivity to low-energy x-rays, the counts, or sensitivity factor, was expected to increase. The expected sensitivity factor increase was calculated by multiplying the increase in dose factor by the sensitivity to low energy x-rays factor.

$$\text{Sensitivity Factor Increase} = \text{Increase in Dose Factor} \times \text{Sensitivity to Low Energy X} - \text{Rays}$$

$$= 3.76 \times 2.9$$

$$= 10.90$$

The measured sensitivity factor increase was calculated by dividing the average counts/gram of the samples exposed to the unfiltered beam for all 4 samples by the average counts/gram of the samples exposed to 1940 cGy.

$$\text{Sensitivity Factor Increase of Powder} = \frac{\text{Average Net } \frac{\text{Counts}}{\text{Gram}} \text{ Exposed to Unfiltered Beam}}{\text{Average Net } \frac{\text{Counts}}{\text{Gram}} \text{Exposed to Filtered Beam}}$$

Standard Deviation of Single Measurements

The standard deviation of single measurements was calculated in the same manner as the standard deviation of single measurements in Chapter 1 because the microSTAR was used to measure the samples the same way it was used to read the LD and FD dosimeters, so the

measurement statistics remain the same. All measurements were made with the microSTAR, which measured luminescing light, and when measuring light with a PMT, the number of detected photons is determined by Poisson distribution (de Haas & Dorenbos, 2011). Further, the number of counts was the only measurement of the luminescing light for a single measurement. Hence the average number of counts for the single measurement is equal to the counts for that measurement. When using the Poisson distribution, the standard deviation is the square root of the average number of counts (Knoll, 2010).

$$\text{Standard Deviation} = \sqrt{\text{Counts}}$$

All plots showing the number of counts for a single measurement include error bars representing the standard deviation, which is equal to the square root of the number of counts.

Statistical Analysis

Standard Deviation of a Single Measurement

When analyzing the data of a single measurement, it is necessary to calculate the standard deviation, σ, as it is a useful index of the degree of scatter within the data. To calculate the standard deviation some assumptions must be made. All measurements were made with the microSTAR, which measured luminescing light, and when measuring light with a PMT, the number of detected photons is determined by Poisson distribution (de Haas & Dorenbos, 2011). Further, the number of counts was the only measurement of the luminescing light for a single measurement so we must assume that the mean of the measurement distribution is equal to the single measurement, or $\bar{x} = x$. We can conclude that when the model is Poissonian $\sigma = \sqrt{\bar{x}}$, and $\bar{x} = x$ because x is our only measurement which $\bar{x}$ can be based. Therefore, the standard deviation being equal to x is the best estimate of deviation for a single measurement, $\sigma = \sqrt{x}$ (Knoll, 2010).

$$\text{Standard Deviation} = \sqrt{\text{Counts}}$$

All plots showing the number of counts for a single measurement include error bars representing the standard deviation, which is equal to the square root of the number of counts.

Standard Deviation of Averages

When calculating the averages we have a total number of counts measured by the microSTAR after reading the dosimeters N number of times. The counts from each measurement are designated as x_1, x_2, …, x_N, and the sum of the counts from all measurements is equal to Σ.

$$\Sigma = x_1 + x_2 + \ldots + x_N$$

When the error of the independent measurements, σ_{xN}, is applied to the sum the expected error of the sum, σ_Σ, is

$$\sigma_\Sigma^2 = \sigma_{x1}^2 + \sigma_{x2}^2 + \cdots + \sigma_{xN}^2$$

And since $\sigma_{xN} = \sqrt{x_N}$ for each count σ_Σ^2 is

$$\sigma_\Sigma^2 = x_1 + x_2 + \ldots + x_N$$

So

$$\sigma_\Sigma = \sqrt{\Sigma}$$

This shows the standard deviation for the sum of all counts is as if the sum had been measured from a single measurement.

The mean value of all the measurements is simply the sum divided by the number of measurements.

$$\bar{x} = \frac{\Sigma}{N}$$

This is an error-associated quantity divided by a constant, so the expected standard error of the mean is

$$\sigma_{\bar{x}} = \frac{\sigma_\Sigma}{N} = \frac{\sqrt{\Sigma}}{N} = \frac{\sqrt{N\bar{x}}}{N}$$

$$\sigma_{\bar{x}} = \sqrt{\frac{\bar{x}}{N}}$$

(Knoll, 2010).

Shapiro-Wilk Test to Determine if Data is Normally Distributed

To determine if the results of the samples are significantly different from each other, multiple statistical tests are performed. The first test is the Shapiro-Wilk test which performed on the net counts/gram (average counts/gram post-irradiation – average background counts/gram,) for all 4 samples of each of the 3 powders to test the null hypothesis that the data comes from a normal distribution. If the null hypothesis is true, then it can be determined that the data is normally distributed. Whether or not the data is normally distributed determines if tests require an assumption of normality in the data.

A W statistic is calculated with the following formula:

$$W = \frac{(\sum_{i=1}^{n} a_i x_{(i)})^2}{\sum_{i=1}^{n}(x_i - \bar{x})^2}$$

X_i is the sorted value of the net counts/gram (the data is sorted from smallest to largest), $\bar{x}$ is the mean net counts/gram, and a_i is a coefficient based on the expected values of order statistics from a normal distribution found in the Shapiro-Wilk test table. All data sets in which the W statistic is calculated have 4 measurements so that the a_i coefficients will be 0.6872, 0.1677, -0.1677, and -0.6872.

The p-value of the test is calculated using the W statistic and the Shapiro-Wilk test table of p-values. We used a significance (α) level of 0.05, and by using the Shapiro-Wilk test table, the $W_{0.05}$ value for a data set of 4 measurements is 0.75. Any *W* value greater than 0.75 means the p-value is greater than α = 0.05, and the null hypothesis is not rejected. When the null hypothesis is not rejected, we conclude that the dataset is normally distributed (SHAPIRO & WILK, 1965).

F-Test Two-Sample for Variances

If we have concluded from the Shapiro-Wilk test that the net counts/gram of the samples were normally distributed, the next statistical test performed was the F-Test between the AF or HA samples and the unmodified Al_2O_3 samples. The F-test tests the null hypothesis that the variance of two data sets is equal. The first step is to calculate the sample variances of the two different data sets, s_1^2 and s_2^2, where s_1^2 is the variance of the first data set and s_2^2 is the variance of the second data set. The sample variance is calculated with the following formula:

$$s^2 = \frac{1}{n-1}\left(\sum_{i=1}^{n} x_i^2 - \frac{\left(\sum_{i=1}^{n} x_i\right)^2}{n}\right)$$

Where n is the number of data points, and x_i is the value of the individual data point (Welford, 1962).

The F statistic, F, is then calculated using the sample variances. The F statistic is calculated as follows:

$$F = \frac{s_1^2}{s_2^2}$$

The degrees of freedom are determined. The degrees of freedom for the numerator are $n_1 - 1$ for the numerator and $n_2 - 1$ for the denominator, where n_1 and n_2 are the number of measurements for each respective data set. For this experiment, the degrees of freedom will always be 3 because there are 4 measurements in each data set. The degrees of freedom are used to determine the critical value with a significance (α) level of 0.05 from the $\alpha = 0.05$ F table. The critical value when $\alpha = 0.05$, and 3 degrees of freedom in the numerator and denominator is 9.28. If the F statistic is greater than the critical value, then the null hypothesis is rejected, and it is concluded that the variances of the two data sets are unequal (*13.5: Test of Two Variances*, 2015). In the results, we calculated the F statistic using the F-Test Two-Sample for Variances

data analysis tool in Microsoft Excel. The first data set will be the AF or HA average minus background post-irradiation counts, and the second will be the unmodified average - background post-irradiation counts.

t-Test: Two-Sample Assuming Unequal Variances

If it has been concluded using the F-Test Two-Sample for Variances that the variances of AF, HA, and unmodified Al_2O_3 samples net counts/gram are unequal, then the T-Test: Two-Sample Assuming Unequal Variances is performed to determine if the null hypothesis can be rejected, and it can be concluded that the mean net counts/gram of the AF or HA is significantly higher than the unmodified Al_2O_3 powder. The first step is to calculate the t statistic. The t statistic is calculated as follows:

$$t = \frac{\overline{x_1} - \overline{x_2}}{\sqrt{\frac{s_1^2}{n_1} + \frac{s_2^2}{n_2}}}$$

where $\overline{x_1}$ is the mean of either the AF or HA net counts/gram and $\overline{x_2}$ is the mean of the unmodified Al_2O_3 net counts/gram, s_1^2 and s_2^2 are the respective variances and n_1 and n_2 are the number of dot sizes.

The degrees of freedom are calculated using the following equation:

$$df = \frac{(\frac{s_1^2}{n_1} + \frac{s_2^2}{n_2})^2}{\frac{(\frac{s_1^2}{n_1})^2}{n_1 - 1} + \frac{(\frac{s_2^2}{n_2})^2}{n_2 - 1}}$$

The degrees of freedom determine the critical value with a significance (α) level of 0.05 from the t-Distribution table when $\alpha = 0.05$. For this analysis the degrees of freedom are always 3 and the critical value when $\alpha = 0.05$ and a one-tail analysis is used, is 2.35. If the t statistic is greater than 2.35 or less than -2.35, then the null hypothesis is rejected, and it is concluded that

the observed differences between the means are significant (Ruxton, 2006). We calculated the t statistic using the t-Test: Two-Sample Assuming Unequal Variances data analysis tool in Microsoft Excel.

Mann-Whitney U Test

If we have concluded from the Shapiro-Wilk test that the set of the mean net counts/gram of any of the samples was not normally distributed, then the next statistical test performed was the Mann-Whitney U Test, sometimes referred to as the Wilcoxon Rank Sum Test, between the AF or HA dots and the unmodified Al_2O_3 dots. The Mann-Whitney U Test is performed to determine if the null hypothesis can be rejected, and the mean net counts/gram of the AF or HA is significantly higher than the unmodified Al_2O_3 powder.

To perform the Mann-Whitney U Test, the mean net counts/gram for each AF or HA sample, and the mean net counts/gram for each unmodified Al_2O_3 sample are combined into a single set. The mean net counts/gram are ranked from lowest to highest, e.g., the lowest mean net counts/gram is ranked 1, the second lowest mean net counts/gram is ranked 2, etc. Then, the ranks of the mean net counts/gram of the AF or HA and the unmodified Al_2O_3 are added to calculate the rank sum, R_{AF} or $R_{HA,}$ and $R_{unmodified}$. Next, the sample sizes, n, are determined but will always be 4 AF or HA dots compared to 4 unmodified Al_2O_3 dots, $n_{AF} = n_{HA} = n_{unmodified} = 4$. Test statistics are calculated using the following equations:

$$U_{\text{AF or HA}} = n_{\text{AF or HA}} n_{\text{unmodified}} + \frac{n_{\text{AF or HA}}(n_{\text{AF or HA}} + 1)}{2} - R_{\text{AF or HA}}$$

$$U_{\text{unmodified}} = n_{\text{AF or HA}} n_{\text{unmodified}} + \frac{n_{\text{unmodified}}(n_{\text{unmodified}}+1)}{2} - R_{\text{unmodified}}$$

The test statistic, U, is the smaller of the $U_{\text{AF or HA}}$ or $U_{\text{unmodified}}$. A critical value with a significance (α) level of 0.05 is found using a Mann-Whitney U Table when $\alpha = 0.05$ for a two tailed test. The column number is equal to $n_{\text{AF or HA}}$ and the row number is equal to $n_{\text{unmodified}}$.

Since $n_{AF} = n_{HA} = n_{unmodified} = 4$, the critical value is 0. If the test statistic U is equal to or smaller than 0, then the null hypothesis can be rejected, and we can conclude that the set of the mean net counts/gram of the AF or HA samples is significantly higher than the mean net counts/gram of the unmodified Al_2O_3 dots (Mann & Whitney, 1947).

RESULTS

Radiation Sensitivity Testing of Unmodified Al_2O_3, AF, and HA Powders Using X-Ray Beam

Four samples of unmodified Al_2O_3, AF, and HA powders were exposed to 1940 cGy, read 10 times, and averaged. The average counts were divided by the powder's mass to normalize the readings to counts/gram. The average counts/gram pre-irradiation were subtracted from the counts/gram post-irradiation to determine the average net difference in counts/gram and then plotted (Figure 28). The results are summarized in Table 16.

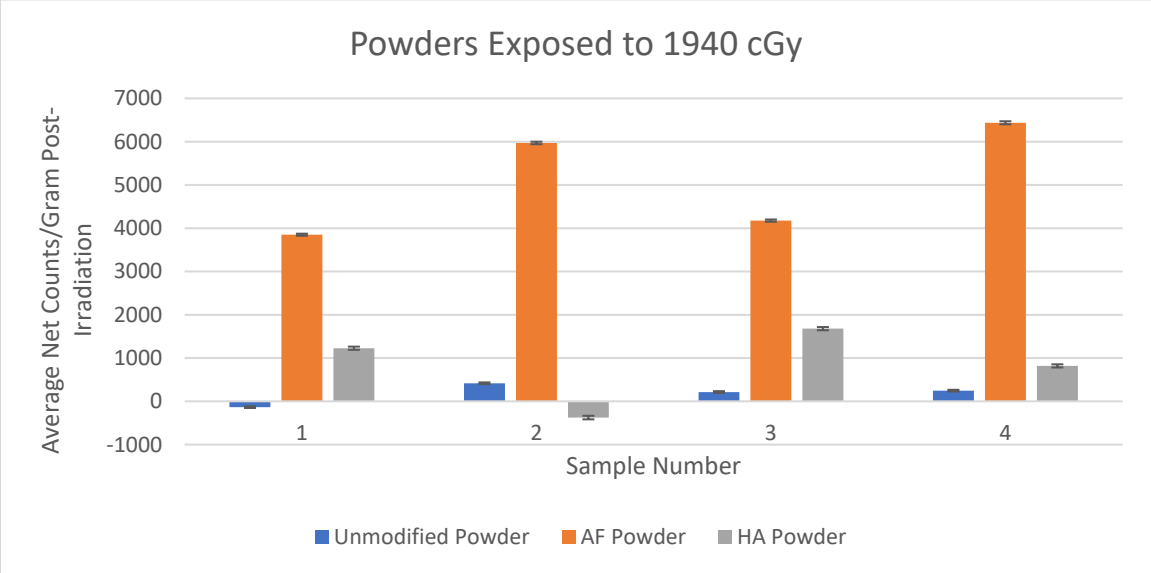

Figure 28: Average difference in counts/gram post-irradiation for 4 samples of unmodified Al_2O_3, AF, and HA powders exposed to 1940 cGy.

Table 16: Average difference in counts/gram post-irradiation for four samples of unmodified Al_2O_3, AF, and HA powders exposed to 1940 cGy.

Powder Type and Sample Number	Average Net Counts/gram	Error (counts)
Unmodified Al_2O_3 Powder Sample 1	-134.33	19.28
Unmodified Al_2O_3 Powder Sample 2	417.72	19.58
Unmodified Al_2O_3 Powder Sample 3	214.29	20.49
Unmodified Al_2O_3 Powder Sample 4	246.58	19.65
AF Powder Sample 1	3850.39	24.06
AF Powder Sample 2	5970.00	28.88
AF Powder Sample 3	4175.26	26.08
AF Powder Sample 4	6436.37	35.19
HA Powder Sample 1	1227.27	37.11
HA Powder Sample 2	-375.00	41.31
HA Powder Sample 3	1680.00	36.66
HA Powder Sample 4	818.18	36.56
Unmodified Al_2O_3 Powder Average	186.06	36.56
AF Powder Average	5108	14.43
HA Powder Average	837.61	18.98

A Shapiro-Wilk test was performed on the average net counts/gram for all 4 samples of each of the 3 powders to determine if the results follow a normal distribution. Table 17, Table 18, and Table 19 are the tables used to calculate the W statistic of the net counts/gram for all unmodified Al_2O_3, AF, and HA samples exposed to 1940 cGy.

Table 17: Shapiro-Wilk test results of unmodified Al_2O_3 samples exposed to 1940 cGy.

Order	$\mathbf{x_i}$	$\mathbf{(x_i - \bar{x})^2}$	$\mathbf{a_i}$	$\mathbf{a_i x_i}$
1	-134.33	102653	0.6872	-92.312
2	214.29	796.651	0.1677	35.9364
3	246.58	3662.07	-0.1677	-41.351
4	417.72	53664	-0.6872	-287.06
$\mathbf{(\sum_{i=1}^{n} a_i x_i)^2}$			148059	
$\mathbf{\sum_{i=1}^{n} (x_i - \bar{x})^2}$			160776	
$\mathbf{W = \frac{(\sum_{i=1}^{n} a_i x_{(i)})^2}{\sum_{i=1}^{n} (x_i - \bar{x})^2}}$			0.92	

Table 18: Shapiro-Wilk test results of AF samples exposed to 1940 cGy.

Order	x_i	$(x_i - \bar{x})^2$	a_i	$a_i x_i$
1	3850.4	1581621	0.6872	2645.99
2	4175.3	869976	0.1677	700.198
3	5970	743001	-0.1677	-1001.2
4	6436.4	1764580	-0.6872	-4423.1
	$(\sum_{i=1}^{n} a_i x_i)^2$		4318377	
	$\sum_{i=1}^{n} (x_i - \bar{x})^2$		4959178	
	$W = \frac{(\sum_{i=1}^{n} a_i x_{(i)})^2}{\sum_{i=1}^{n} (x_i - \bar{x})^2}$		0.87	

Table 19: Shapiro-Wilk test results of HA samples exposed to 1940 cGy.

Order	x_i	$(x_i - \bar{x})^2$	a_i	$a_i x_i$
1	-375	1470429	0.6872	-257.7
2	818.18	377.622	0.1677	137.209
3	1227.27	151833	-0.1677	-205.81
4	1680	709617	-0.6872	-1154.5
	$(\sum_{i=1}^{n} a_i x_i)^2$		2192770	
	$\sum_{i=1}^{n} (x_i - \bar{x})^2$		2332256	
	$W = \frac{(\sum_{i=1}^{n} a_i x_{(i)})^2}{\sum_{i=1}^{n} (x_i - \bar{x})^2}$		0.94	

The W statistic for all three sets of samples is larger than the critical value of 0.748 so the data sets of the net counts/gram are normally distributed.

Since the data sets of the net counts/gram are normally distributed a F-Test Two-Sample for Variances were performed comparing the variances of the AF samples to the unmodified Al_2O_3 samples and the HA samples to the unmodified Al_2O_3. Table 20 and Table 21 are the results of the two tests.

Table 20: F-Test Two-Sample for Variances for AF samples and unmodified Al_2O_3 samples exposed to 1940 cGy.

	AF Samples	**Unmodified Al_2O_3 Samples**
Mean	5108.03	186.065
Variance	1653059	53591.9
Observations	4	4
df	3	3
F	30.8453	
P(F<=f) one-tail	0.00936	
F Critical one-tail	9.27663	

Table 21: F-Test Two-Sample for Variances for HA samples and unmodified Al_2O_3 samples exposed to 1940 cGy.

	HA Samples	Unmodified Al_2O_3 Samples
Mean	837.613	186.065
Variance	777419	53591.9
Observations	4	4
df	3	3
F	14.5063	
P(F<=f) one-tail	0.02726	
F Critical one-tail	9.27663	

The F statistic is greater than the critical value in both tests so it can be concluded that the variances of the AF and HA average net counts/gram data set is no equal to the variances of the unmodified Al_2O_3 average net counts/gram data set.

Since the variances are not equal, the t-Test: Two-Sample Assuming Unequal Variances is performed. Table 22 and Table 23 are the results of the two tests.

Table 22: t-Test: Two-Sample Assuming Unequal Variances for AF samples and unmodified Al_2O_3 samples exposed to 1940 cGy.

	AF Samples	**Unmodified Al_2O_3 Samples**
Mean	5108.03	186.065
Variance	1653059	53591.9
Observations	4	4
Hypothesized Mean Difference	0	
df	3	
t Stat	7.53522	
P(T<=t) one-tail	0.00242	
t Critical one-tail	2.35336	
P(T<=t) two-tail	0.00485	
t Critical two-tail	3.18245	

Table 23: t-Test: Two-Sample Assuming Unequal Variances for HA samples and unmodified Al_2O_3 samples exposed to 1940 cGy.

	HA Samples	Unmodified Al_2O_3 Samples
Mean	837.614	186.064
Variance	777420	53591.5
Observations	4	4
Hypothesized Mean Difference	0	
df	3	
t Stat	1.42947	
P(T<=t) one-tail	0.12411	
t Critical one-tail	2.35336	
P(T<=t) two-tail	0.24821	
t Critical two-tail	3.18245	

Radiation Sensitivity Testing of Unmodified Al_2O_3, AF, and HA Powders Exposed to Unfiltered X-Ray Beam

Measuring the response of the powders exposed to an unfiltered x-ray beam was performed in almost the exact same way as the powders exposed to 1940 cGy. The only difference is that the 0.3 mm Cu treatment filter was removed, so the powders were exposed to low-energy x-rays and a higher dose. The average counts were divided by the mass of the powder to normalize the readings to counts/gram. The average counts/gram pre-irradiation were subtracted from the counts/gram post-irradiation to determine the average difference in counts/gram and then plotted (Figure 29). The results are summarized in Figure 15.

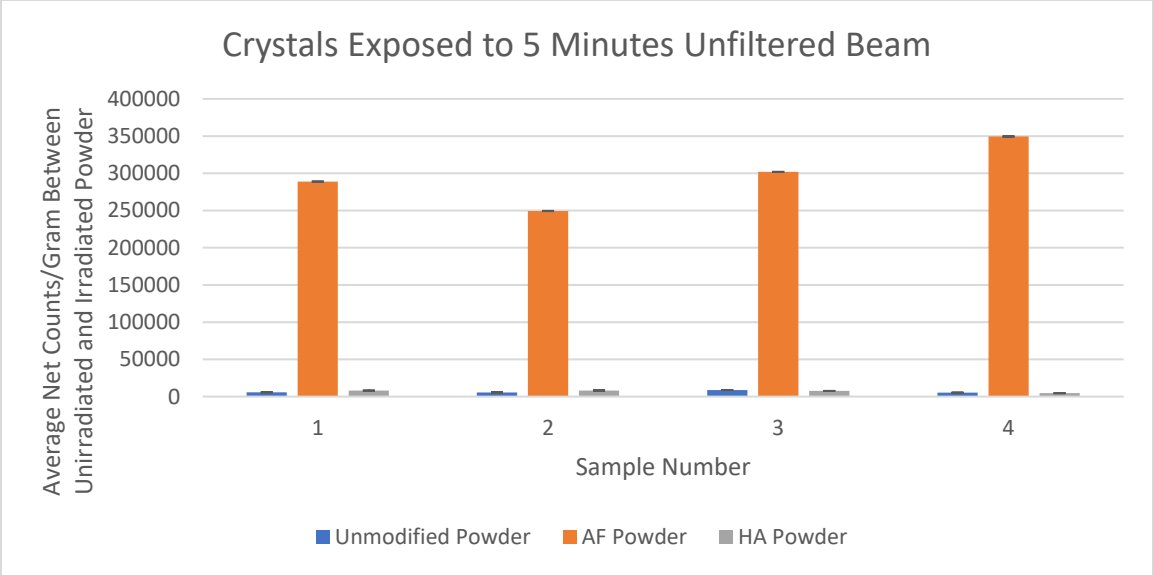

Figure 29: Average difference in counts/gram post-irradiation for 4 samples of unmodified Al_2O_3, AF, and HA powders placed at isocenter of a 40 mm × 40 mm, 225 kVp, 13 mA, x-ray beam from a small animal irradiator with the 0.3 mm Cu filter removed and the beam turned on for 5 minutes.

Table 24: Average difference in counts/gram post-irradiation for 4 samples of unmodified Al_2O_3, AF, and HA powders placed at isocenter of a 40 mm × 40 mm, 225 kVp, 13 mA, x-ray beam from a small animal irradiator with the 0.3 mm Cu filter removed and the beam turned on for 5 minutes.

Powder Type and Sample Number	Average Net Counts/gram	Error of Averages
Unmodified Al_2O_3 Powder Sample 5	5671.23	29.93
Unmodified Al_2O_3 Powder Sample 6	5526.32	29.74
Unmodified Al_2O_3 Powder Sample 7	8810.13	34.48
Unmodified Al_2O_3 Powder Sample 8	5316.46	29.30
AF Powder Sample 5	288890.10	170.76
AF Powder Sample 6	249423.60	159.16
AF Powder Sample 7	301948.50	174.49
AF Powder Sample 8	349500.00	187.77
HA Powder Sample 5	8052.64	45.13
HA Powder Sample 6	8210.53	45.48
HA Powder Sample 7	7578.95	46.00
HA Powder Sample 8	4560.00	40.25
Unmodified Al_2O_3 Powder Average	6331.03	15.47

AF Powder Average	297441	86.67
HA Powder Average	7100.53	22.14

A Shapiro-Wilk test was performed on the average net counts/gram for all 4 samples of each of the 3 powders to determine if the results follow a normal distribution. Table 25, Table 26, and Table 27 are the tables used to calculate the W statistic of the net counts/gram for all unmodified Al_2O_3, AF, and HA dots exposed to 1940 cGy.

Table 25: Shapiro-Wilk test results of unmodified Al_2O_3 samples exposed to an unfiltered beam for 5 minutes.

Order	$\mathbf{x_i}$	$\mathbf{(x_i - \bar{x})^2}$	$\mathbf{a_i}$	$\mathbf{a_i x_i}$
1	5316.46	1029368.04	0.6872	3653.47
2	5526.32	647570.45	0.1677	926.763
3	5671.23	435336.68	-0.1677	-951.07
4	8810.13	6145916.31	-0.6872	-6054.3
$\mathbf{(\sum_{i=1}^{n} a_i x_i)^2}$			5881377.37	
$\mathbf{\sum_{i=1}^{n} (x_i - \bar{x})^2}$			8258191.47	
$\mathbf{W = \frac{(\sum_{i=1}^{n} a_i x_{(i)})^2}{\sum_{i=1}^{n} (x_i - \bar{x})^2}}$			0.71	

Table 26: Shapiro-Wilk test results of AF samples exposed to an unfiltered beam for 5 minutes.

Order	x_i	$(x_i - \bar{x})^2$	a_i	$a_i x_i$
1	249424	2305584272	0.6872	171404
2	288890	73111050.3	0.1677	48446.9
3	301948	20317556.3	-0.1677	-50637
4	349500	2710191540	-0.6872	-240176
	$(\sum_{i=1}^{n} a_i x_i)^2$		5035613080	
	$\sum_{i=1}^{n} (x_i - \bar{x})^2$		5109204419	
	$W = \frac{(\sum_{i=1}^{n} a_i x_{(i)})^2}{\sum_{i=1}^{n} (x_i - \bar{x})^2}$		0.99	

Table 27: Shapiro-Wilk test results of HA samples exposed to an unfiltered beam for 5 minutes.

Order	x_i	$(x_i - \bar{x})^2$	a_i	$a_i x_i$
1	4560	6454292.68	0.6872	3133.63
2	7578.95	228885.696	0.1677	1270.99
3	8052.64	906513.452	-0.1677	-1350.4
4	8210.53	1232100	-0.6872	-5642.3
	$(\sum_{i=1}^{n} a_i x_i)^2$		6698168.59	
	$\sum_{i=1}^{n} (x_i - \bar{x})^2$		8821791.83	
	$W = \frac{(\sum_{i=1}^{n} a_i x_{(i)})^2}{\sum_{i=1}^{n} (x_i - \bar{x})^2}$		0.76	

The W statistic of the unmodified Al_2O_3 samples is less than 0.75 meaning that the null hypothesis is rejected and that the data set of the net counts/gram of the Al_2O_3 samples is not normally distributed.

Since the data set of the net counts/gram for the unmodified Al_2O_3 samples are not normally distributed, a Mann-Whitney U Test was performed comparing the net counts/gram of the AF samples to the unmodified Al_2O_3 samples, and the net counts/gram of the HA samples to the unmodified Al_2O_3. Table 28 and Table 29 are the results of the two tests.

Table 28: Mann-Whitney U Test comparing AF and Unmodified Al_2O_3 samples' average net counts/gram after being exposed to an unfiltered x-ray beam for 5 minutes.

Powder Type and Average Net Counts/gram		**Rank**	
Unmodified Al_2O_3 Average Net Counts/gram	**AF Average Net Counts/gram**	**Unmodified Al_2O_3 Average Net Counts/gram**	**AF Average Net Counts/gram**
5671.23	8052.64	4	6
5526.32	8210.53	3	7
8810.13	7578.95	8	5
5316.46	4560.00	2	1
Rank Sum		17	19
Sample Size		4	4
$\mathbf{U_{AF}} = \mathbf{n_{AF}n_{unmodified}} + \frac{\mathbf{n_{AF}(n_{AF}+1)}}{\mathbf{2}} - \mathbf{R_{AF}}$		0	
$\mathbf{U_{unmodified}} = \mathbf{n_{AF}n_{unmodified}} + \frac{\mathbf{n_{unmodified}(n_{unmodified}+1)}}{\mathbf{2}} - \mathbf{R_{unmodified}}$		16	
Test Statistic		0	
Critical Value		0	

Table 29: Mann-Whitney U Test comparing AF and Unmodified Al_2O_3 samples' average net counts/gram after being exposed to an unfiltered x-ray beam for 5 minutes.

Powder Type and Average Net Counts/gram		**Rank**	
Unmodified Al_2O_3 Average Net Counts/gram	**HA Average Net Counts/gram**	**Unmodified Al_2O_3 Average Net Counts/gram**	**HA Average Net Counts/gram**
5671.23	8052.64	4	6
5526.32	8210.53	3	7
8810.13	7578.95	8	5
5316.46	4560.00	2	1
Rank Sum		17	19
Sample Size		4	4
$\mathbf{U_{HA} = n_{HA}n_{unmodified} + \frac{n_{HA}(n_{HA}+1)}{2} - R_{HA}}$		7	
$\mathbf{U_{unmodified} = n_{HA}n_{unmodified} + \frac{n_{unmodified}(n_{unmodified}+1)}{2} - R_{unmodified}}$		9	
Test Statistic		7	
Critical Value		0	

The measured sensitivity factor increase of the 3 powders was calculated.

$$\text{Sensitivity Factor Increase of AF Powder}$$

$$= \frac{\text{Average Net } \frac{\text{Counts}}{\text{Gram}} \text{ Exposed to Unfiltered Beam}}{\text{Average Net } \frac{\text{Counts}}{\text{Gram}} \text{Exposed to Filtered Beam}}$$

$$= \frac{297{,}440.55 \frac{\text{Counts}}{\text{Gram}}}{5{,}108.01 \frac{\text{Counts}}{\text{Gram}}}$$

$$= 58.23$$

The increase in counts/gram for the AF increased by a factor of 58.23. The other powders were calculated and summarized in Table 30.

Table 30: Sensitivity factor increase for average counts/gram of unmodified Al_2O_3, AF, and HA powders exposed to a 40 mm × 40 mm, 225 kVp, 13 mA, x-ray beam from a small animal irradiator with the 0.3 mm Cu filter removed with the beam turned on for 5 minutes.

Powder Type	Sensitivity Factor Increase
Unmodified Al_2O_3	34.03
AF	58.23
HA	8.48

DISCUSSION

Radiation Sensitivity Testing of Unmodified Al_2O_3, AF, and HA Powders Using X-Ray Beam

The average net counts/gram for both AF and HA powders was higher than the unmodified Al_2O_3 powder, with the average net counts/gram being 5108 and 837.61 for the AF and HA powders respectively, while the average net counts/gram of the unmodified Al_2O_3 powder was 186.06. This seemed to indicate that both the AF and HA methods produce radiosensitive crystals. However, the results of t-Test: Two-Sample Assuming Unequal Variances showed that only the AF powder had a significant difference in average net counts/gram compared to the unmodified Al_2O_3 powder. This means the AF method was able to produce a powder that is significantly more radiosensitive than unmodified Al_2O_3 powder while the HA method did not. The crystals made using the AF method had the largest net increase in counts/gram post-irradiation, an average increase of 5108 counts/gram, and all 4 of the samples had a net increase in counts/gram. Three of the 4 HA powder samples had a positive difference in the net counts/gram. However, HA sample 2 had a negative net difference of -375 counts/gram. Interestingly, the unmodified Al_2O_3 powder also showed a net increase in the average net counts/gram for 3 of its samples, but unmodified Al_2O_3 sample 1 had a net decrease of -134.33 counts/gram. Both the HA and unmodified Al_2O_3 powders had an increase in the net counts/gram for 3 of the 4 samples while one of the samples had a net decrease in counts/gram. This inconsistency across the samples and the results of the t-Test: Two-Sample Assuming Unequal Variances show that the HA method did not increase the radiosensitivity of the crystals as much as the initial results may have indicated.

The crystals made using the AF method had a significant net increase of counts/gram after being exposed to the same dose as the unmodified Al_2O_3 crystals, showing that the crystals

from the AF method add radiosensitivity to the unmodified crystals. The higher increase in counts suggests more carbon ions were incorporated into the Al_2O_3 lattice, enhancing its sensitivity to radiation. Furthermore, all 4 AF samples had a net increase in counts/gram, whereas the other samples did not have a net increase in counts/gram for all samples, showing that AF powder's radiosensitivity is more consistently exhibited.

The AF powder could be further refined and then used to make an OSLD. The AF method is a promising method for producing radiosensitive crystals for dosimetry applications due to the produced powder having a more consistent and significant increase in net counts/gram compared to the HA and unmodified Al_2O_3 powders.

Radiation Sensitivity Testing of Unmodified Al_2O_3, AF, and HA Powders Exposed to Unfiltered X-Ray Beam

All 3 powders had a large increase in net counts/gram compared to the same powders exposed to the filtered x-ray beam, with the largest increase for the AF powders. The increase in counts/gram for the AF powder was a factor of 58.23. This increase is greater than expected if the powder responded only to the dose increase and the known sensitivity to low-energy x-rays. This indicates that the AF powder has an acute sensitivity to low-energy x-rays. The acute sensitivity to low-energy x-rays may be beneficial when applied to medical imaging dosimetry because medical imaging primarily uses low-energy x-rays, so an OSLD that is acutely sensitive to the low-energy x-rays may be highly beneficial. It is unclear at this time why the AF powders had larger than expected increases in sensitivity.

The unmodified Al_2O_3 and HA powders also had an increase in counts/gram. The factor increase for the unmodified Al_2O_3 powder was 34.03, and the factor increase for the HA powder was 7.56. However, statistical analysis using the Mann-Whitney U test showed that the average

net counts/gram for the HA and unmodified Al_2O_3 powder were not significantly different from each other, which shows that the HA method did not produce a powder that is significantly more radiosensitive to low energy x-rays than unmodified Al_2O_3 powder.

The AF methodology enhanced the radiosensitivity of Al_2O_3 by possibly incorporating carbon into the crystalline structure of the Al_2O_3. The enhancement is evident by the significant increase in net counts/gram when compared to the unmodified Al_2O_3 powder. The HA powder also had an increase in its net counts/gram. However, the net counts/gram are not significantly greater than the net counts/gram of the unmodified Al_2O_3 powder showing the HA powder is not significantly more radiosensitive. This means that it is unlikely that the HA method was able to incorporate enough carbon ions into the Al_2O_3 crystal lattice.

Future Work

Further research and tests to refine the AF methodology to optimize the radiosensitivity of the AF powder is warranted. Modification to the HA methodology may be warranted as there were some intriguing results but the method may need to be heavily refined and offers less promising results than the AF methodology. Before refinement and modification of the AF and HA methodologies, x-ray diffraction (XRD) analysis of both powders should be performed. XRD is a non-destructive tool used to determine the crystalline structure of materials (*XRD Basics*, n.d.)XRD would allow us to determine whether and how much carbon is being incorporated into the Al_2O_3 crystal structure or if some other process has occurred.

The crystal size is an essential variable of OSLDs that was not controlled in this experiment. Previous studies have shown that the luminescence strength and the number of counts measured by the PMT varies with individual crystal size (Akselrod et al., 1993). Sieving is a process that separates particles of a sample according to its particle sizes by submitting it to a

mechanical force (Lucka & Hanke, 2016). Implementing a sieving procedure to create samples based on crystal size would allow us to test for the optimal crystal size and maximize radiosensitivity.

The initial carbon concentration of the samples for the AF and HA methodology was 5,000 parts per million (ppm). This concentration was the highest concentration tested in previous studies, and the carbon concentration of a crystal is a critical component that can affect its radiosensitivity. By exploring various concentrations of carbon, it may be found that utilizing a higher or lower concentration of carbon used in the AF or HA methodologies may incorporate more carbon ions into the Al_2O_3 lattice and produce more sensitive powders, and it may be possible to determine the ideal carbon concentration.

Future research may be able to develop more radiosensitive and effective powders through XRD analysis, sieving of powders to control crystal size, and adjusting carbon concentrations of samples. These powders could then be used to produce radiosensitive filament, which would be used to create 3D-printed OSLDs and other radiosensitive models.

This work demonstrates the feasibility of using alternative methods to create OSLD powders made from Al_2O_3 and carbon powder, which could be integrated into commercially available 3D printable filament. This is the first investigation of this type known to the authors. The ability to create OSLD powder made from Al_2O_3 and carbon is essential to further characterize and explore the applications of 3D printing filament with integrated OSLD powder due to the LANDAUER recall making obtaining Al_2O_3:C crystal from a commercial supplier unfeasible. We believe that the Arc Furnace method presents ways to create OSLD crystals and warrants further exploration.

CONCLUSION

The initial question posed by this research was whether it was possible to combine radiosensitive Al_2O_3:C crystals, used to make OSLDs and having well-researched dosimetric properties, with clear NinjaFlex TPU, used to 3D print boluses for patients receiving radiotherapy, to make OSLD 3D printing filament that could be read using a LANDAUER microSTAR reader to measure dose to a patient receiving treatment and to measure the entire radiation field. This research found that it is possible to incorporate Al_2O_3:C into NinjaFlex TPU by cutting up LANDAUER nanoDots, whose primary component is Al_2O_3:C, and NinjaFlex TPU into small pieces, mixing them, and extruding the mixture 3 times through a Filabot EX2 extruder. We were unable to 3D print OSLD dots as the filament kept jamming in the printer nozzle, but we believe that by adjusting the printer's print settings, it should be possible to print objects with the OSLD filament. Rather than 3D printing, we made OSLD dots by placing the filament between two glass microscope slides, heating the slides on a hot plate, pressing down on the slides to compress the filament, and then punching a dot out with an 8 mm diameter punch biopsy tool. The result was Filament Dot (FD) dosimeters, and we compared their dosimetric properties to LANDAUER Dot (LD) dosimeters. We found that the FDs performed similarly to LDs but with a lower strength signal when read. This result makes sense because the physical structure and properties of the Al_2O_3:C crystals were likely unchanged. This result shows that Al_2O_3:C can be incorporated into NinjaFlex TPU to make OSLD filament that researchers may use to 3D print boluses and other radiosensitive objects. These boluses and objects could measure x-ray fields rather than single points while preserving the well-established dosimetric properties of Al_2O_3:C. We found that when 16 FDs were exposed to different doses, they had different counts/cGy responses when measured. We hypothesized there is not a uniform

distribution of Al_2O_3:C in the OSLD filament. We need to refine the methodology to make the OSLD filament because we hypothesize that the Al_2O_3:C is not uniformly distributed throughout the OSLD filament, causing a less predictable signal response to dose. A new source of Al_2O_3:C must be found or made as LANDAUER has recalled all its nanoDot dosimeters and the microSTAR reader. Still, this study has shown it is possible to incorporate established OSLDs into NinjaFlex TPU to create a filament that can measure dose and should be explored further.

In Chapter 2, we explored whether it was possible to synthesize radiosensitive crystal that the LANDAUER microSTAR could read by starting with powdered aluminum oxide and powdered carbon and applying either the Arc Furnace or Hot Acid methodology. We found that the Arc Furnace methodology can produce crystals that are significantly more radiosensitive than unmodified Al_2O_3 crystals which can be read by the microSTAR. The Arc Furnace methodology producing radiosensitive powder is significant because sourcing the necessary carbon-doped aluminum oxide necessary to make OSLD filament from a commercial supplier is cost-prohibitive and no longer possible due to LANDAUER's recall of the nanoDot dosimeter, but by being able to produce radiosensitive crystals ourselves, research into the OSLD filament can continue. Additionally, this research is the first of its kind where an Arc Furnace was used to create radiosensitive powders, opening a new field of research to develop novel OSLDs. The Arc Furnace and Hot Acid methodologies are still in the preliminary phases, and much refinement is required to improve the radiosensitivity, accuracy, and precision of the powders, as well as further characterization. Even though there is much refinement, and a substantial amount of work needed, this work has shown that the Arc Furnace methodology presents new ways to create radiosensitive powders that we can use to make OSLDs and OSLD filament, and research into 3D printing boluses and models with OSLD filament can continue.

REFERENCES

1.3.6.7.3. Upper Critical Values of the F Distribution. (n.d.). Retrieved September 25, 2024, from https://itl.nist.gov/div898/handbook/eda/section3/eda3673.htm

13.5: Test of Two Variances. (2015, October 29). Statistics LibreTexts. https://stats.libretexts.org/Bookshelves/Introductory_Statistics/Introductory_Statistics_1e_(OpenStax)/13%3A_F_Distribution_and_One-Way_ANOVA/13.05%3A_Test_of_Two_Variances

Akselrod, M. S., Angersnap Larsen, N., Whitley, V., & McKeever, S. W. S. (1999). Thermal Quenching of F-centre Luminescence in Al2O3:C. *Radiation Protection Dosimetry*, *84*(1–4), 39–42. https://doi.org/10.1093/oxfordjournals.rpd.a032763

Akselrod, M. S., Bøtter-Jensen, L., & McKeever, S. W. S. (2006). Optically stimulated luminescence and its use in medical dosimetry. *Radiation Measurements*, *41*, S78–S99. https://doi.org/10.1016/j.radmeas.2007.01.004

Akselrod, M. S., & Gorelova, E. A. (1993). Deep traps in highly sensitive α-Al2O3:C TLD crystals. *Nuclear Tracks and Radiation Measurements*, *21*(1), 143–146. https://doi.org/10.1016/1359-0189(93)90065-H

Akselrod, M. S., Kortov, V. S., & Gorelova (Invited), E. A. (1993). Preparation and Properties of Alpha-Al2O3:C. *Radiation Protection Dosimetry*, *47*(1–4), 159–164. https://doi.org/10.1093/rpd/47.1-4.159

Akselrod, M. S., Kortov, V. S., Kravetsky, D. J., & Gotlib, V. I. (1990). Highly Sensitive Thermoluminescent Anion-Defect a-Al2O3:C Single Crystal Detectors. *Radiation Protection Dosimetry*, *33*(1–4), 119–122.

Akselrod, M. S., & McKeever, S. W. S. (1999). A Radiation Dosimetry Method Using Pulsed Optically Stimulated Luminescence. *Radiation Protection Dosimetry*, *81*(3), 167–175. https://doi.org/10.1093/oxfordjournals.rpd.a032583

Alexander, C. S., & McKeever, S. W. S. (1998). Phototransferred thermoluminescence. *Journal of Physics D: Applied Physics*, *31*(20), 2908–2920. https://doi.org/10.1088/0022-3727/31/20/027

Almond, P. R., Biggs, P. J., Coursey, B. M., Hanson, W. F., Huq, M. S., Nath, R., & Rogers, D. W. O. (1999). AAPM's TG-51 protocol for clinical reference dosimetry of high-energy photon and electron beams. *Medical Physics*, *26*(9), 1847–1870. https://doi.org/10.1118/1.598691

Barvinschi, F., Santailler, J.-L., Duffar, T., & Le Gal, H. (1999). Modelling of Verneuil process for the sapphire crystal growth. *Journal of Crystal Growth*, *198–199*, 239–245. https://doi.org/10.1016/S0022-0248(98)01240-8

Beddar, A. S., Mackie, T. R., & Attix, F. H. (1992). Water-equivalent plastic scintillation detectors for high-energy beam dosimetry: I. Physical characteristics and theoretical

considerations. *Physics in Medicine & Biology*, *37*(10), 1883. https://doi.org/10.1088/0031-9155/37/10/006

Belhaj, O. E., Boukhal, H., Chakir, E. M., Bellahsaouia, M., Belhaj, S., Sadeq, Y., Tazi, M., El Khoukhi, T., Hadouachi, M., & Laazouzi, K. (2023). Dose metrology: TLD/OSL dose accuracy and energy response performance. *Nuclear Engineering and Technology*, *55*(2), 717–724. https://doi.org/10.1016/j.net.2022.10.029

Bolus Material for External Beam Radiation Therapy. (n.d.). Mick Radio-Nuclear Instruments, Inc. https://www.micknuclear.com/fileadmin/mick/user_uploads/PDF/Facht_sheet_Superflab__Revision_E__USA.pdf

Brosi, P., Stuessi, A., Verdun, F. R., Vock, P., & Wolf, R. (2011). Copper filtration in pediatric digital X-ray imaging: Its impact on image quality and dose. *Radiological Physics and Technology*, *4*(2), 148–155. https://doi.org/10.1007/s12194-011-0115-4

Bulur, E. (2000). A simple transformation for converting CW-OSL curves to LM-OSL curves. *Radiation Measurements*, *32*(2), 141–145. https://doi.org/10.1016/S1350-4487(99)00247-4

Burleson, S., Baker, J., Hsia, A. T., & Xu, Z. (2015). Use of 3D printers to create a patient-specific 3D bolus for external beam therapy. *Journal of Applied Clinical Medical Physics*, *16*(3), 166–178. https://doi.org/10.1120/jacmp.v16i3.5247

Colin Cameron, A., & Windmeijer, F. A. G. (1997). An *R*-squared measure of goodness of fit for some common nonlinear regression models. *Journal of Econometrics*, *77*(2), 329–342. https://doi.org/10.1016/S0304-4076(96)01818-0

Compton, A. H. (1923). A Quantum Theory of the Scattering of X-rays by Light Elements. *Physical Review*, *21*(5), 483–502. https://doi.org/10.1103/PhysRev.21.483

Daniels, F., Charles A. Boyd, & Donald F. Saunders. (1953). Thermoluminescence as a Research Tool. *Science*, *117*(3040), 343–349.

de Haas, J. T. M., & Dorenbos, P. (2011). Methods for Accurate Measurement of the Response of Photomultiplier Tubes and Intensity of Light Pulses. *IEEE Transactions on Nuclear Science*, *58*(3), 1290–1296. IEEE Transactions on Nuclear Science. https://doi.org/10.1109/TNS.2011.2141683

Einstein, A. (1905). Über einen die Erzeugung und Verwandlung des Lichtes betreffenden heuristischen Gesichtspunkt. *Annalen Der Physik*, *322*(6), 132–148. https://doi.org/10.1002/andp.19053220607

Ezzell, G. A., Galvin, J. M., Low, D., Palta, J. R., Rosen, I., Sharpe, M. B., Xia, P., Xiao, Y., Xing, L., & Yu, C. X. (2003). Guidance document on delivery, treatment planning, and clinical implementation of IMRT: Report of the IMRT subcommittee of the AAPM radiation therapy committee. *Medical Physics*, *30*(8), 2089–2115. https://doi.org/10.1118/1.1591194

F42 Committee. (n.d.). *Terminology for Additive Manufacturing Technologies,*. ASTM International. https://doi.org/10.1520/F2792-12A

Geuskens, G., & David, C. (1979). THE PHOTO-OXIDATION OF POLYMERS. A COMPARISON WITH LOW MOLECULAR WEIGHT COMPOUNDS. In *Photochemistry–7* (pp. 233–240). Elsevier. https://doi.org/10.1016/B978-0-08-022358-2.50007-7

Göppert-Mayer, M. (1931). Über Elementarakte mit zwei Quantensprüngen. *Annalen Der Physik*, *401*(3), 273–294. https://doi.org/10.1002/andp.19314010303

Hashimoto, T., Sato, F., Tamaki, S., Kusaka, S., Miyamaru, H., & Murata, I. (2019a). Fabrication of radiophotoluminescence dosimeter with 3D-printing technology. *Radiation Measurements*, *124*, 141–145. https://doi.org/10.1016/j.radmeas.2019.04.012

Hashimoto, T., Sato, F., Tamaki, S., Kusaka, S., Miyamaru, H., & Murata, I. (2019b). Fabrication of radiophotoluminescence dosimeter with 3D-printing technology. *Radiation Measurements*, *124*, 141–145. https://doi.org/10.1016/j.radmeas.2019.04.012

Hsu, S.-H., Roberson, P. L., Chen, Y., Marsh, R. B., Pierce, L. J., & Moran, J. M. (2008). Assessment of skin dose for breast chest wall radiotherapy as a function of bolus material. *Physics in Medicine and Biology*, *53*(10), 2593–2606. https://doi.org/10.1088/0031-9155/53/10/010

Huffman, F. (2003). Thermionic Energy Conversion. In R. A. Meyers (Ed.), *Encyclopedia of Physical Science and Technology (Third Edition)* (pp. 627–638). Academic Press. https://doi.org/10.1016/B0-12-227410-5/00772-9

Jursinic, P. A. (2007). Characterization of optically stimulated luminescent dosimeters, OSLDs, for clinical dosimetric measurements. *Medical Physics*, *34*(12), 4594–4604. https://doi.org/10.1118/1.2804555

Jursinic, P. A. (2010). Changes in optically stimulated luminescent dosimeter (OSLD) dosimetric characteristics with accumulated dose. *Medical Physics*, *37*(1), 132–140. https://doi.org/10.1118/1.3267489

Khan, F. M., & Gibbons (Jr.), J. P. (2014). *The Physics of Radiation Therapy* (5th ed.). Lippincott Williams & Wilkins.

Knoll, G. F. (2010). *Radiation Detection and Measurement*. John Wiley & Sons.

Kortov, V. S. (1985). Role of Non-Stoichiometry in Exoelectron Oxide Emission I. Emission Centers. *Japanese Journal of Applied Physics*, *24*(S4), 65. https://doi.org/10.7567/JJAPS.24S4.65

Lee, S.-Y., & Jai Lee, K. (2001). Development of a personal dosimetry system based on optically stimulated luminescence of α-Al2O3: C for mixed radiation fields. *Applied Radiation and Isotopes*, *54*(4), 675–685. https://doi.org/10.1016/S0969-8043(00)00302-X

Lucka, M., & Hanke, T. (2016). *Sieve Analysis Different sieving methods for a variety of applications*.

Lynch, N., Monajemi, T., & Robar, J. L. (2020). Characterization of novel 3D printed plastic scintillation dosimeters. *Biomedical Physics & Engineering Express*, *6*(5), 055014. https://doi.org/10.1088/2057-1976/aba880

Mann, H. B., & Whitney, D. R. (1947). On a Test of Whether one of Two Random Variables is Stochastically Larger than the Other. *The Annals of Mathematical Statistics*, *18*(1), 50–60.

Martin, T. W., Boss, M.-K., LaRue, S. M., & Leary, D. (2020). 3D-printed bolus improves dose distribution for veterinary patients treated with photon beam radiation therapy. *The Canadian Veterinary Journal*, *61*(6), 638–644.

McKeever, S. W. S., Akselrod, M. S., & Markey, B. G. (1996). Pulsed Optically Stimulated Luminescence Dosimetry Using Alpha-Al2O3:C. *Radiation Protection Dosimetry*, *65*(1–4), 267–272. https://doi.org/10.1093/oxfordjournals.rpd.a031639

Monajemi, T. T., & Ruiz, E. A. (2018). Application of plastic scintillating fibres to surface dosimetry in megavoltage photon and electron beams: Considerations for Cerenkov correction. *Physics in Medicine & Biology*, *63*(18), 185003. https://doi.org/10.1088/1361-6560/aad9b6

Moscovitch, M., Tawil, R. A., & Svinkin, M. (1993). Light Induced Fading in Alpha-Al2O3:C. *Radiation Protection Dosimetry*, *47*(1–4), 251–253. https://doi.org/10.1093/rpd/47.1-4.251

nanoDot™—Dosimetry Badges | LANDAUER. (n.d.). Retrieved July 25, 2024, from https://www.landauer.com/product/nanodot

Nath, R., Anderson, L. L., Luxton, G., Weaver, K. A., Williamson, J. F., & Meigooni, A. S. (1995). Dosimetry of interstitial brachytherapy sources: Recommendations of the AAPM Radiation Therapy Committee Task Group No. 43. *Medical Physics*, *22*(2), 209–234. https://doi.org/10.1118/1.597458

Novakovic, K., Katsikas, L., & Popovic, I. (2000). The thermal degradation of poly(iso-butyl methacrylate) and poly(sec-butyl methacrylate). *Journal of the Serbian Chemical Society*, *65*(12), 867–875. https://doi.org/10.2298/JSC0012867N

Perks, C. A., Yahnke, C., & Million, M. (2008). *Medical dosimetry using optically stimulated luminescence dots and microStar readers*. IRPA 12: 12 International congress of the International Radiation Protection Association (IRPA): Strengthening radiation protection worldwide, Argentina.

Polyakov, S. V. (2013). Photomultiplier Tubes. In *Experimental Methods in the Physical Sciences* (Vol. 45, pp. 69–82). Elsevier. https://doi.org/10.1016/B978-0-12-387695-9.00003-2

Rana, S., & Rogers, K. (2013). Dosimetric evaluation of Acuros XB dose calculation algorithm with measurements in predicting doses beyond different air gap thickness for smaller and larger field sizes. *Journal of Medical Physics / Association of Medical Physicists of India*, *38*(1), 9. https://doi.org/10.4103/0971-6203.106600

Ruxton, G. D. (2006). The unequal variance t-test is an underused alternative to Student's t-test and the Mann–Whitney U test. *Behavioral Ecology*, *17*(4), 688–690. https://doi.org/10.1093/beheco/ark016

Sato, F., Zushi, N., Maekawa, T., Kato, Y., Murata, I., Shimizu, K., Yamamoto, T., & Iida, T. (2014). Visualization of high radiation field by radiophotoluminescence photography. *Radiation Measurements*, *68*, 23–30. https://doi.org/10.1016/j.radmeas.2014.06.011

Schembri, V., & Heijmen, B. J. M. (2007). Optically stimulated luminescence (OSL) of carbon-doped aluminum oxide for film dosimetry in radiotherapy. *Medical Physics*, *34*(6Part1), 2113–2118. https://doi.org/10.1118/1.2737160

Shahrubudin, N., Lee, T. C., & Ramlan, R. (2019). An Overview on 3D Printing Technology: Technological, Materials, and Applications. *Procedia Manufacturing*, *35*, 1286–1296. https://doi.org/10.1016/j.promfg.2019.06.089

SHAPIRO, S. S., & WILK, M. B. (1965). An analysis of variance test for normality (complete samples)†. *Biometrika*, *52*(3–4), 591–611. https://doi.org/10.1093/biomet/52.3-4.591

Summers (INVITED), G. P. (1984). Thermoluminescence in Single Crystal Alpha-Al2O3. *Radiation Protection Dosimetry*, *8*(1–2), 69–80. https://doi.org/10.1093/oxfordjournals.rpd.a083043

Sureiman, O., & Mangera, C. M. (2020). F-Test of Overall Significance in Regression Analysis Simplified. *Journal of the Practice of Cardiovascular Sciences*, *6*(2), 116. https://doi.org/10.4103/jpcs.jpcs_18_20

Swinhart, M., DeLarme, A., & Diaz, A. L. (2022). A study of the impact of oxygen vacancies on the VUV efficiency of rare-earth doped YBO3 via Ca2+ co-doping. *Optical Materials*, *127*, 112261. https://doi.org/10.1016/j.optmat.2022.112261

Tofail, S. A. M., Koumoulos, E. P., Bandyopadhyay, A., Bose, S., O'Donoghue, L., & Charitidis, C. (2018). Additive manufacturing: Scientific and technological challenges, market uptake and opportunities. *Materials Today*, *21*(1), 22–37. https://doi.org/10.1016/j.mattod.2017.07.001

Viamonte, A., da Rosa, L. a. R., Buckley, L. A., Cherpak, A., & Cygler, J. E. (2008). Radiotherapy dosimetry using a commercial OSL system. *Medical Physics*, *35*(4), 1261–1266. https://doi.org/10.1118/1.2841940

Vishwanathan, H. (2023, August 29). *URGENT - Medical Device Recall—RESPONSE REQUIRED*. LANDAUER. https://www.landauer.com/product/nanodot

Vyas, V., Palmer, L., Mudge, R., Jiang, R., Fleck, A., Schaly, B., Osei, E., & Charland, P. (2013). On bolus for megavoltage photon and electron radiation therapy. *Medical Dosimetry*, *38*(3), 268–273. https://doi.org/10.1016/j.meddos.2013.02.007

Walker, F. D., Colyott, L. E., Agersnap Larsen, N., & McKeever, S. W. S. (1996). The wavelength dependence of light-induced fading of thermoluminescence from α-Al2O3:C. *Radiation Measurements*, *26*(5), 711–718. https://doi.org/10.1016/S1350-4487(97)82885-5

Watanabe, Y., Inoue, S., Saito, A., Kawakawami, M., & Furukawa, H. (2022). 3D printable inter cross-linking network (ICN) gels for reversible transparency control with water content. *Microsystem Technologies*, *28*(1), 167–171. https://doi.org/10.1007/s00542-019-04550-9

Welford, B. P. (1962). Note on a Method for Calculating Corrected Sums of Squares and Products. *Technometrics*. https://www.tandfonline.com/doi/abs/10.1080/00401706.1962.10490022

XRD Basics. (n.d.). Retrieved August 5, 2024, from https://www.physics.upenn.edu/~heiney/datasqueeze/basics.html

Y.C., D., & Hsu, S.-M. (2011). Radio-Photoluminescence Glass Dosimeter (RPLGD). In H. Gali-Muhtasib (Ed.), *Advances in Cancer Therapy*. InTech. https://doi.org/10.5772/23710

APPENDIX A: DOSE RATE MEASUREMENTS OF THE SMALL ANIMAL IRRADIATOR WITH AND WITHOUT THE COPPER TREATMENT FILTER

Removal of the 0.3 mm Cu treatment filter creates a more intense x-ray beam, and the dose delivered increases. To determine how much the dose delivered to isocenter increases, a PinPoint 3D Ion Chamber (PTW Freiburg, Freiburg im Breisgau, Baden-Württemberg, Germany), a low-energy ion chamber with a buildup cap, was placed at isocenter of the Small Animal Irradiator (Figure 30).

The principle of the ion chamber, or free-air ionization chamber, is that as an x-ray beam passes through air, free electrons are put in motion by the photoelectric effect, Compton effect, or pair production. These free electrons are fast-moving and produce ionization along their tracks. An electric field is produced within the chamber by applying a voltage across ion-collection plates; the negatively charged plate collects positive charges created by the ionization, and the positively charged plate collects negative charges. A current is produced and measured by an electrometer. However, some free electrons may cause ionizations outside of the electric field, so the produced positive and negative charges are not collected. The loss of charge is compensated by free electrons which were generated outside of the electric field traveling into the field and causing ionizations and creating a condition known as electronic equilibrium and electronic equilibrium must be satisfied for proper use of ionization chambers (Khan & Gibbons (Jr.), 2014).

The type of ion chamber used is known as a thimble chamber, which places a known volume of air, the chamber's air cavity, at the isocenter, and the x-ray beam irradiates the volume uniformly. A solid shell, with an effective atomic number equal to air, encloses the air and is sufficiently thick such that electronic equilibrium occurs within the chamber's air cavity. When measuring x-rays in the 100-250 kVp range, the solid shell thickness would need to be 1 mm, but

most thimble chambers have a wall thickness of 1 mm or less. This is compensated by placing a close-fitting Plexiglas or other plastic cap on top of the solid shell to bring the wall thickness up to the required thickness, known as buildup caps (Khan & Gibbons (Jr.), 2014).

The beam settings were 225 kVp, 13 mA, 40 × 40 mm field size and the beam was turned on for 30 seconds. The current was measured in milliamps (mA) and the total charge measured by the ion chamber was measured in nanocoulombs (nC).

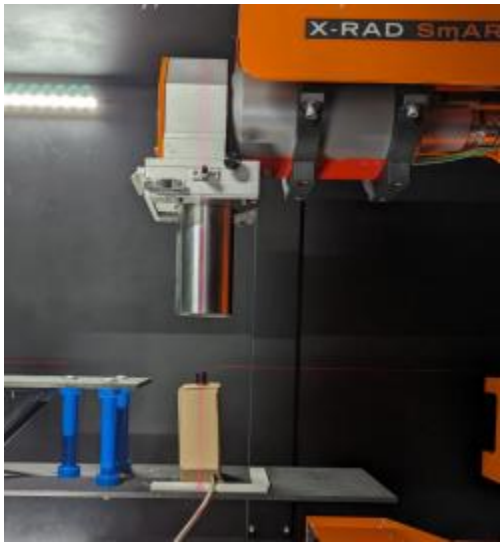

Figure 30: Low energy ion chamber placed at isocenter of the Small Animal Irradiator.

The average total charge measured by the ion chamber of the filtered beam was 3.43 nC, and the average total charge of the unfiltered beam was 12.90 nC (Table 31 and Table 32).

Table 31: Low energy ion chamber at isocenter with buildup cap, read 3 times while exposed to the Small Animal Irradiator's 225 kVp, 13 mA, 40 × 40 mm, x-ray beam for 30 seconds with the Cu treatment filter in.

Reading Number	Reading (nC)
1	3.43
2	3.43
3	3.43
Average	3.43

Table 32: Low energy ion chamber at isocenter with buildup cap, read 3 times while exposed to the Small Animal Irradiator's 225 kVp, 13 mA, 40 × 40 mm, x-ray beam for 30 seconds with the Cu treatment filter removed.

Reading Number	Reading (nC)
1	12.92
2	12.89
3	12.89
Average	12.90

The increase in exposure and dose of the unfiltered versus filtered beam is proportional to the charge measured by the ion chamber, so dividing the average total charge of the unfiltered beam by the average total charge of the filtered beam would yield the proportional increase in exposure by removing the filter.

$$\text{Increase in Exposure} = \frac{\text{Average Measured Charge of the Unfiltered Beam (nC)}}{\text{Average Measured Charge of the Filtered Beam (nC)}}$$

$$= \frac{12.90 \text{ nC}}{3.43 \text{ nC}}$$

$$= 3.76$$

The amount of ionizing radiation exposure at the isocenter of the Small Animal Irradiator 225 kVp, 13 mA, 40 × 40 mm, the x-ray beam is 3.76 times greater with the 0.3 mm Cu filter removed.

APPENDIX B: MEASUREMENT DATA FOR **Error! Reference source not found.**

Table 33: Measurement data for average counts of 10 readings of 4 LDs after being exposed to a dose of 51.6, 103.2, 148.35, and 199.95 cGy exposed with a 40 × 40 mm, 225 kV, 13 mA x-ray beam from the small animal irradiator.

Time In Beam (seconds)			
8	16	23	31
Calculated Dose (cGy)			
51.6	103.2	148.35	199.95
Counts			
89875	188588	277582	394335
85209	177007	259738	358843
84573	168909	243639	348650
80651	166145	237526	347722
81387	165595	237752	343315
81260	165491	234324	338929
80298	164489	232331	337707
80034	167278	234443	337963
80147	164381	235165	337326
83790	164723	233479	334529
Average Counts			
82722.4	169260.6	242597.9	347931.9
Error of Average Counts			
90.95	130.10	155.76	186.53

APPENDIX C: MEASUREMENT DATA FOR **Error! Reference source not found.**

Table 34: Measurement data for average counts of 10 readings of 4 FDs after being exposed to a dose of 51.6, 103.2, 148.35, and 199.95 cGy exposed with a 40 × 40 mm, 225 kV, 13 mA x-ray beam from the small animal irradiator.

Time In Beam (seconds)			
8	16	23	31
Calculated Dose (cGy)			
51.6	103.2	148.35	199.95
Counts			
3105	6500	11147	15252
3011	6446	11327	15256
3120	6438	11130	14908
2924	6344	11616	15189
3052	6313	11114	14994
3031	6455	11138	14905
2981	6307	11079	14647
2896	6199	11134	14817
3037	6273	10759	14748
3000	6344	11019	14620
Average Counts			
3015.7	6361.9	11146.3	14933.6
Error of Average Counts			
17.37	25.22	33.39	38.64

APPENDIX D: MEASUREMENT DATA FOR **Error! Reference source not found.** AND F IGURE 10

Table 35: Measurement data for the number of counts measured by the LANDAUER microSTAR when reading each of the four LD dosimeters, each exposed to 51.6, 103.2, 148.35, and 199.95 cGy using a 40 × 40 mm, 225 kV, 13 mA x-ray beam from a small animal irradiator.

Time In Beam (seconds)			
8	16	23	31
Calculated Dose (cGy)			
51.6	103.2	148.35	199.95
Counts			
85209	168909	259738	394335
84573	166145	243639	358843
80651	165595	237526	348650
81387	165491	237752	347722
81260	164489	234324	343315
80298	167278	232331	338929
80034	164381	234443	337707
80147	164723	235165	337963
83790	164978	233479	337326
79592	163608	234157	334529
82450	158737	231371	334525
80997	164543	228367	330146
77832	162083	231313	332386
79504	159979	232470	333601
80195	161945	225881	329657

79564	161461	230299	331908
79102	158840	230857	332160
78986	160239	229292	331767
80814	163061	229271	330265
78277	158555	227364	330902
77517	161046	227131	326999
77876	159327	230411	331849
78332	160093	231660	325998
79155	160663	229843	330805
79350	160985	227512	329871
78923	156148	228659	329817
79330	160260	227442	329980
78025	158614	228302	328616
78141	160081	225308	327435
79228	160737	226236	329333
77964	160769	228835	325646
80353	158987	227239	333538
78764	159416	226465	325568
78678	159584	227666	328840
81911	159813	226010	323796
76674	160014	227514	327712
77461	158454	223341	327711
76634	155726	226686	326911

76995	159418	223172	324637
76812	156969	226036	325439
78247	158477	223126	324726
79188	157721	226376	323871
79140	157434	221289	322432
77374	156149	224507	325078
77837	157869	221565	322615
75592	158578	222848	326999
77000	155112	222743	323064
77170	154049	220764	318688
75539	157781	220343	322946
77070	158762	223948	324122
78910	156492	225309	325828
76449	155313	222184	321736
76482	157308	219057	320647
76849	156327	223122	324484
77303	155940	221798	319525
78633	156607	220212	320479
75057	155818	223400	321565
77041	156516	221518	319782
79374	155177	222909	321050
77793	157428	222132	320209
77128	155617	223632	322537

75839	156299	220097	317186
77039	154911	222858	323006
77819	158361	220604	319559
76975	154325	223478	321570
76462	157652	219740	318253
76784	155999	221552	319864
77626	156179	220430	320284
76878	157046	221128	320397
75378	154222	221869	319647
75886	156995	218160	317276
75808	154053	221046	323276
76190	153769	218885	316524
76790	153004	220354	318580
77636	154771	218320	319659
75301	156012	219626	319288
76851	153115	221806	319992
75370	156294	217390	319290
76963	154437	221645	319881
75210	153551	220206	316028
75409	153993	220465	319450
75757	154986	217314	316031
76589	153838	221239	319302
75684	153134	217311	316406

76231	153795	217234	315970
74550	156423	221243	319370
75848	152504	216242	315954
74579	154364	219014	314383
77056	152703	217011	316918
74619	154076	219075	315922
76178	152201	216864	315466
75748	151518	216095	315623
75732	153032	217956	313273
75669	152005	215687	315297
75796	153120	218813	314021
78224	155195	220493	315833
75322	152564	218223	315396
76309	154551	219007	315253
75876	154032	216701	315933
74875	153124	216000	312284
Error (counts)			
291.91	410.99	509.64	627.96
290.81	407.61	493.60	599.04
283.99	406.93	487.37	590.47
285.28	406.81	487.60	589.68
285.06	405.57	484.07	585.93
283.37	409.00	482.01	582.18

282.90	405.44	484.19	581.13
283.10	405.86	484.94	581.35
289.47	406.17	483.20	580.80
282.12	404.48	483.90	578.38
287.14	398.42	481.01	578.38
284.60	405.64	477.88	574.58
278.98	402.60	480.95	576.53
281.96	399.97	482.15	577.58
283.19	402.42	475.27	574.16
282.07	401.82	479.89	576.11
281.25	398.55	480.48	576.33
281.04	400.30	478.84	575.99
284.28	403.81	478.82	574.69
279.78	398.19	476.83	575.24
278.42	401.31	476.58	571.84
279.06	399.16	480.01	576.06
279.88	400.12	481.31	570.96
281.34	400.83	479.42	575.16
281.69	401.23	476.98	574.34
280.93	395.16	478.18	574.30
281.66	400.32	476.91	574.44
279.33	398.26	477.81	573.25
279.54	400.10	474.67	572.22

281.47	400.92	475.64	573.88
279.22	400.96	478.37	570.65
283.47	398.73	476.70	577.53
280.65	399.27	475.88	570.59
280.50	399.48	477.14	573.45
286.20	399.77	475.41	569.03
276.90	400.02	476.98	572.46
278.32	398.06	472.59	572.46
276.83	394.62	476.12	571.76
277.48	399.27	472.41	569.77
277.15	396.19	475.43	570.47
279.73	398.09	472.36	569.85
281.40	397.14	475.79	569.10
281.32	396.78	470.41	567.83
278.16	395.16	473.82	570.16
278.99	397.33	470.71	567.99
274.94	398.22	472.07	571.84
277.49	393.84	471.96	568.39
277.79	392.49	469.86	564.52
274.84	397.22	469.41	568.28
277.61	398.45	473.23	569.32
280.91	395.59	474.67	570.81
276.49	394.10	471.36	567.22

276.55	396.62	468.04	566.26
277.22	395.38	472.36	569.63
278.03	394.89	470.95	565.27
280.42	395.74	469.27	566.11
273.97	394.74	472.65	567.07
277.56	395.62	470.66	565.49
281.73	393.93	472.13	566.61
278.91	396.77	471.31	565.87
277.72	394.48	472.90	567.92
275.39	395.35	469.14	563.19
277.56	393.59	472.08	568.34
278.96	397.95	469.69	565.30
277.44	392.84	472.73	567.07
276.52	397.05	468.76	564.14
277.10	394.97	470.69	565.57
278.61	395.19	469.50	565.94
277.27	396.29	470.24	566.04
274.55	392.71	471.03	565.37
275.47	396.23	467.08	563.27
275.33	392.50	470.16	568.57
276.03	392.13	467.85	562.60
277.11	391.16	469.42	564.43
278.63	393.41	467.25	565.38

274.41	394.98	468.64	565.06
277.22	391.30	470.96	565.68
274.54	395.34	466.25	565.06
277.42	392.98	470.79	565.58
274.24	391.86	469.26	562.16
274.61	392.42	469.54	565.20
275.24	393.68	466.17	562.17
276.75	392.22	470.36	565.07
275.11	391.32	466.17	562.50
276.10	392.17	466.08	562.11
273.04	395.50	470.36	565.13
275.41	390.52	465.02	562.10
273.09	392.89	467.99	560.70
277.59	390.77	465.84	562.95
273.16	392.53	468.05	562.07
276.00	390.13	465.69	561.66
275.22	389.25	464.86	561.80
275.19	391.19	466.86	559.71
275.08	389.88	464.42	561.51
275.31	391.31	467.77	560.38
279.69	393.95	469.57	561.99
274.45	390.59	467.14	561.60
276.24	393.13	467.98	561.47

275.46	392.47	465.51	562.08
273.63	391.31	464.76	558.82

APPENDIX E: CALCULATED PERCENT SIGNAL LOSS FOR FOUR LDs IN Table 2

Table 36: Calculated percent signal loss for LD exposed to 51.6 cGy and measured 100 times.

Time in Beam (seconds)	**Calculated Dose (cGy)**		
8	51.6		
Initial Measurement (counts)	**Next Measurement (counts)**	**Signal Loss (counts)**	**Signal Loss (percent)**
85209	84573	636	0.75
84573	80651	3922	4.64
80651	81387	-736	-0.91
81387	81260	127	0.16
81260	80298	962	1.18
80298	80034	264	0.33
80034	80147	-113	-0.14
80147	83790	-3643	-4.55
83790	79592	4198	5.01
79592	82450	-2858	-3.59
82450	80997	1453	1.76
80997	77832	3165	3.91
77832	79504	-1672	-2.15
79504	80195	-691	-0.87
80195	79564	631	0.79
79564	79102	462	0.58
79102	78986	116	0.15

78986	80814	-1828	-2.31
80814	78277	2537	3.14
78277	77517	760	0.97
77517	77876	-359	-0.46
77876	78332	-456	-0.59
78332	79155	-823	-1.05
79155	79350	-195	-0.25
79350	78923	427	0.54
78923	79330	-407	-0.52
79330	78025	1305	1.65
78025	78141	-116	-0.15
78141	79228	-1087	-1.39
79228	77964	1264	1.60
77964	80353	-2389	-3.06
80353	78764	1589	1.98
78764	78678	86	0.11
78678	81911	-3233	-4.11
81911	76674	5237	6.39
76674	77461	-787	-1.03
77461	76634	827	1.07
76634	76995	-361	-0.47
76995	76812	183	0.24
76812	78247	-1435	-1.87

78247	79188	-941	-1.20
79188	79140	48	0.06
79140	77374	1766	2.23
77374	77837	-463	-0.60
77837	75592	2245	2.88
75592	77000	-1408	-1.86
77000	77170	-170	-0.22
77170	75539	1631	2.11
75539	77070	-1531	-2.03
77070	78910	-1840	-2.39
78910	76449	2461	3.12
76449	76482	-33	-0.04
76482	76849	-367	-0.48
76849	77303	-454	-0.59
77303	78633	-1330	-1.72
78633	75057	3576	4.55
75057	77041	-1984	-2.64
77041	79374	-2333	-3.03
79374	77793	1581	1.99
77793	77128	665	0.85
77128	75839	1289	1.67
75839	77039	-1200	-1.58
77039	77819	-780	-1.01

77819	76975	844	1.08
76975	76462	513	0.67
76462	76784	-322	-0.42
76784	77626	-842	-1.10
77626	76878	748	0.96
76878	75378	1500	1.95
75378	75886	-508	-0.67
75886	75808	78	0.10
75808	76190	-382	-0.50
76190	76790	-600	-0.79
76790	77636	-846	-1.10
77636	75301	2335	3.01
75301	76851	-1550	-2.06
76851	75370	1481	1.93
75370	76963	-1593	-2.11
76963	75210	1753	2.28
75210	75409	-199	-0.26
75409	75757	-348	-0.46
75757	76589	-832	-1.10
76589	75684	905	1.18
75684	76231	-547	-0.72
76231	74550	1681	2.21
74550	75848	-1298	-1.74

75848	74579	1269	1.67
74579	77056	-2477	-3.32
77056	74619	2437	3.16
74619	76178	-1559	-2.09
76178	75748	430	0.56
75748	75732	16	0.02
75732	75669	63	0.08
75669	75796	-127	-0.17
75796	78224	-2428	-3.20
78224	75322	2902	3.71
75322	76309	-987	-1.31
76309	75876	433	0.57
75876	74875	1001	1.32
			Average
			0.11

Table 37: Calculated percent signal loss for LD exposed to 103.2 cGy and measured 100 times.

Time in Beam (seconds)	**Calculated Dose (cGy)**		
16	103.2		
Initial Measurement (counts)	**Next Measurement (counts)**	**Signal Loss (counts)**	**Signal Loss (percent)**
168909	166145	2764	1.64
166145	165595	550	0.33
165595	165491	104	0.06
165491	164489	1002	0.61
164489	167278	-2789	-1.70
167278	164381	2897	1.73
164381	164723	-342	-0.21
164723	164978	-255	-0.15
164978	163608	1370	0.83
163608	158737	4871	2.98
158737	164543	-5806	-3.66
164543	162083	2460	1.50
162083	159979	2104	1.30
159979	161945	-1966	-1.23
161945	161461	484	0.30
161461	158840	2621	1.62
158840	160239	-1399	-0.88
160239	163061	-2822	-1.76

163061	158555	4506	2.76
158555	161046	-2491	-1.57
161046	159327	1719	1.07
159327	160093	-766	-0.48
160093	160663	-570	-0.36
160663	160985	-322	-0.20
160985	156148	4837	3.00
156148	160260	-4112	-2.63
160260	158614	1646	1.03
158614	160081	-1467	-0.92
160081	160737	-656	-0.41
160737	160769	-32	-0.02
160769	158987	1782	1.11
158987	159416	-429	-0.27
159416	159584	-168	-0.11
159584	159813	-229	-0.14
159813	160014	-201	-0.13
160014	158454	1560	0.97
158454	155726	2728	1.72
155726	159418	-3692	-2.37
159418	156969	2449	1.54
156969	158477	-1508	-0.96
158477	157721	756	0.48

157721	157434	287	0.18
157434	156149	1285	0.82
156149	157869	-1720	-1.10
157869	158578	-709	-0.45
158578	155112	3466	2.19
155112	154049	1063	0.69
154049	157781	-3732	-2.42
157781	158762	-981	-0.62
158762	156492	2270	1.43
156492	155313	1179	0.75
155313	157308	-1995	-1.28
157308	156327	981	0.62
156327	155940	387	0.25
155940	156607	-667	-0.43
156607	155818	789	0.50
155818	156516	-698	-0.45
156516	155177	1339	0.86
155177	157428	-2251	-1.45
157428	155617	1811	1.15
155617	156299	-682	-0.44
156299	154911	1388	0.89
154911	158361	-3450	-2.23
158361	154325	4036	2.55

154325	157652	-3327	-2.16
157652	155999	1653	1.05
155999	156179	-180	-0.12
156179	157046	-867	-0.56
157046	154222	2824	1.80
154222	156995	-2773	-1.80
156995	154053	2942	1.87
154053	153769	284	0.18
153769	153004	765	0.50
153004	154771	-1767	-1.15
154771	156012	-1241	-0.80
156012	153115	2897	1.86
153115	156294	-3179	-2.08
156294	154437	1857	1.19
154437	153551	886	0.57
153551	153993	-442	-0.29
153993	154986	-993	-0.64
154986	153838	1148	0.74
153838	153134	704	0.46
153134	153795	-661	-0.43
153795	156423	-2628	-1.71
156423	152504	3919	2.51
152504	154364	-1860	-1.22

154364	152703	1661	1.08
152703	154076	-1373	-0.90
154076	152201	1875	1.22
152201	151518	683	0.45
151518	153032	-1514	-1.00
153032	152005	1027	0.67
152005	153120	-1115	-0.73
153120	155195	-2075	-1.36
155195	152564	2631	1.70
152564	154551	-1987	-1.30
154551	154032	519	0.34
154032	153124	908	0.59
			Average
			0.09

Table 38: Calculated percent signal loss for LD exposed to 148.35 cGy and measured 99 times.

Time in Beam (seconds)	**Calculated Dose (cGy)**		
23	148.35		
Initial Measurement (counts)	**Next Measurement (counts)**	**Signal Loss (counts)**	**Signal Loss (percent)**
243639	237526	6113	2.51
237526	237752	-226	-0.10
237752	234324	3428	1.44
234324	232331	1993	0.85
232331	234443	-2112	-0.91
234443	235165	-722	-0.31
235165	233479	1686	0.72
233479	234157	-678	-0.29
234157	231371	2786	1.19
231371	228367	3004	1.30
228367	231313	-2946	-1.29
231313	232470	-1157	-0.50
232470	225881	6589	2.83
225881	230299	-4418	-1.96
230299	230857	-558	-0.24
230857	229292	1565	0.68
229292	229271	21	0.01
229271	227364	1907	0.83

227364	227131	233	0.10
227131	230411	-3280	-1.44
230411	231660	-1249	-0.54
231660	229843	1817	0.78
229843	227512	2331	1.01
227512	228659	-1147	-0.50
228659	227442	1217	0.53
227442	228302	-860	-0.38
228302	225308	2994	1.31
225308	226236	-928	-0.41
226236	228835	-2599	-1.15
228835	227239	1596	0.70
227239	226465	774	0.34
226465	227666	-1201	-0.53
227666	226010	1656	0.73
226010	227514	-1504	-0.67
227514	223341	4173	1.83
223341	226686	-3345	-1.50
226686	223172	3514	1.55
223172	226036	-2864	-1.28
226036	223126	2910	1.29
223126	226376	-3250	-1.46
226376	221289	5087	2.25

221289	224507	-3218	-1.45
224507	221565	2942	1.31
221565	222848	-1283	-0.58
222848	222743	105	0.05
222743	220764	1979	0.89
220764	220343	421	0.19
220343	223948	-3605	-1.64
223948	225309	-1361	-0.61
225309	222184	3125	1.39
222184	219057	3127	1.41
219057	223122	-4065	-1.86
223122	221798	1324	0.59
221798	220212	1586	0.72
220212	223400	-3188	-1.45
223400	221518	1882	0.84
221518	222909	-1391	-0.63
222909	222132	777	0.35
222132	223632	-1500	-0.68
223632	220097	3535	1.58
220097	222858	-2761	-1.25
222858	220604	2254	1.01
220604	223478	-2874	-1.30
223478	219740	3738	1.67

219740	221552	-1812	-0.82
221552	220430	1122	0.51
220430	221128	-698	-0.32
221128	221869	-741	-0.34
221869	218160	3709	1.67
218160	221046	-2886	-1.32
221046	218885	2161	0.98
218885	220354	-1469	-0.67
220354	218320	2034	0.92
218320	219626	-1306	-0.60
219626	221806	-2180	-0.99
221806	217390	4416	1.99
217390	221645	-4255	-1.96
221645	220206	1439	0.65
220206	220465	-259	-0.12
220465	217314	3151	1.43
217314	221239	-3925	-1.81
221239	217311	3928	1.78
217311	217234	77	0.04
217234	221243	-4009	-1.85
221243	216242	5001	2.26
216242	219014	-2772	-1.28
219014	217011	2003	0.91

217011	219075	-2064	-0.95
219075	216864	2211	1.01
216864	216095	769	0.35
216095	217956	-1861	-0.86
217956	215687	2269	1.04
215687	218813	-3126	-1.45
218813	220493	-1680	-0.77
220493	218223	2270	1.03
218223	219007	-784	-0.36
219007	216701	2306	1.05
216701	216000	701	0.32
			Average
			0.12

Table 39: Calculated percent signal loss for LD exposed to 199.95 cGy and measured 99 times.

Time in Beam (seconds)	**Calculated Dose (cGy)**		
31	199.95		
Initial Measurement (counts)	**Next Measurement (counts)**	**Signal Loss (counts)**	**Signal Loss (percent)**
358843	348650	10193	2.84
348650	347722	928	0.27
347722	343315	4407	1.27
343315	338929	4386	1.28
338929	337707	1222	0.36
337707	337963	-256	-0.08
337963	337326	637	0.19
337326	334529	2797	0.83
334529	334525	4	0.00
334525	330146	4379	1.31
330146	332386	-2240	-0.68
332386	333601	-1215	-0.37
333601	329657	3944	1.18
329657	331908	-2251	-0.68
331908	332160	-252	-0.08
332160	331767	393	0.12
331767	330265	1502	0.45
330265	330902	-637	-0.19

330902	326999	3903	1.18
326999	331849	-4850	-1.48
331849	325998	5851	1.76
325998	330805	-4807	-1.47
330805	329871	934	0.28
329871	329817	54	0.02
329817	329980	-163	-0.05
329980	328616	1364	0.41
328616	327435	1181	0.36
327435	329333	-1898	-0.58
329333	325646	3687	1.12
325646	333538	-7892	-2.42
333538	325568	7970	2.39
325568	328840	-3272	-1.01
328840	323796	5044	1.53
323796	327712	-3916	-1.21
327712	327711	1	0.00
327711	326911	800	0.24
326911	324637	2274	0.70
324637	325439	-802	-0.25
325439	324726	713	0.22
324726	323871	855	0.26
323871	322432	1439	0.44

322432	325078	-2646	-0.82
325078	322615	2463	0.76
322615	326999	-4384	-1.36
326999	323064	3935	1.20
323064	318688	4376	1.35
318688	322946	-4258	-1.34
322946	324122	-1176	-0.36
324122	325828	-1706	-0.53
325828	321736	4092	1.26
321736	320647	1089	0.34
320647	324484	-3837	-1.20
324484	319525	4959	1.53
319525	320479	-954	-0.30
320479	321565	-1086	-0.34
321565	319782	1783	0.55
319782	321050	-1268	-0.40
321050	320209	841	0.26
320209	322537	-2328	-0.73
322537	317186	5351	1.66
317186	323006	-5820	-1.83
323006	319559	3447	1.07
319559	321570	-2011	-0.63
321570	318253	3317	1.03

318253	319864	-1611	-0.51
319864	320284	-420	-0.13
320284	320397	-113	-0.04
320397	319647	750	0.23
319647	317276	2371	0.74
317276	323276	-6000	-1.89
323276	316524	6752	2.09
316524	318580	-2056	-0.65
318580	319659	-1079	-0.34
319659	319288	371	0.12
319288	319992	-704	-0.22
319992	319290	702	0.22
319290	319881	-591	-0.19
319881	316028	3853	1.20
316028	319450	-3422	-1.08
319450	316031	3419	1.07
316031	319302	-3271	-1.04
319302	316406	2896	0.91
316406	315970	436	0.14
315970	319370	-3400	-1.08
319370	315954	3416	1.07
315954	314383	1571	0.50
314383	316918	-2535	-0.81

316918	315922	996	0.31
315922	315466	456	0.14
315466	315623	-157	-0.05
315623	313273	2350	0.74
313273	315297	-2024	-0.65
315297	314021	1276	0.40
314021	315833	-1812	-0.58
315833	315396	437	0.14
315396	315253	143	0.05
315253	315933	-680	-0.22
315933	312284	3649	1.15
			Average
			0.14

APPENDIX F: MEASUREMENT DATA FOR **Error! Reference source not found.** AND F IGURE 11

Table 40: Measurement data for the number of counts measured by the LANDAUER microSTAR when reading each of the four FD dosimeters, each exposed to 51.6, 103.2, 148.35, and 199.95 cGy using a 40 × 40 mm, 225 kV, 13 mA x-ray beam from a small animal irradiator.

Time in Beam (seconds)			
8	16	23	31
Calculated Dose (cGy)			
51.6	103.2	148.35	199.95
Counts			
3105	6500	11147	15252
3011	6446	11327	15256
3120	6438	11130	14908
2924	6344	11616	15189
3052	6313	11114	14994
3031	6455	11138	14905
2981	6307	11079	14647
2896	6199	11134	14817
3037	6273	10759	14748
3000	6344	11019	14620
2927	6111	10920	14779
3015	6169	10578	14959
2995	6193	10837	14605
2883	6238	10827	14696
2853	6104	10899	14558

2906	6178	10897	14396
2888	6375	10783	14361
2902	6267	10700	14337
2881	6221	10684	14425
2911	6211	10617	14167
2903	6134	10568	14251
2814	6177	10498	14216
2964	6194	10485	14234
2853	6127	10359	14081
2922	6147	10358	14094
2840	6053	10454	14040
2805	6034	10480	13890
2823	6092	10367	13917
2887	6006	10223	13859
2785	6000	10232	13712
2808	5934	10257	13922
2767	5955	10161	13755
2791	6019	10151	13758
2768	5982	10069	13714
2756	5782	10059	13641
2790	5825	10179	13643
2726	5883	9955	13620
2773	5892	9827	13457

2767	5951	9944	13486
2826	5896	9922	13369
2788	5881	9838	13407
2747	5774	9863	13449
2702	5876	9951	13424
2777	5822	9840	13478
2736	5967	9798	13308
2706	5830	9784	13286
2728	5726	9976	13332
2755	5725	9709	13155
2684	5708	9655	13273
2695	5696	9966	13248
2643	5652	9636	13121
2533	5757	9660	13108
2709	5893	9621	13124
2717	5690	9504	13019
2734	5623	9561	12910
2706	5609	9807	12953
2673	5609	9494	12819
2616	5634	9632	12852
2692	5740	9577	12701
2730	5671	9438	12659
2589	5362	9265	12664

2671	5581	9353	12675
2686	5683	9359	12522
2694	5585	9347	12611
2628	5633	9236	12509
2641	5605	9312	12634
2724	5591	9252	12438
2660	5513	9411	12489
2578	5535	9222	12346
2687	5467	9331	12351
2635	5505	9050	12358
2594	5520	9106	12633
2622	5491	9047	12210
2566	5408	9111	12414
2554	5345	9001	12000
2587	5520	9114	12281
2561	5470	8862	12185
2581	5434	9029	12153
2560	5233	8814	12079
2617	5375	8996	12180
2587	5409	8892	12137
2530	5336	9017	12094
2536	5339	8793	12194
2530	5415	8942	12008

2452	5328	8684	11942
2543	5354	8902	12000
2402	5292	8860	12031
2462	5246	8748	12051
2519	5382	8800	11777
2494	5241	8818	11800
2535	5352	8722	11690
2510	5069	8809	11694
2483	5085	8596	11772
2482	5168	8645	11561
2503	5286	8621	11714
2569	5160	8401	11604
2452	5274	8563	11457
2557	5141	8662	11588
2516	5256	8383	11394
2430	5065	8491	11490
Error (counts)			
55.72	80.62	105.58	123.50
54.87	80.29	106.43	123.52
55.86	80.24	105.50	122.10
54.07	79.65	107.78	123.24
55.24	79.45	105.42	122.45
55.05	80.34	105.54	122.09

54.60	79.42	105.26	121.02
53.81	78.73	105.52	121.73
55.11	79.20	103.73	121.44
54.77	79.65	104.97	120.91
54.10	78.17	104.50	121.57
54.91	78.54	102.85	122.31
54.73	78.70	104.10	120.85
53.69	78.98	104.05	121.23
53.41	78.13	104.40	120.66
53.91	78.60	104.39	119.98
53.74	79.84	103.84	119.84
53.87	79.16	103.44	119.74
53.67	78.87	103.36	120.10
53.95	78.81	103.04	119.03
53.88	78.32	102.80	119.38
53.05	78.59	102.46	119.23
54.44	78.70	102.40	119.31
53.41	78.28	101.78	118.66
54.06	78.40	101.77	118.72
53.29	77.80	102.24	118.49
52.96	77.68	102.37	117.86
53.13	78.05	101.82	117.97
53.73	77.50	101.11	117.72

52.77	77.46	101.15	117.10
52.99	77.03	101.28	117.99
52.60	77.17	100.80	117.28
52.83	77.58	100.75	117.29
52.61	77.34	100.34	117.11
52.50	76.04	100.29	116.79
52.82	76.32	100.89	116.80
52.21	76.70	99.77	116.70
52.66	76.76	99.13	116.00
52.60	77.14	99.72	116.13
53.16	76.79	99.61	115.62
52.80	76.69	99.19	115.79
52.41	75.99	99.31	115.97
51.98	76.66	99.75	115.86
52.70	76.30	99.20	116.09
52.31	77.25	98.98	115.36
52.02	76.35	98.91	115.26
52.23	75.67	99.88	115.46
52.49	75.66	98.53	114.70
51.81	75.55	98.26	115.21
51.91	75.47	99.83	115.10
51.41	75.18	98.16	114.55
50.33	75.87	98.29	114.49

52.05	76.77	98.09	114.56
52.12	75.43	97.49	114.10
52.29	74.99	97.78	113.62
52.02	74.89	99.03	113.81
51.70	74.89	97.44	113.22
51.15	75.06	98.14	113.37
51.88	75.76	97.86	112.70
52.25	75.31	97.15	112.51
50.88	73.23	96.25	112.53
51.68	74.71	96.71	112.58
51.83	75.39	96.74	111.90
51.90	74.73	96.68	112.30
51.26	75.05	96.10	111.84
51.39	74.87	96.50	112.40
52.19	74.77	96.19	111.53
51.58	74.25	97.01	111.75
50.77	74.40	96.03	111.11
51.84	73.94	96.60	111.14
51.33	74.20	95.13	111.17
50.93	74.30	95.43	112.40
51.21	74.10	95.12	110.50
50.66	73.54	95.45	111.42
50.54	73.11	94.87	109.54

50.86	74.30	95.47	110.82
50.61	73.96	94.14	110.39
50.80	73.72	95.02	110.24
50.60	72.34	93.88	109.90
51.16	73.31	94.85	110.36
50.86	73.55	94.30	110.17
50.30	73.05	94.96	109.97
50.36	73.07	93.77	110.43
50.30	73.59	94.56	109.58
49.52	72.99	93.19	109.28
50.43	73.17	94.35	109.54
49.01	72.75	94.13	109.69
49.62	72.43	93.53	109.78
50.19	73.36	93.81	108.52
49.94	72.39	93.90	108.63
50.35	73.16	93.39	108.12
50.10	71.20	93.86	108.14
49.83	71.31	92.71	108.50
49.82	71.89	92.98	107.52
50.03	72.70	92.85	108.23
50.69	71.83	91.66	107.72
49.52	72.62	92.54	107.04
50.57	71.70	93.07	107.65

50.16	72.50	91.56	106.74
49.30	71.17	92.15	107.19

APPENDIX G: CALCULATED PERCENT SIGNAL LOSS FOR FOUR FDs IN Table 4

Table 41: Calculated percent signal loss for FD exposed to 51.6 cGy and measured 100 times.

Time in Beam (seconds)	**Calculated Dose (cGy)**		
8	51.6		
Initial Measurement (counts)	**Next Measurement (counts)**	**Signal Loss (counts)**	**Signal Loss (percent)**
3105	3011	94	3.03
3011	3120	-109	-3.62
3120	2924	196	6.28
2924	3052	-128	-4.38
3052	3031	21	0.69
3031	2981	50	1.65
2981	2896	85	2.85
2896	3037	-141	-4.87
3037	3000	37	1.22
3000	2927	73	2.43
2927	3015	-88	-3.01
3015	2995	20	0.66
2995	2883	112	3.74
2883	2853	30	1.04
2853	2906	-53	-1.86
2906	2888	18	0.62
2888	2902	-14	-0.48

2902	2881	21	0.72
2881	2911	-30	-1.04
2911	2903	8	0.27
2903	2814	89	3.07
2814	2964	-150	-5.33
2964	2853	111	3.74
2853	2922	-69	-2.42
2922	2840	82	2.81
2840	2805	35	1.23
2805	2823	-18	-0.64
2823	2887	-64	-2.27
2887	2785	102	3.53
2785	2808	-23	-0.83
2808	2767	41	1.46
2767	2791	-24	-0.87
2791	2768	23	0.82
2768	2756	12	0.43
2756	2790	-34	-1.23
2790	2726	64	2.29
2726	2773	-47	-1.72
2773	2767	6	0.22
2767	2826	-59	-2.13
2826	2788	38	1.34

2788	2747	41	1.47
2747	2702	45	1.64
2702	2777	-75	-2.78
2777	2736	41	1.48
2736	2706	30	1.10
2706	2728	-22	-0.81
2728	2755	-27	-0.99
2755	2684	71	2.58
2684	2695	-11	-0.41
2695	2643	52	1.93
2643	2533	110	4.16
2533	2709	-176	-6.95
2709	2717	-8	-0.30
2717	2734	-17	-0.63
2734	2706	28	1.02
2706	2673	33	1.22
2673	2616	57	2.13
2616	2692	-76	-2.91
2692	2730	-38	-1.41
2730	2589	141	5.16
2589	2671	-82	-3.17
2671	2686	-15	-0.56
2686	2694	-8	-0.30

2694	2628	66	2.45
2628	2641	-13	-0.49
2641	2724	-83	-3.14
2724	2660	64	2.35
2660	2578	82	3.08
2578	2687	-109	-4.23
2687	2635	52	1.94
2635	2594	41	1.56
2594	2622	-28	-1.08
2622	2566	56	2.14
2566	2554	12	0.47
2554	2587	-33	-1.29
2587	2561	26	1.01
2561	2581	-20	-0.78
2581	2560	21	0.81
2560	2617	-57	-2.23
2617	2587	30	1.15
2587	2530	57	2.20
2530	2536	-6	-0.24
2536	2530	6	0.24
2530	2452	78	3.08
2452	2543	-91	-3.71
2543	2402	141	5.54

2402	2462	-60	-2.50
2462	2519	-57	-2.32
2519	2494	25	0.99
2494	2535	-41	-1.64
2535	2510	25	0.99
2510	2483	27	1.08
2483	2482	1	0.04
2482	2503	-21	-0.85
2503	2569	-66	-2.64
2569	2452	117	4.55
2452	2557	-105	-4.28
2557	2516	41	1.60
2516	2430	86	3.42
			Average
			0.22

Table 42: Calculated percent signal loss for FD exposed to 103.2 cGy and measured 100 times.

Time in Beam (seconds)	**Calculated Dose (cGy)**		
16	103.2		
Initial Measurement (counts)	**Next Measurement (counts)**	**Signal Loss (counts)**	**Signal Loss (percent)**
6500	6446	54	0.83
6446	6438	8	0.12
6438	6344	94	1.46
6344	6313	31	0.49
6313	6455	-142	-2.25
6455	6307	148	2.29
6307	6199	108	1.71
6199	6273	-74	-1.19
6273	6344	-71	-1.13
6344	6111	233	3.67
6111	6169	-58	-0.95
6169	6193	-24	-0.39
6193	6238	-45	-0.73
6238	6104	134	2.15
6104	6178	-74	-1.21
6178	6375	-197	-3.19
6375	6267	108	1.69
6267	6221	46	0.73

6221	6211	10	0.16
6211	6134	77	1.24
6134	6177	-43	-0.70
6177	6194	-17	-0.28
6194	6127	67	1.08
6127	6147	-20	-0.33
6147	6053	94	1.53
6053	6034	19	0.31
6034	6092	-58	-0.96
6092	6006	86	1.41
6006	6000	6	0.10
6000	5934	66	1.10
5934	5955	-21	-0.35
5955	6019	-64	-1.07
6019	5982	37	0.61
5982	5782	200	3.34
5782	5825	-43	-0.74
5825	5883	-58	-1.00
5883	5892	-9	-0.15
5892	5951	-59	-1.00
5951	5896	55	0.92
5896	5881	15	0.25
5881	5774	107	1.82

5774	5876	-102	-1.77
5876	5822	54	0.92
5822	5967	-145	-2.49
5967	5830	137	2.30
5830	5726	104	1.78
5726	5725	1	0.02
5725	5708	17	0.30
5708	5696	12	0.21
5696	5652	44	0.77
5652	5757	-105	-1.86
5757	5893	-136	-2.36
5893	5690	203	3.44
5690	5623	67	1.18
5623	5609	14	0.25
5609	5609	0	0.00
5609	5634	-25	-0.45
5634	5740	-106	-1.88
5740	5671	69	1.20
5671	5362	309	5.45
5362	5581	-219	-4.08
5581	5683	-102	-1.83
5683	5585	98	1.72
5585	5633	-48	-0.86

5633	5605	28	0.50
5605	5591	14	0.25
5591	5513	78	1.40
5513	5535	-22	-0.40
5535	5467	68	1.23
5467	5505	-38	-0.70
5505	5520	-15	-0.27
5520	5491	29	0.53
5491	5408	83	1.51
5408	5345	63	1.16
5345	5520	-175	-3.27
5520	5470	50	0.91
5470	5434	36	0.66
5434	5233	201	3.70
5233	5375	-142	-2.71
5375	5409	-34	-0.63
5409	5336	73	1.35
5336	5339	-3	-0.06
5339	5415	-76	-1.42
5415	5328	87	1.61
5328	5354	-26	-0.49
5354	5292	62	1.16
5292	5246	46	0.87

5246	5382	-136	-2.59
5382	5241	141	2.62
5241	5352	-111	-2.12
5352	5069	283	5.29
5069	5085	-16	-0.32
5085	5168	-83	-1.63
5168	5286	-118	-2.28
5286	5160	126	2.38
5160	5274	-114	-2.21
5274	5141	133	2.52
5141	5256	-115	-2.24
5256	5065	191	3.63
			Average
			0.24

Table 43: Calculated percent signal loss for FD exposed to 148.35 cGy and measured 100 times.

Time in Beam (seconds)	**Calculated Dose (cGy)**		
23	148.35		
Initial Measurement (counts)	**Next Measurement (counts)**	**Signal Loss (counts)**	**Signal Loss (percent)**
11147	11327	-180	-1.61
11327	11130	197	1.74
11130	11616	-486	-4.37
11616	11114	502	4.32
11114	11138	-24	-0.22
11138	11079	59	0.53
11079	11134	-55	-0.50
11134	10759	375	3.37
10759	11019	-260	-2.42
11019	10920	99	0.90
10920	10578	342	3.13
10578	10837	-259	-2.45
10837	10827	10	0.09
10827	10899	-72	-0.67
10899	10897	2	0.02
10897	10783	114	1.05
10783	10700	83	0.77
10700	10684	16	0.15

10684	10617	67	0.63
10617	10568	49	0.46
10568	10498	70	0.66
10498	10485	13	0.12
10485	10359	126	1.20
10359	10358	1	0.01
10358	10454	-96	-0.93
10454	10480	-26	-0.25
10480	10367	113	1.08
10367	10223	144	1.39
10223	10232	-9	-0.09
10232	10257	-25	-0.24
10257	10161	96	0.94
10161	10151	10	0.10
10151	10069	82	0.81
10069	10059	10	0.10
10059	10179	-120	-1.19
10179	9955	224	2.20
9955	9827	128	1.29
9827	9944	-117	-1.19
9944	9922	22	0.22
9922	9838	84	0.85
9838	9863	-25	-0.25

9863	9951	-88	-0.89
9951	9840	111	1.12
9840	9798	42	0.43
9798	9784	14	0.14
9784	9976	-192	-1.96
9976	9709	267	2.68
9709	9655	54	0.56
9655	9966	-311	-3.22
9966	9636	330	3.31
9636	9660	-24	-0.25
9660	9621	39	0.40
9621	9504	117	1.22
9504	9561	-57	-0.60
9561	9807	-246	-2.57
9807	9494	313	3.19
9494	9632	-138	-1.45
9632	9577	55	0.57
9577	9438	139	1.45
9438	9265	173	1.83
9265	9353	-88	-0.95
9353	9359	-6	-0.06
9359	9347	12	0.13
9347	9236	111	1.19

9236	9312	-76	-0.82
9312	9252	60	0.64
9252	9411	-159	-1.72
9411	9222	189	2.01
9222	9331	-109	-1.18
9331	9050	281	3.01
9050	9106	-56	-0.62
9106	9047	59	0.65
9047	9111	-64	-0.71
9111	9001	110	1.21
9001	9114	-113	-1.26
9114	8862	252	2.76
8862	9029	-167	-1.88
9029	8814	215	2.38
8814	8996	-182	-2.06
8996	8892	104	1.16
8892	9017	-125	-1.41
9017	8793	224	2.48
8793	8942	-149	-1.69
8942	8684	258	2.89
8684	8902	-218	-2.51
8902	8860	42	0.47
8860	8748	112	1.26

8748	8800	-52	-0.59
8800	8818	-18	-0.20
8818	8722	96	1.09
8722	8809	-87	-1.00
8809	8596	213	2.42
8596	8645	-49	-0.57
8645	8621	24	0.28
8621	8401	220	2.55
8401	8563	-162	-1.93
8563	8662	-99	-1.16
8662	8383	279	3.22
8383	8491	-108	-1.29
8491			
			Average
			0.26

Table 44: Calculated percent signal loss for FD exposed to 199.95 cGy and measured 100 times.

Time in Beam (seconds)	**Calculated Dose (cGy)**		
31	199.95		
Initial Measurement (counts)	**Next Measurement (counts)**	**Signal Loss (counts)**	**Signal Loss (percent)**
15252	15256	-4	-0.03
15256	14908	348	2.28
14908	15189	-281	-1.88
15189	14994	195	1.28
14994	14905	89	0.59
14905	14647	258	1.73
14647	14817	-170	-1.16
14817	14748	69	0.47
14748	14620	128	0.87
14620	14779	-159	-1.09
14779	14959	-180	-1.22
14959	14605	354	2.37
14605	14696	-91	-0.62
14696	14558	138	0.94
14558	14396	162	1.11
14396	14361	35	0.24
14361	14337	24	0.17
14337	14425	-88	-0.61

14425	14167	258	1.79
14167	14251	-84	-0.59
14251	14216	35	0.25
14216	14234	-18	-0.13
14234	14081	153	1.07
14081	14094	-13	-0.09
14094	14040	54	0.38
14040	13890	150	1.07
13890	13917	-27	-0.19
13917	13859	58	0.42
13859	13712	147	1.06
13712	13922	-210	-1.53
13922	13755	167	1.20
13755	13758	-3	-0.02
13758	13714	44	0.32
13714	13641	73	0.53
13641	13643	-2	-0.01
13643	13620	23	0.17
13620	13457	163	1.20
13457	13486	-29	-0.22
13486	13369	117	0.87
13369	13407	-38	-0.28
13407	13449	-42	-0.31

13449	13424	25	0.19
13424	13478	-54	-0.40
13478	13308	170	1.26
13308	13286	22	0.17
13286	13332	-46	-0.35
13332	13155	177	1.33
13155	13273	-118	-0.90
13273	13248	25	0.19
13248	13121	127	0.96
13121	13108	13	0.10
13108	13124	-16	-0.12
13124	13019	105	0.80
13019	12910	109	0.84
12910	12953	-43	-0.33
12953	12819	134	1.03
12819	12852	-33	-0.26
12852	12701	151	1.17
12701	12659	42	0.33
12659	12664	-5	-0.04
12664	12675	-11	-0.09
12675	12522	153	1.21
12522	12611	-89	-0.71
12611	12509	102	0.81

12509	12634	-125	-1.00
12634	12438	196	1.55
12438	12489	-51	-0.41
12489	12346	143	1.15
12346	12351	-5	-0.04
12351	12358	-7	-0.06
12358	12633	-275	-2.23
12633	12210	423	3.35
12210	12414	-204	-1.67
12414	12000	414	3.33
12000	12281	-281	-2.34
12281	12185	96	0.78
12185	12153	32	0.26
12153	12079	74	0.61
12079	12180	-101	-0.84
12180	12137	43	0.35
12137	12094	43	0.35
12094	12194	-100	-0.83
12194	12008	186	1.53
12008	11942	66	0.55
11942	12000	-58	-0.49
12000	12031	-31	-0.26
12031	12051	-20	-0.17

12051	11777	274	2.27
11777	11800	-23	-0.20
11800	11690	110	0.93
11690	11694	-4	-0.03
11694	11772	-78	-0.67
11772	11561	211	1.79
11561	11714	-153	-1.32
11714	11604	110	0.94
11604	11457	147	1.27
11457	11588	-131	-1.14
11588	11394	194	1.67
11394	11490	-96	-0.84
			Average
			0.28

APPENDIX H: MEASUREMENT DATA FOR Figure 12

Table 45: Measurement data for the number of counts measured by the LANDAUER microSTAR when reading 8 LD dosimeters, each exposed to 303.15, 399.9, 503.1, 599.85, 703.05, 799.8, 903, and 999.75 cGy using a 40 × 40 mm, 225 kV, 13 mA x-ray beam from a small animal irradiator.

Time in Beam (seconds)							
47	62	78	93	109	124	140	155
Calculated Dose (cGy)							
303.15	399.9	503.1	599.85	703.05	799.8	903	999.75
Counts							
448622	606549	832485	989419	1011824	1224221	1443750	1702975
455220	607351	824913	967320	1022395	1203794	1425082	1693766
445484	617498	840425	970464	998578	1203627	1418723	1681254
448047	613788	809998	954843	994228	1199787	1408523	1662276
445470	608841	817007	954952	992834	1195256	1414950	1660817
452274	600628	803888	941023	994612	1189919	1409594	1646770
445959	597682	821720	949240	1005687	1192896	1398256	1641606
446364	610525	815645	941065	997298	1181149	1396708	1642981
436602	596924	809848	931107	982626	1175908	1388125	1625085
437717	607143	818213	936088	976436	1180091	1389660	1609955
Average Counts							
446175.9	606692.9	819414.2	953552.1	997651.8	1194664.8	1409337.1	1656748.5
Error of Average Counts							
211.23	246.31	286.25	308.80	315.86	345.64	375.41	407.03

Table 46: Measurement data for the number of counts measured by the LANDAUER microSTAR when reading 8 LD dosimeters, each exposed to 1102.95, 1206.15, 1296.45, 1399.65, 1496.4, 1548, 1599.6, and 1651.2 cGy using a 40 × 40 mm, 225 kV, 13 mA x-ray beam from a small animal irradiator.

Time in Beam (seconds)							
171	187	201	217	232	240	248	256
Calculated Dose (cGy)							
1102.95	1206.15	1296.45	1399.65	1496.4	1548	1599.6	1651.2
Counts							
1647362	1970541	2165550	2345435	2271353	2346712	2468365	2794597
1578540	1979812	2108802	2330848	2231730	2320897	2450856	2670857
1577898	1962248	2093844	2284134	2233100	2319462	2408319	2636589
1552584	1917514	2085774	2248479	2220015	2309293	2395433	2613066
1544787	1959952	2088998	2254261	2231584	2320406	2471720	2593297
1563093	1953422	2080308	2243040	2188772	2275314	2352287	2593697
1558086	1896882	2059919	2218611	2207730	2264175	2374272	2571752
1529223	1916206	2063401	2219874	2213414	2272144	2397757	2580992
1535561	1914259	2090798	2232463	2202378	2273295	2393712	2557548
1528323	1897234	2057413	2200549	2202047	2279152	2362150	2565879
Average Counts							
1561545.7	1936807	2089480.7	2257769.4	2220212.3	2298085	2407487.1	2617827.4
Error of Average Counts							
440.09	457.11	475.16	471.19	479.38	490.66	511.65	440.09

APPENDIX I: MEASUREMENT DATA FOR Figure 13

Table 47: Measurement data for the number of counts measured by the LANDAUER microSTAR when reading 8 FD dosimeters, each exposed to 303.15, 399.9, 503.1, 599.85, 703.05, 799.8, 903, and 999.75 cGy using a 40 × 40 mm, 225 kV, 13 mA x-ray beam from a small animal irradiator.

Time in Beam (seconds)							
47	62	78	93	109	124	140	155
Calculated Dose (cGy)							
303.15	399.9	503.1	599.85	703.05	799.8	903	999.75
Counts							
2144	3234	5545	4593	3108	3773	6780	6905
2191	3291	5571	4570	3063	3692	6579	6764
2158	3274	5530	4580	3086	3660	6640	6754
2166	3226	5574	4471	3090	3727	6647	6661
2076	3246	5466	4514	3086	3694	6720	6725
2122	3253	5542	4512	3000	3627	6532	6599
2207	3229	5518	4502	3020	3718	6545	6581
2152	3153	5375	4395	2941	3610	6473	6543
2106	3228	5366	4433	3004	3611	6540	6616
2112	3212	5399	4454	3086	3644	6601	6515
Average Counts							
2143.4	3234.6	5488.6	4502.4	3048.4	3675.6	6605.7	6666.3
Error of Average Counts							
14.64	17.98	23.43	21.22	17.46	19.17	25.70	25.82

Table 48: Measurement data for the number of counts measured by the LANDAUER microSTAR when reading 8 FD dosimeters, each exposed to 1102.95, 1206.15, 1296.45, 1399.65, 1496.4, 1548, 1599.6, and 1651.2 cGy using a 40 × 40 mm, 225 kV, 13 mA x-ray beam from a small animal irradiator.

Time in Beam (seconds)							
171	187	201	217	232	240	248	256
Calculated Dose (cGy)							
1102.95	1206.15	1296.45	1399.65	1496.4	1548	1599.6	1651.2
Counts							
4724	5627	6046	10165	9666	13265	9759	9159
4828	5621	6003	10048	9929	16414	9762	9182
4814	5648	5891	9824	9812	13741	9767	9161
4634	5619	5877	9888	10055	13674	9851	9208
4621	5524	5866	9955	10044	13688	9782	9215
4727	5452	5883	9927	9784	13820	9651	9148
4846	5477	5909	9939	9778	13849	9671	9134
4820	5585	5879	9886	9703	14134	9635	9125
4622	5551	5943	9815	9690	13713	9667	9098
4578	5499	5764	9582	9904	16633	9515	9000
Average Counts							
4721.4	5560.3	5906.1	9902.9	9836.5	14293.1	9706	9143
Error of Average Counts							
21.73	23.58	24.30	31.47	31.36	37.81	31.15	30.24

APPENDIX J: MEASUREMENT DATA FOR Figure 14, Figure 15, Figure 16, AND Figure 17

Table 49: Measurement data for the average counts of 4 LDs which were incrementally exposed to doses of 6.45 cGy for total doses of 0, 6.45, 12.9, 19.35, 25.8, 32.25, 38.7, 45.15, and 51.6 cGy by placing the dots in a 40 × 40 mm, 225 kV, and 13 mA x-ray beam in the small animal irradiator for 1 second and then read with the microSTAR reader 5 times.

Time in Beam (seconds)	**Calculated Dose (cGy)**		
0	0		
LD1 (counts)	**LD 2 (counts)**	**LD 3 (counts)**	**LD 4 (counts)**
13	14	12	13
14	12	17	13
13	13	14	16
19	12	15	12
12	15	14	12
	Average (counts)		
14.2	13.2	14.4	13.2
Time in Beam (seconds)	**Calculated Dose (cGy)**		
1	6.45		
LD1 (counts)	**LD 2 (counts)**	**LD 3 (counts)**	**LD 4 (counts)**
35945	36885	36699	38474
33853	35612	35084	35360
30916	31068	31335	32017
29734	29801	30223	30408
28503	28480	28723	29028

	Average (counts)		
31790.2	32369.2	32412.8	33057.4
Time in Beam (seconds)	**Calculated Dose (cGy)**		
2	12.9		
LD1 (counts)	**LD 2 (counts)**	**LD 3 (counts)**	**LD 4 (counts)**
34013	63382	64281	65891
62670	61375	61838	61362
55375	55803	57096	57256
56029	54586	55573	57131
53751	52509	54485	55503
	Average (counts)		
52367.6	57531	58654.6	59428.6
Time in Beam (seconds)	**Calculated Dose (cGy)**		
3	19.35		
LD1 (counts)	**LD 2 (counts)**	**LD 3 (counts)**	**LD 4 (counts)**
92429	90818	92783	94839
88996	88227	89469	90219
86280	85743	88068	88176
82672	82808	83821	84278
84871	81738	83520	82798
Average			

87049.6	85866.8	87532.2	88062
Time in Beam (seconds)	**Calculated Dose (cGy)**		
4	25.8		
LD1 (counts)	**LD 2 (counts)**	**LD 3 (counts)**	**LD 4 (counts)**
108196	107759	111152	111934
106694	108296	109180	111668
109116	106884	107698	110392
105516	105263	105753	109200
	Average (counts)		
107380.5	107050.5	108445.8	110798.5
Time in Beam (seconds)	**Calculated Dose (cGy)**		
5	32.25		
LD1 (counts)	**LD 2 (counts)**	**LD 3 (counts)**	**LD 4 (counts)**
136820	138615	140119	146140
	130512	128979	136736
121627	124660	124568	129664
127221	126625	125684	132337
127199	125489	127691	132321
130598	124918	129029	131596
	Average (counts)		
128693	128469.8	129345	134799

Time in Beam (seconds)	Calculated Dose (cGy)		
6	38.7		
LD1 (counts)	**LD 2 (counts)**	**LD 3 (counts)**	**LD 4 (counts)**
165365	166960		
161899	163443		166891
141264	147710	147267	153740
141376	148491	147641	155957
142460	148142	150585	154745
142924	147971	149397	155897
146800	149472	149280	155544
	Average (counts)		
148869.7	153169.9	148834	157129
Time in Beam (seconds)	**Calculated Dose (cGy)**		
7	45.15		
LD1 (counts)	**LD 2 (counts)**	**LD 3 (counts)**	**LD 4 (counts)**
174121	168082	172949	176760
171028	167209	169776	177500
169771	167001	169087	174517
165261	165610	170826	175081
164784	163871	168628	171826
	Average (counts)		

168993	166354.6	170253.2	175136.8
Time in Beam (seconds)	**Calculated Dose (cGy)**		
8	51.6		
LD1 (counts)	**LD 2 (counts)**	**LD 3 (counts)**	**LD 4 (counts)**
186041	193420	187562	195892
186388	191156	188498	192534
187981	190681	186751	190880
180962	187710	184575	190981
181270	187618	183108	190264
Average (counts)			
184528.4	190117	186098.8	192110.2

Table 50: Error of Measurement data for the average counts of 4 LDs which were incrementally exposed to doses of 6.45 cGy for total doses of 0, 6.45, 12.9, 19.35, 25.8, 32.25, 38.7, 45.15, and

51.6 cGy by placing the dots in a 40 × 40 mm, 225 kV, and 13 mA x-ray beam in the small animal irradiator for 1 second and then read with the microSTAR reader 5 times.

Time in Beam (seconds)	**Calculated Dose (cGy)**		
0	0		
Error of Measurement			
LD 1 (counts)	**LD 2 (counts)**	**LD3 (counts)**	**LD 4 (counts)**
3.61	3.74	3.46	3.61
3.74	3.46	4.12	3.61
3.61	3.61	3.74	4.00
4.36	3.46	3.87	3.46
3.46	3.87	3.74	3.46
Error of Average (counts)			
1.69	1.62	1.70	1.62
Time in Beam (seconds)	**Calculated Dose (cGy)**		
1	6.45		
Error of Measurement			
LD 1 (counts)	**LD 2 (counts)**	**LD3 (counts)**	**LD 4 (counts)**
189.59	192.05	191.57	196.15
183.99	188.71	187.31	188.04
175.83	176.26	177.02	178.93
172.44	172.63	173.85	174.38
168.83	168.76	169.48	170.38

Error of Average (counts)			
79.74	80.46	80.51	81.31
Time in Beam (seconds)	**Calculated Dose (cGy)**		
2	12.9		
Error of Measurement			
LD 1 (counts)	**LD 2 (counts)**	**LD3 (counts)**	**LD 4 (counts)**
184.43	251.76	253.54	256.69
250.3398	247.7398	248.67	247.71
235.32	236.23	238.95	239.28
236.70	233.64	235.74	239.02
231.84	229.15	233.42	235.59
102.3402	107.267	108.3094	109.0216
Time in Beam (seconds)	**Calculated Dose (cGy)**		
3	19.35		
Error of Measurement			
LD 1 (counts)	**LD 2 (counts)**	**LD3 (counts)**	**LD 4 (counts)**
304.02	301.36	304.60	307.96
298.32	297.0303	299.11	300.36
293.73	292.82	296.76	296.94
287.53	287.76	289.52	290.31

291.33	285.90	289.00	287.75
Error of Average (counts)			
131.95	131.05	132.31	132.71
Time in Beam (seconds)	**Calculated Dose (cGy)**		
4	25.8		
Error of Measurement			
LD 1 (counts)	**LD 2 (counts)**	**LD3 (counts)**	**LD 4 (counts)**
328.93	328.2667	333.39	334.57
326.6405	329.0836	330.42	334.17
330.33	326.93	328.17	332.25
324.83	324.44	325.20	330.45
Error of Average (counts)			
163.84	163.59	164.66	166.43
Time in Beam (seconds)	**Calculated Dose (cGy)**		
5	32.25		
Error of Measurement			
LD 1 (counts)	**LD 2 (counts)**	**LD3 (counts)**	**LD 4 (counts)**
369.89	372.3104	374.32	382.28
	361.26	359.14	369.78
348.75	353.07	352.94	360.09
356.68	355.84	354.52	363.78

356.6497	354.24	357.34	363.7595
361.38	353.44	359.21	362.76
Error of Average (counts)			
160.43	146.33	146.82	149.89
Time in Beam (seconds)	**Calculated Dose (cGy)**		
6	38.7		
Error of Measurement			
LD 1 (counts)	**LD 2 (counts)**	**LD3 (counts)**	**LD 4 (counts)**
406.65	408.61		
402.37	404.28		408.52
375.85	384.33	383.75	392.10
376	385.35	384.24	394.91
377.44	384.89	388.05	393.38
378.05	384.67	386.52	394.84
383.14	386.62	386.37	394.39
Error of Average (counts)			
145.83	147.92	172.53	161.83
Time in Beam (seconds)	**Calculated Dose (cGy)**		
7	45.15		
Error of Measurement			
LD 1 (counts)	**LD 2 (counts)**	**LD3 (counts)**	**LD 4 (counts)**

417.28	409.98	415.87	420.43
413.56	408.91	412.04	421.31
412.03	408.66	411.20	417.75
406.52	406.95	413.31	418.43
405.94	404.8098	410.64	414.52

Error of Average (counts)

183.84	182.40	184.53	187.16

Time in Beam (seconds)	**Calculated Dose (cGy)**
8	51.6

Error of Measurement

LD 1 (counts)	**LD 2 (counts)**	**LD3 (counts)**	**LD 4 (counts)**
431.32	439.80	433.08	442.60
431.73	437.21	434.16	438.79
433.57	436.6704	432.15	436.90
425.40	433.26	429.62	437.01
425.76	433.15	427.91	436.19

Error of Average (counts)

192.11	195.00	192.92	196.02

APPENDIX J: MEASUREMENT DATA FOR Figure 18, Figure 19, Figure 20, and Figure 21

Table 51: Measurement data for the average counts of 4 FDs which were incrementally exposed to doses of 6.45 cGy for total doses of 0, 6.45, 12.9, 19.35, 25.8, 32.25, 38.7, 45.15, and 51.6 cGy by placing the dots in a 40 × 40 mm, 225 kV, and 13 mA x-ray beam in the small animal irradiator for 1 second and then read with the microSTAR reader 5 times.

Time in Beam (seconds)	**Calculated Dose (cGy)**		
0	0		
FD 1 (counts)	**FD 2 (counts)**	**FD3 (counts)**	**FD 4 (counts)**
24	24	26	24
18	23		
20	21	24	19
19	21	27	27
20			
19	24	27	25
25	20	29	28
	Average (counts)		
20.71	22.17	26.6	24.6
Time in Beam (seconds)	**Calculated Dose (cGy)**		
1	6.45		
FD 1 (counts)	**FD 2 (counts)**	**FD3 (counts)**	**FD 4 (counts)**
138	141	129	115
142	137	137	120
144	144	137	123

141	145	139	118
136	135	145	124
Average (counts)			
140.2	140.4	137.4	120
Time in Beam (seconds)	**Calculated Dose (cGy)**		
2	12.9		
FD 1 (counts)	**FD 2 (counts)**	**FD3 (counts)**	**FD 4 (counts)**
236	262		
273	261	233	214
275	259	225	222
261	277	219	221
260	268	233	217
266	258	233	217
Average (counts)			
261.83	264.17	228.6	218.2
Time in Beam (seconds)	**Calculated Dose (cGy)**		
3	19.35		
FD 1 (counts)	**FD 2 (counts)**	**FD3 (counts)**	**FD 4 (counts)**
360	367	321	303
314	365	346	330
337	390	302	327

342	380		
324	380	327	305
319	382	343	315
	Average (counts)		
332.67	377.33	327.8	316
Time in Beam (seconds)	**Calculated Dose (cGy)**		
4	25.8		
FD 1 (counts)	**FD 2 (counts)**	**FD3 (counts)**	**FD 4 (counts)**
454	478	474	394
474	477	460	393
466	507	467	411
475	531	435	411
489	511	434	378
	Average (counts)		
471.6	500.8	454	397.4
Time in Beam (seconds)	**Calculated Dose (cGy)**		
5	32.25		
FD 1 (counts)	**FD 2 (counts)**	**FD3 (counts)**	**FD 4 (counts)**
489	558	560	532
493	561	539	521
508	567	564	539

496	564	554	521
505	555	551	530
Average (counts)			
498.2	561	553.6	528.6
Time in Beam (seconds)	**Calculated Dose (cGy)**		
6	38.7		
FD 1 (counts)	**FD 2 (counts)**	**FD3 (counts)**	**FD 4 (counts)**
637	669	563	509
647	688	554	535
634	667	546	534
623	695	561	554
665	669	571	563
Average (counts)			
641.2	677.6	559	539
Time in Beam (seconds)	**Calculated Dose (cGy)**		
7	45.15		
FD 1 (counts)	**FD 2 (counts)**	**FD3 (counts)**	**FD 4 (counts)**
824	745	727	602
825	747	689	621
813	734		
791	714	715	586

799	733	694	603
797	739	704	593
Average (counts)			
808.17	735.33	705.8	601
Time in Beam (seconds)	**Calculated Dose (cGy)**		
8	51.6		
FD 1 (counts)	**FD 2 (counts)**	**FD3 (counts)**	**FD 4 (counts)**
804	824	713	756
803	847	713	734
814	827	695	732
796	854	716	742
822	806	721	742
Average (counts)			
807.8	831.6	711.6	741.2

Table 52: Error of Measurement data for the average counts of 4 LDs which were incrementally exposed to doses of 6.45 cGy for total doses of 0, 6.45, 12.9, 19.35, 25.8, 32.25, 38.7, 45.15, and

51.6 cGy by placing the dots in a 40 × 40 mm, 225 kV, and 13 mA x-ray beam in the small animal irradiator for 1 second and then read with the microSTAR reader 5 times.

Time in Beam (seconds)	**Calculated Dose (cGy)**		
0	0		
Error of Measurement			
FD 1 (counts)	**FD 2 (counts)**	**FD3 (counts)**	**FD 4 (counts)**
4.90	4.90	5.10	4.90
4.24	4.80	0.00	0.00
4.47	4.58	4.90	4.36
4.36	4.58	5.20	5.20
4.47	0.00	0.00	0.00
4.36	4.90	5.20	5.00
5.00	4.47	5.39	5.29
Error of Average (counts)			
1.72	1.92	2.31	2.22
Time in Beam (seconds)	**Calculated Dose (cGy)**		
1	6.45		
Error of Measurement			
FD 1 (counts)	**FD 2 (counts)**	**FD3 (counts)**	**FD 4 (counts)**
11.75	11.87	11.36	10.72
11.92	11.70	11.70	10.95
12.00	12.00	11.70	11.09

11.87	12.04	11.79	10.86
11.66	11.62	12.04	11.14

Error of Average (counts)

5.30	5.30	5.24	4.90

Time in Beam (seconds)	**Calculated Dose (cGy)**
2	12.9

Error of Measurement

FD 1 (counts)	**FD 2 (counts)**	**FD3 (counts)**	**FD 4 (counts)**
15.36	16.19	0.00	0.00
16.52	16.16	15.26	14.63
16.58	16.09	15.00	14.90
16.16	16.64	14.80	14.87
16.12	16.37	15.26	14.73
16.31	16.06	15.26	14.73

Error of Average (counts)

6.61	6.64	6.76	6.61

Time in Beam (seconds)	**Calculated Dose (cGy)**
3	19.35

Error of Measurement

FD 1 (counts)	**FD 2 (counts)**	**FD3 (counts)**	**FD 4 (counts)**
18.97	19.16	17.92	17.41

17.72	19.10	18.60	18.17
18.36	19.75	17.38	18.08
18.49	19.49	0.00	0.00
18.00	19.49	18.08	17.46
17.86	19.54	18.52	17.75
Error of Average (counts)			
7.45	7.93	8.10	7.95
Time in Beam (seconds)	**Calculated Dose (cGy)**		
4	25.8		
Error of Measurement			
FD 1 (counts)	**FD 2 (counts)**	**FD3 (counts)**	**FD 4 (counts)**
21.31	21.86	21.77	19.85
21.77	21.84	21.45	19.82
21.59	22.52	21.61	20.27
21.79	23.04	20.86	20.27
22.11	22.61	20.83	19.44
Error of Average (counts)			
9.71	10.01	9.53	8.92
Time in Beam (seconds)	**Calculated Dose (cGy)**		
5	32.25		
Error of Measurement			

FD 1 (counts)	FD 2 (counts)	FD3 (counts)	FD 4 (counts)
22.11	23.62	23.66	23.07
22.20	23.69	23.22	22.83
22.54	23.81	23.75	23.22
22.27	23.75	23.54	22.83
22.47	23.56	23.47	23.02
Error of Average (counts)			
9.98	10.59	10.52	10.28
Time in Beam (seconds)	**Calculated Dose (cGy)**		
6	38.7		

Error of Measurement

FD 1 (counts)	FD 2 (counts)	FD3 (counts)	FD 4 (counts)
25.24	25.87	23.73	22.56
25.44	26.23	23.54	23.13
25.18	25.83	23.37	23.11
24.96	26.36	23.69	23.54
25.79	25.87	23.90	23.73
Error of Average (counts)			
11.32	11.64	10.57	10.38
Time in Beam (seconds)	**Calculated Dose (cGy)**		
7	45.15		

Error of Measurement			
FD 1 (counts)	**FD 2 (counts)**	**FD3 (counts)**	**FD 4 (counts)**
28.71	27.29	26.96	24.54
28.72	27.33	26.25	24.92
28.51	27.09	0.00	0.00
28.12	26.72	26.74	24.21
28.27	27.07	26.34	24.56
28.23	27.18	26.53	24.35
Error of Average (counts)			
11.61	11.07	11.88	10.96
Time in Beam (seconds)	**Calculated Dose (cGy)**		
8	51.6		
Error of Measurement			
FD 1 (counts)	**FD 2 (counts)**	**FD3 (counts)**	**FD 4 (counts)**
28.35	28.71	26.70	27.50
28.34	29.10	26.70	27.09
28.53	28.76	26.36	27.06
28.21	29.22	26.76	27.24
28.67	28.39	26.85	27.24
Error of Average (counts)			
12.71	12.90	11.93	12.18

APPENDIX K: MEASUREMENT DATA FOR FIGURE 22 AND FIGURE 23

Table 53: Measurement data for the average number of counts of 4 LDs exposed to 0, 51.6, 96.75, 199.95, 303.15, 399.9, 503.1, 599.85, 703.05, 799.8, 999.75, 1102.95, 1206.15, 1296.15, 1399.65, 1548, 1599.6, and 1651.2 cGy by putting the dots in a 40 × 40 mm, 225 kV, and 13 mA beam in the small animal irradiator for various periods. Each dot was measured a minimum of 5 times after each exposure.

Time in Beam (seconds)	**Calculated Dose (cGy)**		
0	0		
LD 1 (counts)	**LD 2 (counts)**	**LD 3 (counts)**	**LD 4 (counts)**
41	37	45	56
39	37	44	57
39	41	42	56
40	39	52	54
39	39	44	59
Average (counts)			
39.6	38.6	45.4	56.4
Time in Beam (seconds)	**Calculated Dose (cGy)**		
8	51.6		
LD 1 (counts)	**LD 2 (counts)**	**LD 3 (counts)**	**LD 4 (counts)**
90748	91835	93650	95757
91023	90972	91732	95881
89778	89997	92998	93881
88133	90821	91195	94084
88507	88601	92723	93169

Average			
89637.8	90445.2	92459.6	94554.4
Time in Beam (seconds)	**Calculated Dose (cGy)**		
15	96.75		
LD 1 (counts)	**LD 2 (counts)**	**LD 3 (counts)**	**LD 4 (counts)**
189733	192834	189366	185607
179869	185682	185115	182937
177876	181496	183897	179893
174772	177339	174552	176054
172859	176105	175245	177928
Average (counts)			
179021.8	182691.2	181635	180483.8
Time in Beam (seconds)	**Calculated Dose (cGy)**		
31	199.95		
LD 1 (counts)	**LD 2 (counts)**	**LD 3 (counts)**	**LD 4 (counts)**
380603	390580	379987	376087
363291	375438	378400	372386
353927	367034	365503	369426
353873	365097	366045	364044
349466	365615	364010	361399
Average (counts)			

360232	372752.8	370789	368668.4
Time in Beam (seconds)	**Calculated Dose (cGy)**		
47	303.15		
LD 1 (counts)	**LD 2 (counts)**	**LD 3 (counts)**	**LD 4 (counts)**
536531	562067	523620	547057
526527	538052	534399	544271
523578	535780	520682	538828
517477	528130	529898	533728
527135	534100	523264	532051
Average (counts)			
526249.6	539625.8	526372.6	539187
Time in Beam (seconds)	**Calculated Dose (cGy)**		
62	399.9		
LD 1 (counts)	**LD 2 (counts)**	**LD 3 (counts)**	**LD 4 (counts)**
697988	708979	714741	728221
695083	703499	706911	711779
680317	695904	698637	716806
678023	691153	687660	695080
676597	691151	695833	695058
Average (counts)			
685601.6	698137.2	700756.4	709388.8

Time in Beam (seconds)	Calculated Dose (cGy)		
78	503.1		
LD 1 (counts)	**LD 2 (counts)**	**LD 3 (counts)**	**LD 4 (counts)**
863569	886686	874936	907402
863152	882923	870926	892829
823978	845528	839312	859838
821889	849377	842202	867313
819228	837386	836542	859434
Average (counts)			
838363.2	860380	852783.6	877363.2
Time in Beam (seconds)	**Calculated Dose (cGy)**		
93	599.85		
LD 1 (counts)	**LD 2 (counts)**	**LD 3 (counts)**	**LD 4 (counts)**
981506	1042658	1048171	1050002
973952	1033308	1049410	1037809
968027	1030050	1025992	1049715
980288	1019315	1040074	1026951
962396	1016433	1027685	1025029
Average (counts)			
973233.8	1028353	1038266	1037901

Time in Beam (seconds)	**Calculated Dose (cGy)**		
109	703.05		
LD 1 (counts)	**LD 2 (counts)**	**LD 3 (counts)**	**LD 4 (counts)**
1149584	1194799	1225222	1234839
1154371	1191884	1219052	1228563
1164212	1195996	1209555	1221245
1135662	1187489	1201071	1217462
1123506	1179735	1193825	1203596
Average (counts)			
1145467	1189981	1209745	1221141
Time in Beam (seconds)	**Calculated Dose (cGy)**		
124	799.8		
LD 1 (counts)	LD 2 (counts)	LD 3 (counts)	LD 4 (counts)
1279994	1335833	1365857	1385813
1287938	1344222	1367295	1377089
1267809	1347437	1364124	1365628
1271988	1331380	1354664	1357272
1260835	1310192	1342083	1347879
Average (counts)			
1273713	1333813	1358805	1366736

Time in Beam (seconds)	Calculated Dose (cGy)		
140	903		
LD 1 (counts)	**LD 2 (counts)**	**LD 3 (counts)**	**LD 4 (counts)**
1458271	1498887	1544713	1597497
1468853	1503211	1554630	1552391
1452420	1509606	1546500	1543938
1471191	1498687	1510223	1558182
1438640	1474123	1529434	1539693
Average (counts)			
1457875	1496903	1537100	1558340
Time in Beam (seconds)	**Calculated Dose (cGy)**		
155	999.75		
LD 1 (counts)	**LD 2 (counts)**	**LD 3 (counts)**	**LD 4 (counts)**
1574228	1658767	1713444	1722269
1593922	1658768	1762724	1745970
1569903	1642999	1735194	1711474
1548178	1640683	1717159	1710390
1559010	1599448	1687172	1688353
Average (counts)			
1569048	1640133	1723139	1715691

Time in Beam (seconds)	**Calculated Dose (cGy)**		
163	1051.35		
LD 1 (counts)	LD 2 (counts)	LD 3 (counts)	LD 4 (counts)
1605198	1691941	1725798	1705608
1626066	1694853	1750881	1704366
1621391	1692459	1728342	1702029
1616180	1689699	1715393	1700846
1597110	1681246	1741746	1689266
Average (counts)			
1613189	1690040	1732432	1700423
Time in Beam (seconds)	**Calculated Dose (cGy)**		
170	1096.5		
LD 1 (counts)	**LD 2 (counts)**	**LD 3 (counts)**	**LD 4 (counts)**
1657707	1770967	1827992	1862058
1678595	1771183	1875002	1859806
1644954	1757512	1846423	1844791
1651095	1767310	1830478	1847717
1619390	1749435	1824020	1835885
Average (counts)			
1650348	1763281	1840783	1850051

Time in Beam (seconds)	Calculated Dose (cGy)		
186	1199.7		
LD 1 (counts)	**LD 2 (counts)**	**LD 3 (counts)**	**LD 4 (counts)**
1778223	1963973	1978277	2020790
1789494	1945802	1960441	2017591
1670402	1860573	1906194	1936415
1664938	1888392	1929314	1928236
1676683	1902749	1951821	1930183
Average (counts)			
1715948	1912298	1945209	1966643
Time in Beam (seconds)	**Calculated Dose (cGy)**		
201	1296.45		
LD 1 (counts)	**LD 2 (counts)**	**LD 3 (counts)**	**LD 4 (counts)**
1894894	1987707	2042648	2043615
1783963	1977583	2018272	2048289
1806920	1991468	2022216	2059097
1805699	2020872	2012583	2078588
1796855	2000977	2036194	2048923
Average (counts)			
1817666	1995721	2026383	2055702

Time in Beam (seconds)	**Calculated Dose (cGy)**		
217	1399.65		
LD 1 (counts)	LD 2 (counts)	LD 3 (counts)	LD 4 (counts)
2057540	2184771	2226854	2241567
1962550	2147821	2176614	2202983
1988132	2117697	2156115	2180432
1941604	2119182	2149737	2182327
1942281	2121840	2175354	2199241
Average (counts)			
1978421	2138262	2176935	2201310
Time in Beam (seconds)	**Calculated Dose (cGy)**		
232	1496.4		
LD 1 (counts)	**LD 2 (counts)**	**LD 3 (counts)**	**LD 4 (counts)**
2187818	2311430	2375606	2338905
2131807	2247919	2322277	2342491
2114241	2267511	2343954	2331857
2135422	2248504	2302918	2318632
2147672	2234797	2323081	2313438
Average (counts)			
2143392	2262032	2333567	2329065

Time in Beam (seconds)	**Calculated Dose (cGy)**		
240	1548		
LD 1 (counts)	LD 2 (counts)	LD 3 (counts)	LD 4 (counts)
2277728	2344085	2394634	2388069
2199831	2311069	2357852	2379869
2234382	2293127	2339234	2348134
2156774	2296085	2365354	2352559
2171002	2280858	2340279	2351673
Average (counts)			
2207943	2305045	2359471	2364061
Time in Beam (seconds)	**Calculated Dose (cGy)**		
248	1599.6		
LD 1 (counts)	**LD 2 (counts)**	**LD 3 (counts)**	**LD 4 (counts)**
2243977	2349938	2411124	2415771
2211917	2323383	2392074	2399418
2177486	2309251	2380153	2394043
2171331	2324907	2389334	2412180
2169312	2300769	2389336	2389665
Average (counts)			
2194805	2321650	2392404	2402215

Time in Beam (seconds)	Calculated Dose (cGy)		
256	1651.2		
LD 1 (counts)	**LD 2 (counts)**	**LD 3 (counts)**	**LD 4 (counts)**
2262977	2393715	2441515	2455919
2233906	2344993	2415909	2432121
2207552	2353080	2429623	2436297
2208382	2360699	2429425	2436156
2256811	2353159	2410569	2426905
Average (counts)			
2233926	2361129	2425408	2437480

Table 54: Error of measurement data for the average number of counts of 4 LDs exposed to 0, 51.6, 96.75, 199.95, 303.15, 399.9, 503.1, 599.85, 703.05, 799.8, 999.75, 1102.95, 1206.15, 1296.15, 1399.65, 1548, 1599.6, and 1651.2 cGy by putting the dots in a 40 × 40 mm, 225 kV, and 13 mA beam in the small animal irradiator for various periods. Each dot was measured a minimum of 5 times after each exposure.

Time in Beam (seconds)	**Calculated Dose (cGy)**		
0	0		
Error of Measurement			
LD 1 (counts)	**LD 2 (counts)**	**LD 3 (counts)**	**LD 4 (counts)**
6.40	6.08	6.71	7.48
6.24	6.08	6.63	7.55
6.24	6.40	6.48	7.48
6.32	6.24	7.21	7.35
6.24	6.24	6.63	7.68
Error of Average (counts)			
2.81	2.78	3.01	3.36
Time in Beam (seconds)	**Calculated Dose (cGy)**		
8	51.6		
Error of Measurement			
LD 1 (counts)	**LD 2 (counts)**	**LD 3 (counts)**	**LD 4 (counts)**
301.24	303.04	306.02	309.45
301.70	301.62	302.87	309.65
299.63	299.99	304.96	306.40

296.87	301.37	301.99	306.73
297.50	297.66	304.50	305.24
Average (counts)			
133.89	134.50	135.98	137.52
Time in Beam (seconds)	**Calculated Dose (cGy)**		
15	96.75		
Error of Measurement			
LD 1 (counts)	**LD 2 (counts)**	**LD 3 (counts)**	**LD 4 (counts)**
435.58	439.13	435.16	430.82
424.11	430.91	430.25	427.71
421.75	426.02	428.83	424.14
418.06	421.12	417.79	419.59
415.76	419.65	418.62	421.82
Error of Average (counts)			
189.22	191.15	190.60	189.99
Time in Beam (seconds)	**Calculated Dose (cGy)**		
31	199.95		
Error of Measurement			
LD 1 (counts)	**LD 2 (counts)**	**LD 3 (counts)**	**LD 4 (counts)**
616.93	624.96	616.43	613.26
602.74	612.73	615.14	610.23

594.92	605.83	604.57	607.80
594.87	604.23	605.02	603.36
591.16	604.66	603.33	601.16
Error of Average (counts)			
268.41	273.04	272.32	271.54
Time in Beam (seconds)	**Calculated Dose (cGy)**		
47	303.15		
Error of Measurement			
LD 1 (counts)	**LD 2 (counts)**	**LD 3 (counts)**	**LD 4 (counts)**
732.48	749.71	723.62	739.63
725.62	733.52	731.03	737.75
723.59	731.97	721.58	734.05
719.36	726.73	727.94	730.57
726.04	730.82	723.37	729.42
Error of Average (counts)			
324.42	328.52	324.46	328.39
Time in Beam (seconds)	**Calculated Dose (cGy)**		
62	399.9		
Error of Measurement			
LD 1 (counts)	**LD 2 (counts)**	**LD 3 (counts)**	**LD 4 (counts)**
835.46	842.01	845.42	853.36

833.72	838.75	840.78	843.67
824.81	834.21	835.85	846.64
823.42	831.36	829.25	833.71
822.56	831.35	834.17	833.70
Error of Average (counts)			
370.30	373.67	374.37	376.67
Time in Beam (seconds)	**Calculated Dose (cGy)**		
78	503.1		
Error of Measurement			
LD 1 (counts)	**LD 2 (counts)**	**LD 3 (counts)**	**LD 4 (counts)**
929.28	941.64	935.38	952.58
929.06	939.64	933.23	944.90
907.73	919.53	916.14	927.27
906.58	921.62	917.72	931.30
905.11	915.09	914.63	927.06
Error of Average (counts)			
409.48	414.82	412.99	418.89
Time in Beam (seconds)	**Calculated Dose (cGy)**		
93	599.85		
Error of Measurement			
LD 1 (counts)	**LD 2 (counts)**	**LD 3 (counts)**	**LD 4 (counts)**

990.71	1021.11	1023.80	1024.70
986.89	1016.52	1024.41	1018.73
983.88	1014.91	1012.91	1024.56
990.09	1009.61	1019.84	1013.39
981.02	1008.18	1013.75	1012.44
Error of Average (counts)			
441.19	453.51	455.69	455.61
Time in Beam (seconds)	**Calculated Dose (cGy)**		
109	703.05		
Error of Measurement			
LD 1 (counts)	**LD 2 (counts)**	**LD 3 (counts)**	**LD 4 (counts)**
1072.19	1093.07	1106.90	1111.23
1074.42	1091.73	1104.11	1108.41
1078.99	1093.62	1099.80	1105.10
1065.67	1089.72	1095.93	1103.39
1059.96	1086.16	1092.62	1097.09
Error of Average (counts)			
478.64	487.85	491.88	494.19
Time in Beam (seconds)	**Calculated Dose (cGy)**		
124	799.8		
Error of Measurement			

LD 1 (counts)	LD 2 (counts)	LD 3 (counts)	LD 4 (counts)
1131.37	1155.78	1168.7	1177.21
1134.87	1159.41	1169.31	1173.49
1125.97	1160.79	1167.96	1168.6
1127.82	1153.85	1163.9	1165.02
1122.87	1144.64	1158.48	1160.98
Error of Average (counts)			
504.72	516.49	521.31	522.83

Time in Beam (seconds)	Calculated Dose (cGy)
140	903

Error of Measurement

LD 1 (counts)	LD 2 (counts)	LD 3 (counts)	LD 4 (counts)
1207.59	1224.29	1242.87	1263.92
1211.96	1226.06	1246.85	1245.95
1205.16	1228.66	1243.58	1242.55
1212.93	1224.21	1228.91	1248.27
1199.43	1214.14	1236.7	1240.84
Error of Average (counts)			
539.98	547.16	554.45	558.27

Time in Beam (seconds)	Calculated Dose (cGy)
155	999.75

Error of Measurement			
LD 1 (counts)	**LD 2 (counts)**	**LD 3 (counts)**	**LD 4 (counts)**
1254.68	1287.93	1308.99	1312.35
1262.51	1287.93	1327.68	1321.35
1252.96	1281.8	1317.27	1308.23
1244.26	1280.89	1310.4	1307.82
1248.6	1264.69	1298.91	1299.37
Error of Average (counts)			
560.19	572.74	587.05	585.78
Time in Beam (seconds)	**Calculated Dose (cGy)**		
163	1051.35		

Error of Measurement			
LD 1 (counts)	**LD 2 (counts)**	**LD 3 (counts)**	**LD 4 (counts)**
1266.96	1300.75	1313.7	1305.99
1275.17	1301.87	1323.21	1305.51
1273.34	1300.95	1314.66	1304.62
1271.29	1299.88	1309.73	1304.17
1263.77	1296.63	1319.75	1299.72
Error of Average (counts)			
568.01	581.38	588.63	583.17
Time in Beam (seconds)	**Calculated Dose (cGy)**		

170	1096.5		
Error of Measurement			
LD 1 (counts)	**LD 2 (counts)**	**LD 3 (counts)**	**LD 4 (counts)**
1287.52	1330.78	1352.03	1364.57
1295.61	1330.86	1369.31	1363.75
1282.56	1325.71	1358.83	1358.23
1284.95	1329.40	1352.95	1359.31
1272.55	1322.66	1350.56	1354.95
Error of Average (counts)			
574.52	593.85	606.76	608.28
Time in Beam (seconds)	**Calculated Dose (cGy)**		
186	1199.7		
Error of Measurement			
LD 1 (counts)	**LD 2 (counts)**	**LD 3 (counts)**	**LD 4 (counts)**
1333.5	1401.42	1406.51	1421.55
1337.72	1394.92	1400.16	1420.42
1292.44	1364.03	1380.65	1391.55
1290.33	1374.19	1387	1388.61
1294.87	1379.4	1397.08	1389.31
Error of Average (counts)			
585.82	618.43	623.73	627.16

Time in Beam (seconds)	Calculated Dose (cGy)		
201	1296.45		
Error of Measurement			
LD 1 (counts)	**LD 2 (counts)**	**LD 3 (counts)**	**LD 4 (counts)**
1376.55	1409.86	1429.21	1429.55
1335.65	1406.27	1420.66	1431.18
1344.22	1411.19	1422.05	1434.96
1343.76	1421.57	1418.66	1441.73
1340.47	1414.56	1426.95	1431.41
Error of Average (counts)			
602.94	631.78	636.61	641.20
Time in Beam (seconds)	**Calculated Dose (cGy)**		
217	1399.65		
Error of Measurement			
LD 1 (counts)	**LD 2 (counts)**	**LD 3 (counts)**	**LD 4 (counts)**
1434.41	1478.1	1492.27	1497.19
1400.91	1465.55	1475.34	1484.25
1410.01	1455.23	1468.37	1476.63
1393.42	1455.74	1466.2	1477.27
1393.66	1456.65	1474.91	1482.98
Error of Average (counts)			

629.03	653.95	659.84	663.52
Time in Beam (seconds)	**Calculated Dose (cGy)**		
232	1496.4		
Error of Measurement			
LD 1 (counts)	**LD 2 (counts)**	**LD 3 (counts)**	**LD 4 (counts)**
1479.13	1520.34	1541.3	1529.35
1460.07	1499.31	1523.9	1530.52
1454.04	1505.83	1531	1527.04
1461.31	1499.5	1517.54	1522.71
1465.49	1494.92	1524.17	1521
Error of Average (counts)			
654.74	672.61	683.16	682.50
Time in Beam (seconds)	**Calculated Dose (cGy)**		
240	1548		
Error of Measurement			
LD 1 (counts)	**LD 2 (counts)**	**LD 3 (counts)**	**LD 4 (counts)**
1509.21	1531.04	1547.46	1545.34
1483.18	1520.22	1535.53	1542.68
1494.79	1514.31	1529.46	1532.36
1468.6	1515.28	1537.97	1533.81
1473.43	1510.25	1529.8	1533.52

Error of Average (counts)			
664.52	678.98	686.95	687.61
Time in Beam (seconds)	**Calculated Dose (cGy)**		
248	1599.6		
Error of Measurement			
LD 1 (counts)	**LD 2 (counts)**	**LD 3 (counts)**	**LD 4 (counts)**
1497.99	1532.95	1552.78	1554.28
1487.25	1524.27	1546.63	1549.01
1475.63	1519.62	1542.77	1547.27
1473.54	1524.77	1545.75	1553.12
1472.86	1516.83	1545.75	1545.85
Error of Average (counts)			
662.54	681.42	691.72	693.14
Time in Beam (seconds)	**Calculated Dose (cGy)**		
256	1651.2		
Error of Measurement			
LD 1 (counts)	**LD 2 (counts)**	**LD 3 (counts)**	**LD 4 (counts)**
1504.32	1547.16	1562.54	1567.14
1494.63	1531.34	1554.32	1559.53
1485.78	1533.98	1558.73	1560.86
1486.06	1536.46	1558.66	1560.82

1502.27	1534	1552.6	1557.85
Error of Average (counts)			
668.42	687.19	696.48	698.21

APPENDIX L: MEASUREMENT DATA FOR FIGURE 24 AND FIGURE 25

Table 55: Measurement data for the average number of counts of 4 FDs exposed to 0, 51.6, 96.75, 199.95, 303.15, 399.9, 503.1, 599.85, 703.05, 799.8, 999.75, 1102.95, 1206.15, 1296.15, 1399.65, 1548, 1599.6, and 1651.2 cGy by putting the dots in a 40 × 40 mm, 225 kV, and 13 mA beam in the small animal irradiator for various periods. Each dot was measured a minimum of 5 times after each exposure.

Time in Beam (seconds)	**Calculated Dose (cGy)**		
0	0		
FD 1 (counts)	**FD 2 (counts)**	**FD 3 (counts)**	**FD 4 (counts)**
15	18	12	16
14	16	14	18
18	17	16	18
15	16	18	17
13	16	15	17
	Average (counts)		
15	16.6	15	17.2
Time in Beam (seconds)	**Calculated Dose (cGy)**		
8	51.6		
FD 1 (counts)	**FD 2 (counts)**	**FD 3 (counts)**	**FD 4 (counts)**
350	584	312	313
345	568		
326	574	295	297
310	577	298	304

316	558	300	310
321	558	291	301
Average (counts)			
328	569.833	299.2	305
Time in Beam (seconds)	**Calculated Dose (cGy)**		
15	96.75		
FD 1 (counts)	**FD 2 (counts)**	**FD 3 (counts)**	**FD 4 (counts)**
677	1117	590	618
641	1031	599	596
689	1036	564	586
660	1041	570	600
648	1024	577	590
Average (counts)			
663	1049.8	580	598
Time in Beam (seconds)	**Calculated Dose (cGy)**		
31	199.95		
FD 1 (counts)	**FD 2 (counts)**	**FD 3 (counts)**	**FD 4 (counts)**
1413	2279	1229	1298
1326	2162	1187	1205
1347	2161	1165	1236
1328	2176	1158	1229

1361	2174	1170	1222
Average (counts)			
1355	2190.4	1181.8	1238
Time in Beam (seconds)	**Calculated Dose (cGy)**		
47	303.15		
FD 1 (counts)	**FD 2 (counts)**	**FD 3 (counts)**	**FD 4 (counts)**
2299	3333	1926	1815
2168	3270	1850	1683
2193	3340	1813	1744
2237	3195	1834	1606
2211	3161	1814	1746
Average (counts)			
2221.6	3259.8	1847.4	1718.8
Time in Beam (seconds)	**Calculated Dose (cGy)**		
62	399.9		
FD 1 (counts)	**FD 2 (counts)**	**FD 3 (counts)**	**FD 4 (counts)**
2909	4591	2605	2201
2853	4360	2501	2117
2786	4331	2508	2129
2778	4421	2497	2154
2773	4322	2441	2076

Average (counts)			
2819.8	4405	2510.4	2135.4
Time in Beam (seconds)	**Calculated Dose (cGy)**		
78	503.1		
FD 1 (counts)	**FD 2 (counts)**	**FD 3 (counts)**	**FD 4 (counts)**
3745	5659	3210	2823
3467	5425	3116	2813
3459	5480	3147	2904
3369	5490	3102	2854
3405	5516	3110	2830
Averages			
3489	5514	3137	2844.8
Time in Beam (seconds)	**Calculated Dose (cGy)**		
93	599.85		
FD 1 (counts)	**FD 2 (counts)**	**FD 3 (counts)**	**FD 4 (counts)**
4432	6945	4002	3353
4264	6592	3819	3368
4233	6562	3837	3379
4241	6506	3728	3300
4214	6625	3726	3259
Averages			

4276.8	6646	3822.4	3331.8
Time in Beam (seconds)	**Calculated Dose (cGy)**		
109	703.5		
FD 1 (counts)	**FD 2 (counts)**	**FD 3 (counts)**	**FD 4 (counts)**
5081	7911	4254	4037
5057	7647	4092	3990
4858	7598	4117	4103
4882	7634	4106	4042
4689	7549	4135	4096
Average (counts)			
4913.4	7667.8	4140.8	4053.6
Time in Beam (seconds)	**Calculated Dose (cGy)**		
124	799.8		
FD 1 (counts)	**FD 2 (counts)**	**FD 3 (counts)**	**FD 4 (counts)**
5679	8984	4570	5056
5374	8733	4243	4889
5276	8704	4196	4846
5611	8523	4169	4959
5269	8508	4386	4798
Average (counts)			
5441.8	8690.4	4312.8	4909.6

Time in Beam (seconds)	Calculated Dose (cGy)		
140	903		
FD 1 (counts)	**FD 2 (counts)**	**FD 3 (counts)**	**FD 4 (counts)**
6567	10414	5142	5863
6349	10107	4913	5790
6286	9896	4926	5624
6121	9757	4939	5639
6249	9784	4820	5626
Average (counts)			
6314.4	9991.6	4948	5708.4
Time in Beam (seconds)	**Calculated Dose (cGy)**		
155	999.75		
FD 1 (counts)	**FD 2 (counts)**	**FD 3 (counts)**	**FD 4 (counts)**
7231	11859	5728	6488
6844	11241	5649	6283
6979	11385	5453	6272
6660	11127	5510	6171
6716	11175	5597	6253
Average (counts)			
6886	11357.4	5587.4	6293.4

Time in Beam (seconds)	Calculated Dose (cGy)		
163	1051.35		
FD 1 (counts)	**FD 2 (counts)**	**FD 3 (counts)**	**FD 4 (counts)**
7708	12280	6580	6678
7089	11792	6301	6509
7134	11521	6290	6441
7083	11705	6248	6434
7087	11389	6142	6375
Average (counts)			
7220.2	11737.4	6312.2	6487.4
Time in Beam (seconds)	**Calculated Dose (cGy)**		
170	1096.5		
FD 1 (counts)	**FD 2 (counts)**	**FD 3 (counts)**	**FD 4 (counts)**
7890	12618	6125	6563
7611	12129	5992	6431
7486	11872	5934	6381
7470	11770	5844	6341
7297	11682	5792	6224
Average (counts)			
7550.8	12014.2	5937.4	6388

Time in Beam (seconds)	Calculated Dose (cGy)		
186	1199.7		
FD 1 (counts)	**FD 2 (counts)**	**FD 3 (counts)**	**FD 4 (counts)**
8558	13902	6691	7614
8482	13154	6389	7314
8393	13372	6310	7225
8280	13101	6483	7182
8235	12949	6447	7156
Average (counts)			
8389.6	13295.6	6464	7298.2
Time in Beam (seconds)	**Calculated Dose (cGy)**		
201	1296.45		
FD 1 (counts)	**FD 2 (counts)**	**FD 3 (counts)**	**FD 4 (counts)**
9429	14063	7265	7828
8884	13573	6934	7701
9073	13729	6880	7639
8834	13746	6904	7692
8943	13429	6815	7558
Average (counts)			
9032.6	13708	6959.6	7683.6

Time in Beam (seconds)	Calculated Dose (cGy)		
217	1399.65		
FD 1 (counts)	**FD 2 (counts)**	**FD 3 (counts)**	**FD 4 (counts)**
9307	13760	7920	7927
8992	12716	7662	7794
8914	14943	7534	7826
9010	15146	7490	7634
9060	14793	7586	7544
Average (counts)			
9056.6	14271.6	7638.4	7745
Time in Beam (seconds)	**Calculated Dose (cGy)**		
232	1496.4		
FD 1 (counts	**FD 2 (counts)**	**FD 3 (counts)**	**FD 4 (counts)**
9808	16256	9058	8349
10031	13763	9118	8345
10161	16239	9052	8321
10282	16194	8977	8281
10102	13183	8922	8243
Averages			
10076.8	15127	9025.4	8307.8

Time in Beam (seconds)	Calculated Dose (cGy)		
1548	240	240	1548
FD 1 (counts)	**FD 2 (counts)**	**FD 3 (counts)**	**FD 4 (counts)**
10790	14799	9337	
10373	13818	9016	9067
10423	16758	9046	8964
10372	16949	9116	8945
10275	16632	8972	8920
10420	13447	9029	8807
Average (counts)			
10442.2	15400.5	9086	8940.6
Time in Beam (seconds)	**Calculated Dose (cGy)**		
248	1599.6		
FD 1 (counts)	**FD 2 (counts)**	**FD 3 (counts)**	**FD 4 (counts)**
10203	14639	8848	8975
9048			
9520	16164	8104	8725
9139	13318	8260	8700
9556	16379	8202	8863
9312	13521	8293	8696
Average (counts)			

9463	14804.2	8341.4	8791.8
Time in Beam (seconds)	**Calculated Dose (cGy)**		
256	1651.2		
FD 1 (counts)	**FD 2 (counts)**	**FD 3 (counts)**	**FD 4 (counts)**
10213	15793	9873	9839
10139	15204	9612	9772
9988	14648	9570	9593
10375	17858	9560	9669
9820	14600	9593	9691
Average (counts)			
10107	15620.6	9641.6	9712.8

Table 56: Error of measurement data for the average number of counts of 4 FDs exposed to 0, 51.6, 96.75, 199.95, 303.15, 399.9, 503.1, 599.85, 703.05, 799.8, 999.75, 1102.95, 1206.15, 1296.15, 1399.65, 1548, 1599.6, and 1651.2 cGy by putting the dots in a 40 × 40 mm, 225 kV, and 13 mA beam in the small animal irradiator for various periods. Each dot was measured a minimum of 5 times after each exposure.

Time in Beam (seconds)	**Calculated Dose (cGy)**		
0	0		
Error of Measurement			
FD 1 (counts)	**FD 2 (counts)**	**FD 3 (counts)**	**FD 4 (counts)**
3.87	4.24	3.46	4.00
3.74	4.00	3.74	4.24
4.24	4.12	4.00	4.24
3.87	4.00	4.24	4.12
3.61	4.00	3.87	4.12
Error of Averages (counts)			
1.73	1.82	1.73	1.85
Time in Beam (seconds)	**Calculated Dose (cGy)**		
8	51.6		
Error of Measurement			
FD 1 (counts)	**FD 2 (counts)**	**FD 3 (counts)**	**FD 4 (counts)**
18.71	24.17	17.66	17.69
18.57	23.83		
18.06	23.96	17.18	17.23

17.61	24.02	17.26	17.44
17.78	23.62	17.32	17.61
17.92	23.62	17.06	17.35
Error of Averages (counts)			
7.39	9.75	7.74	7.81
Time in Beam (seconds)	**Calculated Dose (cGy)**		
15	96.75		
Error of Measurement			
FD 1 (counts)	**FD 2 (counts)**	**FD 3 (counts)**	**FD 4 (counts)**
26.02	33.42	24.29	24.86
25.32	32.11	24.47	24.41
26.25	32.19	23.75	24.21
25.69	32.26	23.87	24.49
25.46	32.00	24.02	24.29
Error of Averages (counts)			
11.52	14.49	10.77	10.94
Time in Beam (seconds)	**Calculated Dose (cGy)**		
31	199.95		
Error of Measurement			
FD 1 (counts)	**FD 2 (counts)**	**FD 3 (counts)**	**FD 4 (counts)**
37.59	47.74	35.06	36.03

36.41	46.50	34.45	34.71
36.70	46.49	34.13	35.16
36.44	46.65	34.03	35.06
36.89	46.63	34.21	34.96
Error of Averages (counts)			
16.46	20.93	15.37	15.74
Time in Beam (seconds)	**Calculated Dose (cGy)**		
47	303.15		
Error of Measurement			
FD 1 (counts)	**FD 2 (counts)**	**FD 3 (counts)**	**FD 4 (counts)**
47.95	57.73	43.89	42.60
46.56	57.18	43.01	41.02
46.83	57.79	42.58	41.76
47.30	56.52	42.83	40.07
47.02	56.22	42.59	41.79
Error of Averages (counts)			
21.08	25.53	19.22	18.54
Time in Beam (seconds)	**Calculated Dose (cGy)**		
62	399.9		
Error of Measurement			
FD 1 (counts)	**FD 2 (counts)**	**FD 3 (counts)**	**FD 4 (counts)**

53.94	67.76	51.04	46.91
53.41	66.03	50.01	46.01
52.78	65.81	50.08	46.14
52.71	66.49	49.97	46.41
52.66	65.74	49.41	45.56
Error of Averages (counts)			
23.75	29.68	22.41	20.67
Time in Beam (seconds)	**Calculated Dose (cGy)**		
78	503.1		
Error of Measurement			
FD 1 (counts)	**FD 2 (counts)**	**FD 3 (counts)**	**FD 4 (counts)**
61.20	75.23	56.66	53.13
58.88	73.65	55.82	53.04
58.81	74.03	56.10	53.89
58.04	74.09	55.70	53.42
58.35	74.27	55.77	53.20
Error of Averages (counts)			
26.42	33.21	25.05	23.85
Time in Beam (seconds)	**Calculated Dose (cGy)**		
93	599.85		
Error of Measurement			

FD 1 (counts)	FD 2 (counts)	FD 3 (counts)	FD 4 (counts)
66.57	83.34	63.26	57.91
65.30	81.19	61.80	58.03
65.06	81.01	61.94	58.13
65.12	80.66	61.06	57.45
64.92	81.39	61.04	57.09
Error of Averages (counts)			
29.25	36.46	27.65	25.81
Time in Beam (seconds)	**Calculated Dose (cGy)**		
109	703.5		
Error of Measurement			
FD 1 (counts)	**FD 2 (counts)**	**FD 3 (counts)**	**FD 4 (counts)**
71.28	88.94	65.22	63.54
71.11	87.45	63.97	63.17
69.70	87.17	64.16	64.05
69.87	87.37	64.08	63.58
68.48	86.88	64.30	64.00
Error of Averages (counts)			
31.35	39.16	28.78	28.47
Time in Beam (seconds)	**Calculated Dose (cGy)**		
124	799.8		

Error of Measurement			
FD 1 (counts)	**FD 2 (counts)**	**FD 3 (counts)**	**FD 4 (counts)**
75.36	94.78	67.60	71.11
73.31	93.45	65.14	69.92
72.64	93.30	64.78	69.61
74.91	92.32	64.57	70.42
72.59	92.24	66.23	69.27
Error of Averages (counts)			
32.99	41.69	29.37	31.34
Time in Beam (seconds)	**Calculated Dose (cGy)**		
140	903		
Error of Measurement			
FD 1 (counts)	**FD 2 (counts)**	**FD 3 (counts)**	**FD 4 (counts)**
81.04	102.05	71.71	76.57
79.68	100.53	70.09	76.09
79.28	99.48	70.19	74.99
78.24	98.78	70.28	75.09
79.05	98.91	69.43	75.01
Error of Averages (counts)			
35.54	44.70	31.46	33.79
Time in Beam (seconds)	**Calculated Dose (cGy)**		

155	999.75		
Error of Measurement			
FD 1 (counts)	**FD 2 (counts)**	**FD 3 (counts)**	**FD 4 (counts)**
85.04	108.90	75.68	80.55
82.73	106.02	75.16	79.27
83.54	106.70	73.84	79.20
81.61	105.48	74.23	78.56
81.95	105.71	74.81	79.08
Error of Averages (counts)			
37.11	47.66	33.43	35.48
Time in Beam (seconds)	**Calculated Dose (cGy)**		
163	1051.35		
Error of Measurement			
FD 1 (counts)	**FD 2 (counts)**	**FD 3 (counts)**	**FD 4 (counts)**
87.80	110.82	81.12	81.72
84.20	108.59	79.38	80.68
84.46	107.34	79.31	80.26
84.16	108.19	79.04	80.21
84.18	106.72	78.37	79.84
Error of Averages (counts)			
38.00	48.45	35.53	36.02

Time in Beam (seconds)	Calculated Dose (cGy)		
170	1096.5		
Error of Measurement			
FD 1 (counts)	**FD 2 (counts)**	**FD 3 (counts)**	**FD 4 (counts)**
88.83	112.33	78.26	81.01
87.24	110.13	77.41	80.19
86.52	108.96	77.03	79.88
86.43	108.49	76.45	79.63
85.42	108.08	76.11	78.89
Error of Averages (counts)			
38.86	49.02	34.46	35.74
Time in Beam (seconds)	**Calculated Dose (cGy)**		
186	1199.7		
Error of Measurement			
FD 1 (counts)	**FD 2 (counts)**	**FD 3 (counts)**	**FD 4 (counts)**
92.51	117.91	81.80	87.26
92.10	114.69	79.93	85.52
91.61	115.64	79.44	85.00
90.99	114.46	80.52	84.75
90.75	113.79	80.29	84.59
Error of Averages (counts)			

40.96	51.57	35.96	38.21
Time in Beam (seconds)	**Calculated Dose (cGy)**		
201	1296.45		
Error of Measurement			
FD 1 (counts)	**FD 2 (counts)**	**FD 3 (counts)**	**FD 4 (counts)**
97.10	118.59	85.23	88.48
94.25	116.50	83.27	87.76
95.25	117.17	82.95	87.40
93.99	117.24	83.09	87.70
94.57	115.88	82.55	86.94
Error of Averages (counts)			
42.50	52.36	37.31	39.20
Time in Beam (seconds)	**Calculated Dose (cGy)**		
217	1399.65		
Error of Measurement			
FD 1 (counts)	**FD 2 (counts)**	**FD 3 (counts)**	**FD 4 (counts)**
96.47	117.30	88.99	89.03
94.83	112.77	87.53	88.28
94.41	122.24	86.80	88.46
94.92	123.07	86.54	87.37
95.18	121.63	87.10	86.86

Error of Averages (counts)			
42.56	53.43	39.09	39.36
Time in Beam (seconds)	**Calculated Dose (cGy)**		
232	1496.4		
Error of Measurement			
FD 1 (counts)	**FD 2 (counts)**	**FD 3 (counts)**	**FD 4 (counts)**
99.04	127.50	95.17	91.37
100.15	117.32	95.49	91.35
100.80	127.43	95.14	91.22
101.40	127.26	94.75	91.00
100.51	114.82	94.46	90.79
Error of Averages (counts)			
44.89	55.00	42.49	40.76
Time in Beam (seconds)	**Calculated Dose (cGy)**		
1548	240	240	1548
Error of Measurement			
FD 1 (counts)	**FD 2 (counts)**	**FD 3 (counts)**	**FD 4 (counts)**
103.87	121.65	96.63	
101.85	117.55	94.95	95.22
102.09	129.45	95.11	94.68
101.84	130.19	95.48	94.58

101.37	128.97	94.72	94.45
102.08	115.96	95.02	93.85
Error of Averages (counts)			
41.72	50.66	38.91	42.29
Time in Beam (seconds)	**Calculated Dose (cGy)**		
248	1599.6		
Error of Measurement			
FD 1 (counts)	**FD 2 (counts)**	**FD 3 (counts)**	**FD 4 (counts)**
101.01	120.99	94.06	94.74
95.12			
97.57	127.14	90.02	93.41
95.60	115.40	90.88	93.27
97.75	127.98	90.56	94.14
96.50	116.28	91.07	93.25
Error of Averages (counts)			
39.71	54.41	40.84	41.93
Time in Beam (seconds)	**Calculated Dose (cGy)**		
256	1651.2		
Error of Measurement			
FD 1 (counts)	**FD 2 (counts)**	**FD 3 (counts)**	**FD 4 (counts)**
101.06	125.67	99.36	99.19

100.69	123.30	98.04	98.85
99.94	121.03	97.83	97.94
101.86	133.63	97.78	98.33
99.10	120.83	97.94	98.44
Error of Averages (counts)			
44.96	55.89	43.91	44.07

APPENDIX M: MEASUREMENT DATA FOR FIGURE 28 AND FIGURE 29

Table 57: Mass of dots with no powder adhered.

Blank Dots Weight (g)
0.0019
0.0019
0.0018
Average (g)
0.0019

Table 58: Mass of dots with unmodified Al_2O_3 powder adhered.

Unmodified Al_2O_3 Dots		
Dot number	**Mass (g)**	**Crystal Mass (g)**
1	0.0041	0.0022
2	0.0045	0.0026
3	0.0042	0.0023
4	0.0043	0.0024
5	0.0043	0.0024
6	0.0044	0.0025
7	0.0045	0.0026
8	0.0045	0.0026

Table 59: Mass of dots with AF powder adhered.

AF Dots

Dot number	Weight (g)	Crystal Mass (g)
1	0.0061	0.0042
2	0.0052	0.0033
3	0.0051	0.0032
4	0.0037	0.0018
5	0.0049	0.0030
6	0.0047	0.0028
7	0.0051	0.0032
8	0.0048	0.0029

Table 60: Mass of dots with HA powder adhered.

Hot Acid Dots

Dot number	Weight (g)	Crystal Mass (g)
1	0.0026	0.0007
2	0.0024	0.0005
3	0.0027	0.0008
4	0.0026	0.0007
5	0.0025	0.0006
6	0.0025	0.0006
7	0.0025	0.0006
8	0.0027	0.0008

Table 61: Measurement data of unmodified Al_2O_3 dots pre-irradiation.

Unmodified Al_2O_3 Dots Pre-irradiation

Measurement	Dot 1 (counts)	Counts/g	Dot 2 (counts)	Counts/g	Dot 3 (counts)	Counts/g	Dot 4 (counts)	Counts/g
1	9	4029.85	8	3037.97	8	3428.57	8	3287.67
2	7	3134.33	9	3417.72	9	3857.14	7	2876.71
3	9	4029.85	10	3797.47	11	4714.29	9	3698.63
4	9	4029.85	10	3797.47	12	5142.86	7	2876.71
5	8	3582.09	8	3037.97	10	4285.71	10	4109.59
6	10	4477.61	9	3417.72	7	3000	8	3287.67
7	8	3582.09	10	3797.47	9	3857.14	12	4931.51
8	9	4029.85	8	3037.97	10	4285.71	11	4520.55
9	8	3582.09	8	3037.97	8	3428.57	7	2876.71
10	9	4029.85	10	3797.47	9	3857.14	9	3698.63
Average (counts)	8.6	3850.75	9	3417.72	9.3	3985.71	8.8	3616.44

Table 62: Measurement data of unmodified Al_2O_3 dots exposed to 5 minutes of a filtered beam for a calculated dose of 19.4 Gy.

Unmodified Al_2O_3 Dots 5 min, filtered beam, 19.4 Gy

Measurement	Dot 1 (counts)	Counts/g	Dot 2 (counts)	Counts/g	Dot 3 (counts)	Counts/g	Dot 4 (counts)	Counts/g
1	11	4925.37	12	4556.96	11	4714.29	10	4109.59
2	9	4029.85	9	3417.72	10	4285.71	8	3287.67
3	7	3134.33	10	3797.47	12	5142.86	10	4109.59
4	8	3582.09	10	3797.47	9	3857.14	10	4109.59
5	9	4029.85	9	3417.72	8	3428.57	9	3698.63
6	7	3134.33	9	3417.72	9	3857.14	9	3698.63
7	8	3582.09	9	3417.72	9	3857.14	8	3287.67
8	7	3134.33	12	4556.96	8	3428.57	11	4520.55
9	9	4029.85	11	4177.22	11	4714.29	11	4520.55
10	8	3582.09	10	3797.47	11	4714.29	8	3287.67
Average (counts)	8.3	3716.42	10.1	3835.44	9.8	4200	9.4	3863.01
Average Net (counts)	-0.3	-134.33	1.1	417.722	0.5	214.286	0.6	246.576
Average Error		19.28		19.58		20.49		19.65

Table 63: Measurement data of AF dots pre-irradiation.

AF Dots Pre-irradiation

Measurement	Dot 1 (counts)	Counts/g	Dot 2 (counts)	Counts/g	Dot 3 (counts)	Counts/g	Dot 4 (counts)	Counts/g
1	6	1417.32	9	2700	9	2783.51	11	6000
2	9	2125.98	7	2100	7	2164.95	9	4909.09
3	7	1653.54	9	2700	8	2474.23	10	5454.55
4	9	2125.98	9	2700	8	2474.23	12	6545.46
5	8	1889.76	7	2100	9	2783.51	10	5454.55
6	9	2125.98	8	2400	8	2474.23	10	5454.55
7	10	2362.2	7	2100	9	2783.51	11	6000
8	8	1889.76	7	2100	8	2474.23	14	7636.37
9	8	1889.76	8	2400	9	2783.51	10	5454.55
10	8	1889.76	8	2400	10	3092.78	12	6545.46
Average (counts)	8.2	1937.01	7.9	2370	8.5	2628.87	10.9	5945.46

Table 64: Measurement data of AF dots exposed to 5 minutes of a filtered beam for a calculated dose of 19.4 Gy.

AF Dots 5 min, filtered beam, 19.4 Gy

Measurement	Dot 1	Counts/g	Dot 2	Counts/g	Dot 3	Counts/g	Dot 4	Counts/g
1	23	5433.07	22	6600	25	7731.96	23	12545.5
2	25	5905.51	30	9000	21	6494.85	23	12545.5
3	23	5433.07	30	9000	24	7422.68	24	13090.9
4	25	5905.51	30	9000	22	6804.12	24	13090.9
5	23	5433.07	28	8400	21	6494.85	23	12545.5
6	29	6850.39	28	8400	21	6494.85	21	11454.5
7	24	5669.29	28	8400	22	6804.12	21	11454.5
8	26	6141.73	26	7800	22	6804.12	22	12000
9	24	5669.29	30	9000	24	7422.68	21	11454.5
10	23	5433.07	26	7800	18	5567.01	25	13636.4
Average (counts)	24.5	5787.4	27.8	8340	22	6804.12	22.7	12381.8
Average Net (counts	16.3	3850.39	19.9	5970	13.5	4175.26	11.8	6436.36
Average Error		24.06		28.88		26.08		35.19

Table 65: Measurement data of HA dots pre-irradiation.

Hot Acid Dot Pre-irradiation

Measurement	Dot 1 (counts)	Counts/g	Dot 2 (counts)	Counts/g	Dot 3 (counts)	Counts/g	Dot 4 (counts)	Counts/g
1	9	12272.7	8	15000	10	12000	9	12272.7
2	10	13636.4	11	20625	10	12000	12	16363.6
3	8	10909.1	9	16875	10	12000	10	13636.4
4	9	12272.7	8	15000	9	10800	10	13636.4
5	9	12272.7	9	16875	10	12000	9	12272.7
6	10	13636.4	8	15000	9	10800	10	13636.4
7	8	10909.1	9	16875	12	14400	8	10909.1
8	10	13636.4	10	18750	10	12000	9	12272.7
9	10	13636.4	10	18750	10	12000	7	9545.46
10	9	12272.7	11	20625	8	9600	8	10909.1
Average (counts)	9.2	12545.5	9.3	17437.5	9.8	11760	9.2	12545.5

Table 66: Measurement data of AF dots exposed to 5 minutes of a filtered beam for a calculated dose of 19.4 Gy.

HA Dots 5 min, filtered beam, 19.4 Gy

Measurement	Dot 1 (counts)	Counts/g	Dot 2 (counts)	Counts/g	Dot 3 (counts)	Counts/g	Dot 4 (counts)	Counts/g
1	13	17727.3	12	22500	11	13200	10	13636.4
2	10	13636.4	11	20625	13	15600	8	10909.1
3	10	13636.4	8	15000	11	13200	10	13636.4
4	9	12272.7	10	18750	12	14400	11	15000
5	10	13636.4	8	15000	12	14400	9	12272.7
6	9	12272.7	7	13125	10	12000	10	13636.4
7	11	15000	9	16875	10	12000	10	13636.4
8	10	13636.4	9	16875	11	13200	10	13636.4
9	11	15000	7	13125	11	13200	10	13636.4
10	8	10909.1	10	18750	11	13200	10	13636.4
Average (counts)	10.1	13772.7	9.1	17062.5	11.2	13440	9.8	13363.6
Average Net (counts)	0.9	1227.27	-0.2	-375	1.4	1680	0.6	818.18
Average Error (counts)		37.11		41.31		36.66		36.56

Table 67: Measurement data of unmodified Al_2O_3 dots pre-irradiation.

Unmodified Al_2O_3 pots Pre-irradiation

Measurement	Dot 5 (counts)	Counts/g	Dot 6 (counts)	Counts/g	Dot 7 (counts)	Counts/g	Dot 8 (counts)	Counts/g
1	7	2876.71	8	3157.9	7	2658.23	10	3797.47
2	8	3287.67	6	2368.42	8	3037.98	7	2658.23
3	9	3698.63	7	2763.16	8	3037.98	7	2658.23
4	8	3287.67	8	3157.9	8	3037.98	10	3797.47
5	7	2876.71	10	3947.37	8	3037.98	10	3797.47
6	7	2876.71	7	2763.16	8	3037.98	8	3037.98
7	7	2876.71	8	3157.9	10	3797.47	9	3417.72
8	11	4520.55	10	3947.37	7	2658.23	8	3037.98
9	9	3698.63	10	3947.37	9	3417.72	9	3417.72
10	7	2876.71	10	3947.37	8	3037.98	8	3037.98
Average (counts)	8	3287.67	8.4	3315.79	8.1	3075.95	8.6	3265.82

Table 68: Measurement Data for unmodified Al_2O_3 dots exposed to an unfiltered beam for 5 minutes.

Unmodified Al_2O_3 Dots Exposed to an Unfiltered Beam for 5 minutes

Measurement	Dot 5 (counts)	Counts/g	Dot 6 (counts)	Counts/g	Dot 7 (counts)	Counts/g	Dot 8 (counts)	Counts/g
1	30	12328.8	29	11447.4	36	13670.9	29	11012.7
2	24	9863.02	24	9473.69	40	15189.9	24	9113.93
3	25	10274	28	11052.6	30	11392.4	24	9113.93
4	21	8630.14	23	9078.95	34	12911.4	26	9873.42
5	18	7397.26	21	8289.47	33	12531.6	20	7594.94
6	24	9863.02	22	8684.21	28	10632.9	23	8734.18
7	20	8219.18	21	8289.47	31	11772.2	23	8734.18
8	19	7808.22	19	7500	26	9873.42	21	7974.68
9	19	7808.22	20	7894.74	29	11012.7	20	7594.94
10	18	7397.26	17	6710.53	26	9873.42	16	6075.95
Average (counts)	21.8	8958.91	22.4	8842.11	31.3	11886.1	22.6	8582.28
Average Net (counts)	13.8	5671.23	14	5526.32	23.2	8810.13	14	5316.46
Average Error		29.93		29.74		34.48		29.30

Table 69: Measurement data for AF dots pre-irradiation.

AF Dots Pre-Irradiation

Measurement	Dot 5 (counts)	Counts/g	Dot 6 (counts)	Counts/g	Dot 7 (counts)	Counts/g	Dot 8 (counts)	Counts/g
1	9	2967.03	12	4235.29	10	3092.78	10	3409.09
2	8	2637.36	11	3882.35	8	2474.23	8	2727.27
3	9	2967.03	10	3529.41	8	2474.23	8	2727.27
4	8	2637.36	11	3882.35	8	2474.23	10	3409.09
5	8	2637.36	11	3882.35	7	2164.95	8	2727.27
6	7	2307.69	11	3882.35	8	2474.23	11	3750
7	7	2307.69	10	3529.41	8	2474.23	9	3068.18
8	9	2967.03	11	3882.35	7	2164.95	10	3409.09
9	7	2307.69	11	3882.35	9	2783.51	7	2386.36
10	10	3296.7	12	4235.29	8	2474.23	9	3068.18
Average (counts)	8.2	2703.3	11	3882.35	8.1	2505.15	9	3068.18

Table 70: Measurement data for AF dots exposed to an unfiltered beam for 5 minutes.

AF Dots Exposed to an Unfiltered Beam for 5 minutes

Measurement	Dot 5 (counts)	Counts/g	Dot 6 (counts)	Counts/g	Dot 7 (counts)	Counts/g	Dot 8 (counts)	Counts/g
1	958	315824	780	275294	1061	328144	1117	380795
2	951	313517	735	259412	1016	314227	1098	374318
3	903	297692	746	263294	1034	319794	1064	362727
4	891	293736	736	259765	1013	313299	1055	359659
5	872	287473	710	250588	973	300928	1044	355909
6	876	288791	717	253059	982	303711	1021	348068
7	867	285824	711	250941	974	301237	994	338864
8	840	276923	688	242824	930	287629	1010	344318
9	849	279890	673	237529	928	287010	967	329659
10	838	276264	681	240353	933	288557	972	331364
Average (counts)	884.5	291593	717.7	253306	984.4	304454	1034.2	352568
Average Net (counts)	876.3	288890	706.7	249424	976.3	301948	1025.2	349500
Average Error		170.76		159.16		174.49		187.77

Table 71: Measurement data for HA dots pre-irradiation.

HA Dots Pre-Irradiation

Measurement	Dot 5 (counts)	Counts/g	Dot 6 (counts)	Counts/g	Dot 7 (counts)	Counts/g	Dot 8 (counts)	Counts/g
1	7	11052.6	8	12631.6	10	15789.5	7	8400
2	8	12631.6	8	12631.6	7	11052.6	8	9600
3	8	12631.6	7	11052.6	9	14210.5	9	10800
4	8	12631.6	9	14210.5	9	14210.5	8	9600
5	7	11052.6	9	14210.5	8	12631.6	10	12000
6	10	15789.5	7	11052.6	8	12631.6	12	14400
7	8	12631.6	8	12631.6	8	12631.6	10	12000
8	7	11052.6	7	11052.6	9	14210.5	10	12000
9	7	11052.6	7	11052.6	8	12631.6	12	14400
10	8	12631.6	9	14210.5	10	15789.5	11	13200
Average (counts)	7.8	12315.8	7.9	12473.7	8.6	13579	9.7	11640

Table 72: Measurement data for HA dots exposed to an unfiltered beam for 5 minutes.

HA Dots Exposed to an Unfiltered Beam for 5 minutes

Measurement	Dot 5 (counts)	Counts/g	Dot 6 (counts)	Counts/g	Dot 7 (counts)	Counts/g	Dot 8 (counts)	Counts/g
1	14	22105.3	17	26842.1	15	23684.2	15	18000
2	12	18947.4	17	26842.1	12	18947.4	15	18000
3	13	20526.3	12	18947.4	15	23684.2	15	18000
4	15	23684.2	13	20526.3	14	22105.3	14	16800
5	13	20526.3	15	23684.2	14	22105.3	14	16800
6	13	20526.3	13	20526.3	14	22105.3	12	14400
7	11	17368.4	13	20526.3	15	23684.2	14	16800
8	14	22105.3	10	15789.5	12	18947.4	12	14400
9	11	17368.4	13	20526.3	11	17368.4	13	15600
10	13	20526.3	8	12631.6	12	18947.4	11	13200
Average (counts)	12.9	20368.4	13.1	20684.2	13.4	21157.9	13.5	16200
Average Net (counts)	5.1	8052.64	5.2	8210.53	4.8	7578.95	3.8	4560
Average Error		45.13		45.48		46.00		40.25